Spring 1-1-2014

Optically Active Plasmonic Microbubbles

Jacob Dove
University of Colorado Boulder, jacob.dove@colorado.edu

Optically Active Plasmonic Microbubbles

by

JACOB DOVE

B.S., Iowa State University, 2007

M.S., University of Colorado, 2012

A thesis submitted to the

Faculty of the Graduate School of the

University of Colorado in partial fulfillment

Of the requirement for the degree of

Doctor of Philosophy

Department of Mechanical Engineering

2014

This thesis entitled:
Optically Active Plasmonic Microbubbles
written by Jacob Dove
has been approved for the Department of Mechanical Engineering

_____

Professor Todd Murray
Mechanical Engineering, University of Colorado Boulder

_____

Professor Mark Borden
Mechanical Engineering, University of Colorado Boulder

Date: November 20, 2014

The final copy of this thesis has been examined by the signatories, and we find that both the content and the form meet acceptable presentation standards of scholarly work in the above mentioned discipline.

Abstract

Dove, Jacob (Ph.D., Mechanical Engineering)

Optically Active Plasmonic Microbubbles

Thesis directed by Associate Professors Mark Borden and Todd Murray

Contrast agents are used across a variety of medical imaging modalities for improved visualization of structures in the body. Microbubbles, for example, efficiently scatter ultrasound thereby providing enhanced ultrasonic imaging of the vasculature. Plasmonic nanoparticles, on the other hand, are efficient optical absorbers and can provide improvements in optical and photoacoustic imaging.

The focus of this thesis is on the development of novel contrast agents capable of enhancing both ultrasound and photoacoustic imaging modalities. The first agent is constructed by templating nanoparticles onto a lipid-encapsulated microbubble with a perfluorocarbon gas core. Using an avidin-biotin conjugation scheme, control over the nanoparticle surface density is achieved. The nanoparticle shell absorbs pulsed laser radiation and heats the microbubble gas core, producing a strong photoacoustic response. Upon destruction of the microbubble gas core the photoacoustic response is diminished. A model of laser driven bubble oscillations is presented and the amplitude and frequency correlate well with experiment. Contrast enhanced dual mode imaging is demonstrated in a tissue phantom and contrast is quantified. In addition, the properties of individual nanoparticle-coated microbubbles, such as the shell elasticity and viscosity, are found by exciting them with a pulsed laser source in an optical microscope and detecting the resulting oscillations using light scattering. The all optical interface is an attractive platform for the study of microbubble physics.

The second contrast agent is a nanoparticle-templated, sub-micron droplet with a liquid perfluorocarbon core. Advantages of this agent are increased circulation time and the ability to leave leaky tumor vasculature due to the sub-micron size. Nanoparticle-templated droplets are fabricated using a condensation technique, where application of high pressure to the nanoparticle-templated microbubbles causes the gas core to condense into a metastable, superheated liquid. Pulsed laser heating of the liquid core transforms the droplet back into a microbubble. The droplet undergoes explosive vaporization producing an exceptionally strong photoacoustic response. The resulting microbubble is templated with nanoparticles and capable of providing photoacoustic and ultrasound contrast. The core material of the droplet is found to have a strong effect on the threshold fluence for vaporization, with lower boiling temperature droplets vaporizing at a lower fluence.

Acknowledgements

I would like to thank everyone that helped make this project a success. First I would like to thank both of my advisors Drs. Mark Borden and Todd Murray for their support through the progress of this work. They provided me the freedom to explore interesting avenues associated with this work while also providing direction when needed.

I would like to thank members of the Borden and Murray lab groups. Thanks to Dr. Shashank Sirsi and Dr. Jameel Feshitan for their patience and willingness to teach me about contrast agent fabrication. Their knowledge in the chemical design of microbubble proved extremely useful. Much thanks to Dr. Hengyi Ju for the many discussions on photoacoustics and ultrasound. His technical expertise in both theory and experiment was extremely valuable. I would also like to thank Paul Mountford for help with droplet fabrication and the many discussions that added to the depth of the work.

I would like to thank my family. Thanks to my parents as they constantly provided me with encouraging words and support throughout my entire life. Special thanks are due to my wife. Her unflinching faith in my abilities was truly inspiring and she has been a constant source of inspiration and encouragement.

Contents

Figures

Chapter 1

Introduction

1.1. Microbubbles in Medicine

The ability to ultrasonically image the vasculature has motivated research in microbubbles since 1968 when it was reported that an agitated saline solution containing "mini bubbles" greatly enhanced ultrasound contrast [1]. Today, microbubbles are FDA approved for contrast enhanced echocardiography. Microbubbles are 1-10 μm in diameter and consist of air or inert gas surrounded by a thin polymer or phospholipid shell. The shell serves to help stabilize the microbubbles against dissolution in the blood by reducing the surface tension and providing a barrier for gas diffusion and coalescence [2,3]. Upon exposure to an ultrasound field, microbubbles can undergo strong oscillations, producing a scattered field with both linear and nonlinear components [4].

Current imaging approaches take advantage of the nonlinear scattered fields to improve microbubble contrast with respect to the more linear background scattering in tissue [5]. The nonlinear microbubble response depends highly on the ultrasound frequency, pressure amplitude

and phase. This has steered research to design ultrasound pulse trains that modulate the phase and pressure to optimize the microbubble contrast-to-tissue ratio [6]. For example, pulse inversion imaging can be used to reconstruct excellent images of the vasculature, as shown in Fig. 1.1 [7]. Here, the detected backscatter from two pulses with opposite phases are summed together. In the linear regime the summation cancels out resulting in no contrast. However, the nonlinear microbubble response results in a nonzero summation. Hence, pulse inversion imaging can improve sensitivity and specificity of microbubble contrast. Amplitude modulation is a similar technique that modulates the pressure of the transmit pulse [8]. Transmit pulses consisting of either phase or amplitude modulation were compared and found to achieve identical levels of enhancement. However, transmit pulses containing a combination of amplitude and phase modulation enhanced the nonlinear microbubble response and contrast was found to improve by 28% compared to using only amplitude or phase modulation [9].

Detection of a sub-harmonic or higher harmonic echoes from nonlinear resonant microbubble oscillations is another avenue that can lead to improved microbubble contrast. In a study by Kruse and Ferrara, microbubbles were imaged in a flow-through phantom by detecting the higher harmonic emission [10]. The microbubbles were also imaged through the linear backscatter at the higher frequency for comparison. Higher harmonic imaging was shown to improve contrast over 10 dB. However, sub-harmonic detection of microbubbles offers benefits as opposed to the detection of higher harmonics, and has received interest as a microbubble specific imaging modality [11,12]. The lower frequencies from sub-harmonic emission are advantageous for deep tissue imaging applications where ultrasound is less scattered and attenuated. Interestingly, coated microbubbles have been shown to emit sub-harmonics at lower driving pressures than uncoated bubbles [13,14]. Theoretically, nonlinearities in the microbubble shell stiffness can lower the

required pressure for sub-harmonic emission [15]. Recently, sub-harmonic microbubble detection was demonstrated *in vivo* with a 20 dB improvement over the endogenous background signal [16].

Figure 1.1 Microbubble contrast enhanced image of liver vasculature, with the white arrow corresponding to slowly perfusing tissue. A nonlinear contrast imaging technique, pulse inversion, was used to improve microbubble contrast along with a temporal averaging technique (from Wilson *et. al.*) [7].

1.2. Microbubble Imaging Applications

Blood is a poor acoustic scatterer and therefore ultrasound imaging of the vasculature is difficult. Nevertheless, vascular density and blood flow are important parameters for the diagnosis of cancer and cardiovascular disease [17,18]. In addition, the vascular geometry was found to contain important information regarding the delivery of nanoparticles or drugs to cells outside the vasculature [19]. Hence, it is advantageous to construct images of the vasculature that allow for the geometry, density, and blood flow to be quantified. Ultrasound imaging of vasculature can be achieved by intravenous injection of microbubbles to improve contrast. Here, a bolus of concentrated microbubbles (~1 mL at 10^9 ml^{-1}) is injected intravenously. Microbubbles 1-10 μm in diameter can circulate throughout the vasculature because they are capable of freely passing through the capillary system [20]. Nonlinear imaging techniques can be used to create contrast

enhanced images that map out the vasculature geometry [17]. In addition, blood volume and flow can be measured with microbubble enhanced imaging of the vasculature. The contrast enhancement before and after the addition of microbubbles provides an estimate of the vascular density (i.e. blood volume) [18]. After the microbubbles have fully populated the vasculature, a destruction pulse of high intensity ultrasound is directed towards the microbubbles. As the microbubbles are destroyed the enhanced contrast is lost. Capturing the intensity-time curve as the microbubbles repopulate the vasculature gives a measure of blood flow [21]. For example, the dark region in Fig. 1.1 is a result of slowly perfusing tissue. This demonstrates the powerful diagnostic capabilities of the microbubbles.

Microbubbles can also be used to provide therapeutic benefits [22]. During imaging applications, the microbubble undergoes stable cavitation and oscillates around an equilibrium radius. At higher ultrasound intensities a microbubble can undergo violent oscillations that lead to inertial collapse. As the bubble collapses, significant mechanical forces and strains are produced on the nearby endothelium. These forces and strains can increase the gaps between the endothelium cells, increasing vascular permeability and, therefore, drug delivery to the interstitium. For example, a study by Chen *et. al.* imaged microbubble inertial collapse with a high speed camera *in vivo* and observed the invagination of the vessel after inertial collapse [23]. Recently, focused ultrasound was used with microbubbles to transiently open the blood-brain-barrier (BBB) [24,25]. Gadolinium was co-administered with the microbubbles and the extravasation through the BBB was imaged with magnetic resonance imaging (MRI). Significant forces can also be produced during large-amplitude, nonlinear microbubble oscillations. Tung *et. al.* showed that for small microbubbles (1-2 μm in diameter) inertial collapse was required to open the BBB. However, for large bubbles (6-8 μm in diameter) lower ultrasonic pressures, where the microbubble exhibited

nonlinear oscillations, was sufficient to open the BBB [26]. It was suggested that inertial cavitation was not needed because the larger microbubble was in contact with the vessel wall.

1.3. Functionalized Microbubbles

Microbubbles can be functionalized for molecular imaging [27,28]. Molecular imaging offers several benefits ranging from early diagnosis to monitoring disease progression. Here, a disease specific molecule is targeted and imaged *in vivo*. One approach to target microbubbles to diseased tissue is through nonspecific binding of the microbubble shell [29]. However, this method lacks specificity and is limited to certain applications. Attaching disease targeting ligands to the microbubble shell allows for microbubble accumulation at the diseased tissue through binding with the receptor. The targeting ligands commonly consist of antibodies or peptides and are disease specific [30]. Ideally, molecular imaging would only be sensitive to the microbubbles that attached to the disease [31]. However, in practice freely circulating microbubbles remain after injection and relatively long dwell times are required to clear non-adherent microbubbles from the vasculature [32]. It would be beneficial to immediately distinguish adherent microbubbles from freely circulating. Recently, an approach was developed to image the nonspecific binding of microbubbles [33]. Here, the individual pixels from contrast enhanced image were separated into two compartments. If the pixels remained at a constant intensity over time, they were grouped into a time-independent compartment. Conversely, pixels with an intensity that fluctuated with respect to time were grouped into a time-fluctuating compartment. The adherent microbubbles were assumed to enhance the time-independent image while the freely circulating microbubbles contributed to the time-fluctuating enhancement. A similar approach was recently used to image targeted microbubbles in a flow-through phantom [34].

Microbubbles can also be used to actively target a region for molecular imaging with ultrasound radiation pressure [35]. Relying on microbubbles that passively flow in the vasculature and attach to the vessel wall is inefficient because the majority of the microbubbles will flow at the center of the vessel. Ultrasound radiation pressure has been used to push the microbubbles against the vessel wall and increase the number of targeted microbubbles that bind to receptors [36]. This approach is particularly appealing because the targeting ligands can be buried into the shell. While targeting ligands are designed to bind with a specific bio-marker, they can still display nonspecific binding or trigger an immune response (through binding with proteins in the complement immune system) both of which are unwanted. Ultrasound radiation pressure can push the microbubble against the vessel wall and expose the buried ligand to the receptor [37,38]. Microbubbles with a buried ligand architecture improve circulation persistence by shielding the targeting ligand from the immune system and exposing them only at the actively targeted site [38].

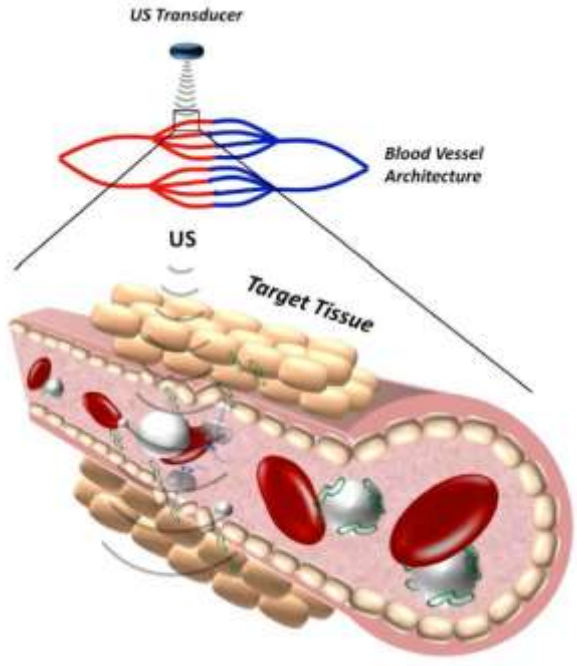

Figure 1.2 A cartoon depicting targeted drug delivery utilizing microbubbles as the delivery vehicle, the abbreviation US stands for ultrasound (from Sirsi *et. al.*) [39].

As shown in Fig. 1.2, microbubbles may be functionalized to incorporate drugs or genes within or on the shell and act as delivery vehicles for the local release of the loaded therapeutic [39–41]. By minimizing the impact of the drug on healthy tissue and maximizing the drug exposure to the diseased tissue, the therapeutic index (defined as the lethal dose in 50% of the population to the effective dose in 50% of the population) can be improved. The therapeutic is locally delivered by targeting a specific area with high intensity ultrasound. High-intensity ultrasound has been observed via high-speed camera to cause microbubble fragmentation [42,43]. Drug-loaded microbubbles can be imaged with low intensity ultrasound as they travel to the desired location and the drug can be locally released with high intensity ultrasound. Microbubble fragmentation is an appealing mechanism for drug delivery. The fragmentation threshold for microbubbles has been found to depend on the ultrasound pulse parameters and shell composition [44]. Specifically, lipid shelled microbubbles have been found to fragment at lower ultrasound pressures than polymer shelled microbubbles [45]. In addition, recent studies have found that a small amount of shell material sheds from the microbubble at ultrasound pressures below the fragmentation threshold [46–48]. These results indicate that it could be possible to control the drug release from the microbubble shell by adjusting the frequency or pressure amplitude of the ultrasound.

1.4. Physiochemical Properties of Microbubbles

Microbubbles have been engineered to increase stability while maintaining the echogenicity provided by the compressible gas core [49]. The role of the encapsulating shell is to stabilize the gas core which would otherwise quickly dissolve. This is due to the Laplace pressure, which increases as the radius decreases, and will exceed 2 atm for an air bubble with a 1 μm diameter. To stabilize the microbubble against dissolution, an encapsulating shell and high molecular weight gases are used [2,3]. The shell serves to lower the Laplace pressure. High molecular weight gasses

can slow microbubble dissolution due to lower solubility. When gases with low diffusivities are used, the microbubble can undergo size changes when placed in an aqueous environment. Here, concentration gradients of the gases cause an initial influx of oxygen and nitrogen. The gas core efflux is slower than the influx and results in an increase in the microbubble radius. As time progresses the gas core exchanges its contents and relaxes back to the initial radius and eventually undergoes dissolution [51].

Common shell materials used to stabilize micron size bubbles include proteins, polymers and lipids. In a review by Stride *et. al.* different shell materials and fabrication techniques are discussed [52]. Proteins and polymers have a tendency to create rigid shells that can significantly alter the responsiveness of the gas core to an ultrasonic field. Depending on the application, a polymer or lipid shell could be advantageous. For imaging applications, a lipid shell would offer the benefit of increased echogencity. However, for drug delivery applications when stability is highly desirable, a polymer shell offers benefits.

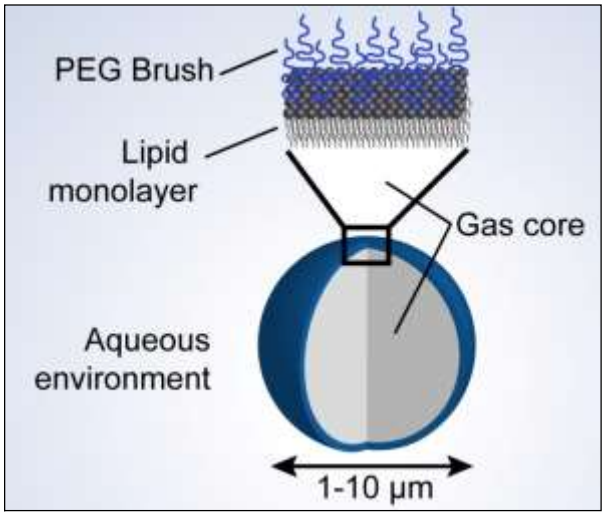

Figure 1.3 Cartoon of a lipid-encapsulated microbubble in an aqueous environment, highlighting the important features of the microbubble.

Figure 1.3 depicts the construction of a lipid-encapsulated microbubble. Lipids are a class of amphiphilic molecules (i.e. part hydrophobic and part hydrophilic) and self-assemble into a monolayer at the gas-liquid interface, with the hydrophobic portion of the lipid orientated towards the gas core. To improve microbubble stability *in vivo*, poly(ethylene glycol) (PEG) is added to the shell of the microbubble in the form of a brush layer. To achieve a brush layer, the PEG spacing must be less than the radius of gyration of the polymer. The brush layer acts as an invisibility cloak to the immune system and increases circulation persistence. In addition, the PEG brush provides steric repulsion which resists coalescence with other microbubbles and improves stability.

Until recently, the specific role of the shell molecules on the microbubble properties had not been examined. Dicker *et. al.* studied the dependence of the PEG molecular weight on the shell stiffness [53]. When the PEG did not form a brush layer, the PEG molecular weight did not affect the microbubble properties. However, when the PEG formed a brush layer, the microbubble shell stiffness decreased with increasing PEG molecular weight. This was attributed to the increase in PEG lateral repulsion as molecular weight increased. Recently, Garg *et. al.* investigated the dependence of the lipid-lipid intermolecular forces on microbubble stability [54]. Longer acyl chain lipids were shown to improve *in vitro* and *in vivo* circulation persistence. This improvement was related to increased van der Waals attraction in the longer acyl chained lipids. The added cohesion from the additional acyl chain length provided increased resistance to gas dissolution which resulted in increased in circulation persistence.

1.5. Physics of Microbubble Oscillations

Microbubbles offer excellent ultrasound contrast due to their ability to oscillate in response to the ultrasound field [55]. The problem of cavitation physics has a long history and was first considered by Lord Rayleigh in 1917 [56]. Later, in 1947, Plesset expanded on the problem of cavitation

resulting in an equation describing the bubble wall motion in response to an arbitrary pressure wave and commonly referred to as the Rayleigh-Plesset equation [57]. The Rayleigh-Plesset equation relates the time-dependent radius of an oscillating spherical bubble to the pressure difference between the bubble gas core and the surrounding liquid. Thus, the behavior of the gas (isothermal, isobaric, adiabatic or polytropic) needs to be included in the Rayleigh-Plesset equation to fully describe the dynamics of bubble wall radius. Below, the Rayleigh-Plesset equation is combined with the polytropic gas law.

$$\rho\left(\frac{3\dot{R}^2}{2}+R\ddot{R}\right)=\left(p_0+\frac{2\sigma}{R_0}\right)\left(\frac{R_0}{R}\right)^{3\gamma}-\frac{2\sigma}{R}-\frac{4\eta\dot{R}}{R}-p_0-P(t) \tag{1.1}$$

Here, R is the time-dependent radius of curvature of the bubble, p_o is the ambient pressure outside the bubble, R_0 is the radius of curvature at equilibrium, η viscosity of the liquid, γ is the polytropic exponent and $P(t)$ is the driving pressure. An applied ultrasound field, $P(t)$, forces a bubble to oscillate which sets the liquid into motion (described by the left-hand side). As the bubble oscillates, the gas core expands and compresses which is described through a polytropic process that relates the gas pressure of the bubble at equilibrium ($p_{g,e}=p_0+2\sigma/R_0$) to an instantaneous gas pressure in the bubble ($p_g=p_{g,e}\left(R_0/R\right)^{3\gamma}$). For micron sized bubbles, the main contribution to damping is viscous losses in the liquid. However, more damping sources exist such as the radiation of sound and thermal dissipation [58,59]. The above expression may be considered a starting point for all bubble dynamics [60–64].

1.5.1. The Encapsulated Microbubble

The encapsulating shell of a microbubble is expected to alter the dynamics compared to that of a free bubble. Specifically, the shell adds both an extra restoring force (shell elasticity) and damping

(shell viscosity). Several models have been presented in the literature to describe the effect of an encapsulating shell. Marmottant *et. al.* modified the Rayleigh-Plesset equation (Eqn. (1.2)) to account for the lipid shell [65].

$$\rho\left(\frac{3\dot{R}^2}{2}+R\ddot{R}\right)=\left(p_0+\frac{2\sigma(R_0)}{R_0}\right)\left(\frac{R_0}{R}\right)^{3\gamma}-\frac{2\sigma(R)}{R}-\frac{4\kappa_s\dot{R}}{R^2}-\frac{4\eta\dot{R}}{R}-p_0-P(t) \qquad (1.2)$$

Where $\sigma(R)$ is the size dependent surface tension of the lipid shell and κ_s is the shell viscosity. The shell properties, $\sigma(R)$ and κ_s, are incorporated into the Rayleigh-Plesset equation by performing a stress balance at the bubble interface. The size dependent surface tension, $\sigma(R)$, accounts for three different compression and expansion regimes, as shown in Fig. 1.4.

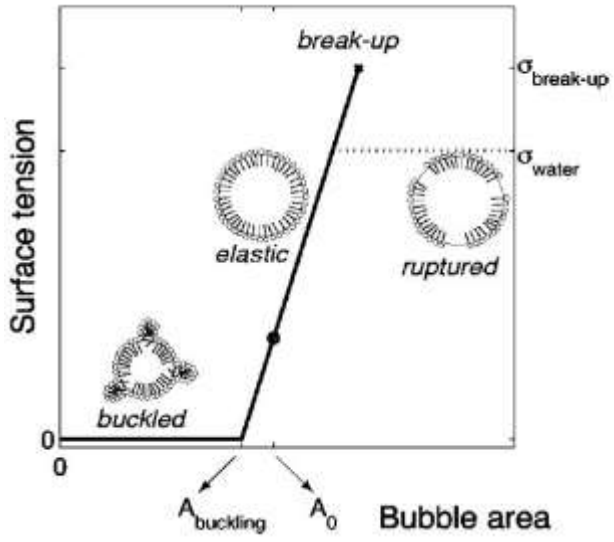

Figure 1.4 The size dependent surface tension of a lipid shelled microbubble showing the buckled, elastic and ruptured regimes (from Marmottant *et. al.*) [65].

For oscillations below a critical buckling radius, the bubble is said to be in the buckled regime. Here, the shell can contract until wrinkling or folds occur, which causes the surface tension to approach zero. This regime is shown in Fig. 1.4 where the bubble area is below $A_{buckling}$. The zero

surface tension term is because the monolayer is fully compressed. Here no work goes into increasing the intermolecular distance of the lipid molecules, just increasing or decreasing the folds in the shell, similar to an accordion.

For oscillations greater than a critical ruptured radius, the bubble is said to be in the ruptured regime. Here, the bubble expansion causes the lipid shell to rupture and exposes gas-liquid interface. The size dependent surface tension term then takes the value of the surface tension of the gas-liquid interface. This is depicted in Fig. 1.4 for a bubble area greater than the break-up point.

A linear elastic regime is defined when the bubble oscillates between the critical buckling radius, and the surface tension is described as:

$$\sigma(R) = \chi\left(\frac{R^2}{R_{buckle}^2} - 1\right) \tag{1.3}$$

Here, R_{buckle} is the buckled radius and χ is the shell elasticity, defined as $\chi = A(d\sigma/dA)$ where A is the surface area of the lipid shell. This is shown in Fig. 1.4 as the linear regime between the buckling and break-up areas. The shell elasticity (χ) can be determined from the slope of the line from $A_{buckling}$ to the break-up point.

The lipid shell is a complex visco-elastic material exhibiting behavior such as wrinkling, buckling, or rupture. The Marmottant model is one of many modified Rayliegh-Plesset equations to describe the dynamics of a lipid-encapsulated microbubble. A recent review by Doinikov and Bouakaz covers the details of the different models [66].

To understand the complex dynamics of shelled microbubbles when exposed to ultrasound, experiments have been performed on individual microbubbles. Here, optical or acoustic methods

have been used to interface with a single microbubble. Acoustic detection relates the scattered pressure from the microbubble to a radius-time curve [67–70]. Here, an acoustic transducer is used to collect the scattered ultrasound from the bubble oscillations. The radius-time curve is then determined by converting the scattered ultrasound to a radius through a model for the scattered pressure from an oscillating bubble. Optical methods to measure radius-time curves use a high speed camera or optical scattering. Several groups have utilized a high speed camera with frame rates in the millions of frames per second, to capture the first few oscillations from a microbubble under a microscope [43,71,72]. Another path to optically track the bubble wall radius is to collect the scattered light from an oscillating microbubble [73–75]. The fluctuations in scattered light are then converted to radial fluctuation with a conversion curve that relates the light level at the photodetector to a bubble radius. High bandwidth and resolution can be achieved by tracking the optical scatter with a high speed photodetector and signal averaging. Cameras capable of achieving such high frame rates are expensive but allow for complex bubble motions to be observed, such as non-spherical oscillations [76,77].

Researchers have observed interesting microbubble dynamics and measured the effects from the encapsulating shell by performing experiments on single microbubbles. Van der Meer *et. al.* performed acoustic spectroscopy of single microbubbles [78]. Here, the linear response was characterized by probing a single microbubble with different driving frequencies of equal amplitudes. The response was measured with a high speed camera. The Marmottant model (Eqn. (1.2)) was used to determine shell viscosity and elasticity for lipid-encapsulated microbubbles. Recently, the nonlinear properties of the lipid-encapsulated shell were studied [70,79]. Interestingly, some of the bubbles with encapsulating shells behaved as though there was no shell (i.e. the measured shell elasticity was close zero) [79]. This behavior was attributed to the state of

the shell. Here, it was hypothesized that some microbubbles were rupturing or buckling during oscillations. During rupture the gas-liquid interface was exposed and the shelled microbubbles had resonant frequencies equal to clean bubbles.

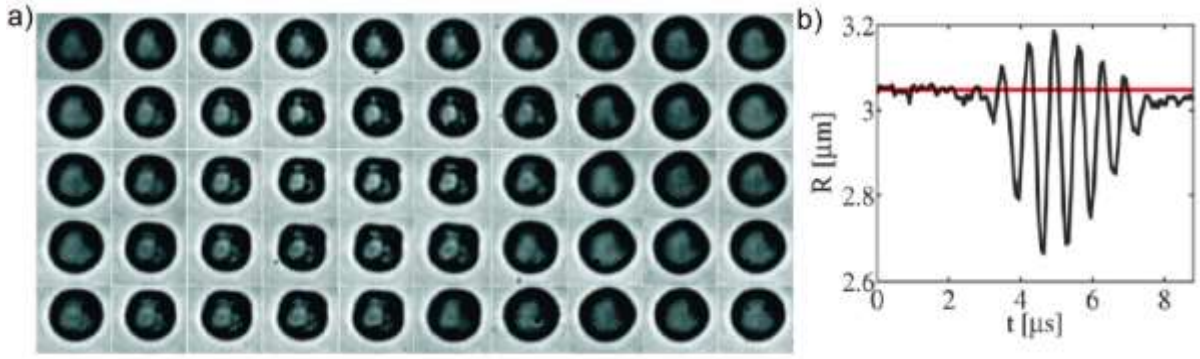

Figure 1.5 (a) High-speed optical micrographs of microbubble oscillations displaying a buckled shell during compression. (b) The corresponding radius-time curve where the "compression-only" behavior is apparent (from Sijl *et. al.*) [15].

Renaud *et. al.* observed expansion-only behavior from lipid-encapsulated microbubbles [80] and de Jong et al. observed compression-only behavior [81]. Expansion-only behavior is used to describe an oscillating bubble that exhibits a greater change in radius during the expansion phase of the oscillation than the compression phase. Compression-only behavior describes the same phenomenon but where the compression phase of the bubble oscillation exhibits a larger change in radius. These interesting nonlinear properties were attributed to a ruptured shell (expansion-only) and a buckled shell (compression-only). Using a high-speed optical camera, Sijl *et. al.* was able to capture the microbubble shell buckling during the compression phase of the bubble oscillations. This is shown in the micrograph in Fig. 1.5 where the bubble surface is initially smooth and at later times appears rough (when buckling occurs). As a buckled shell is easier to strain, the bubble displayed asymmetrical oscillations, where the bubble compressed more than it expanded, as shown in Fig. 1.5. In studies performed by Dayton *et. al.* and Morgan *et. al.* the

nonlinear dynamics of an individual microbubble were studied [42,82]. Dayton *et. al.* observed fragmentation of the microbubble during exposure to high intensity ultrasound of several hundred kPa. Morgan *et. al.* studied the effect of the driving phase on the bubble response, which is an important feature for pulse inversion imaging. The studies outlined above have been extremely valuable in understanding and translating interesting microbubble dynamics into novel imaging applications (subharmonic imaging) and therapeutic techniques (targeted drug delivery).

1.6. Microbubbles and multimodal imaging

Microbubbles can also be functionalized with agents that provide contrast in another imaging modality. Multimodal detection offers benefits in providing additional functional, molecular and/or anatomical information. In addition, improved specificity and sensitivity in detection can be achieved because each modality has different endogenous noise. For example, microbubbles loaded with gadolinium or iron oxide nanoparticles have been used to provide contrast in MRI [83,84]. Gadolinium-loaded microbubbles produced different levels of MRI contrast before and after fragmentation [83]. Detection of microbubble fragmentation may one day provide important real-time information *in vivo* during the local delivery of a therapeutic.

Various optical probes (i.e. dyes, fluorescent molecules, quantum dots and plasmonic nanoparticles) have been combined with microbubbles to create unique contrast agents. Fluorescent molecules added to the microbubble shell were found to undergo a self-quenching process during microbubble oscillations creating a modulated fluorescence signal [85]. Recently, ultrasound switchable fluorescence was shown to improve fluorescence imaging penetration depth [86]. Quantum dots have been incorporated into the microbubble shell and used to study drug delivery [87]. Here, microbubble fragmentation with high intensity ultrasound was used to deposit the quantum dots. The fluorescence distribution was analyzed to provide an optical measure of the

drug delivery. Recently, this approach was demonstrated *in vivo*, where fluorescently labeled antibodies were co-administered with microbubbles [88]. Fluorescence imaging was able to visualize the accumulation of the antibody *in vivo*. When microbubbles were exposed to high intensity ultrasound, inertial cavitation increased vascular permeability and an enhancement in the fluorescence signal was observed. The ability to monitor drug delivery is a benefit utilizing dual mode imaging.

Ultrasound combined with photoacoustics offers potentially powerful capabilities. Photoacoustic imaging is a hybrid modality that combines light with sound. Here, the tissue is illuminated with a non-ionizing optical pulse. Once the optical pulse is absorbed, the tissue undergoes rapid thermal expansion causing the emission of acoustic waves. The emitted acoustic waves travel back to the surface of the tissue where they are detected with an ultrasonic transducer. The detected ultrasound wave can be processed to create an image that maps the optical absorption distribution within tissue. Photoacoustics is unlike other optical imaging modalities that rely on ballistic photons and thus have limited penetration depth. In photoacoustics the light needs only to be absorbed allowing for imaging at depth in tissue. Recently, imaging at several centimeters into tissue has been demonstrated [90]. As blood provides endogenous contrast, one promising technique for photoacoustic imaging is mapping the vasculature, as shown in Fig 1.6. The image shown in Fig. 1.6 was reconstructed from a scanned array of 128 ultrasound transducers and acquired in 24 seconds. Remarkably, the photoacoustic image was able to resolve sub-millimeter vessels at a tissue depth of 40 mm. Several reviews have been published that cover the details of photoacoustic imaging [91–96]. Ultrasound imaging, which probes the mechanical properties of tissue, is highly compatible with photoacoustic instrumentation and provides complementary information. The same transducer may be used for both photoacoustic and ultrasound imaging

such that a co-registered image is produced. Dual mode photoacoustic and ultrasound imaging can simultaneously probe structural properties of tissue with ultrasound and functional and molecular properties of tissue with photoacoustics.

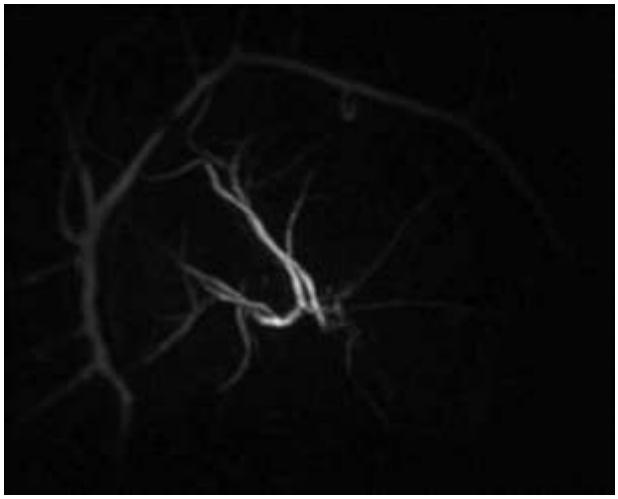

Figure 1.6 Photoacoustic image of the left breast vascular (anterior-posterior projection) in a 57 year-old volunteer patient (from Kruger *et. al.*) [89].

Photoacoustic imaging of endogenous contrast has proven to be very useful. However, the use of an exogenous contrast agent with photoacoustic imaging can enhance the photoacoustic response, and potentially allow for molecular imaging or therapy [97,98]. Plasmonic nanoparticles are common photoacoustic contrast agents due to their large optical absorption efficiencies [99]. In addition, the optical absorption band of nanoparticles can be tuned by altering the material or the geometry [100]. Gold nanoparticles with various geometries (e.g. nanorods, nanocages, nanoshells and nanospheres) have been used to enhance photoacoustic contrast during imaging [101–104].

Dual mode photoacoustic and ultrasound contrast agents build on the microbubble construct to provide optical absorption. Optically absorbing dyes and plasmonic nanoparticles have been incorporated into the microbubble shell such that dual mode contrast was achieved [105–112].

Nanoparticle-loaded microbubbles have been studied for enhanced photothermal [113], optical scattering [110] and photoacoustic [111] properties. The ability to detect the contrast agent using a combination of acoustics and optics offers improved sensitivity and specificity.

Current targeted drug delivery methods rely on patient specific features and cannot accurately provide a specific dosage. A dual mode agent offers potentially powerful applications in drug delivery and therapy. Photoacoustics can image the spatial distribution of nanoparticles at depth in tissue [114–116]. Recently, photoacoustic imaging of gold nanorods was used to confirm the opening of the blood-brain-barrier [117]. The nanorods were co-administered with microbubbles and passively accumulated in the rat brain. A nanoparticle-loaded microbubble has the potential to be an exceptional theranostic (i.e. therapeutic and diagnostic) agent. Low intensity ultrasound could be used to track the agent to a desired location. High intensity ultrasound could then be used to fragment the shell and deliver nanoparticles. Photoacoustic imaging of the delivery process could potentially measure the accumulation of the nanoparticles. Hence, a nanoparticle-loaded microbubble could provide feedback on the delivered dosage and overcome current patient specific delivery issues.

1.7. Phase-change droplets

All of the applications utilizing microbubbles discussed thus far are limited to the vascular compartment due to the 1-10 μm size range. A promising contrast agent that offers additional benefits compared to microbubbles is phase-change droplets [118–120]. Phase-change agents contain a low-boiling point liquid fluorocarbon core with a stabilizing shell constructed from proteins, polymers or phospholipids. When excited with sufficient energy, the droplet core undergoes a phase change from liquid to gas. The benefits of a phase-change droplet stem from the ability to controllably initiate the phase change process.

In the liquid state, the droplet is small enough to extravasate leaky tumor vasculature [121,122]. Targeted delivery may be achieved by utilizing the enhanced permeability and retention (EPR) effect. Here, an agent, after intravenous injection, diffuses from the vasculature primarily at the tumor cite due to the leaky vasculature. Once the droplet extravasates, it may passively accumulate at the tumor site due to poor lymph drainage.

Another benefit of the liquid core is that droplets are more stable compared to microbubbles because dissolution of the liquid is considerably slower than the gas. The half-life of a microbubble is on the order of a few minutes [54] compared to recent studies on droplets with diameters in the one hundred nm range which remained stable *in vivo* for over an hour [119]. Once the droplet extravasates, the liquid core can be vaporized into gas and imaged. Hence, droplets enable interrogation of the tumor outside of the vascular and targeted drug delivery.

Currently acoustic [123–126] or optical energy [127–133] is used to vaporize the droplet core. Acoustic droplet vaporization utilizes an ultrasound field with a peak negative pressure capable of vaporizing the core. While the exact mechanism for acoustic vaporization is still unclear, super harmonic focusing of ultrasound appears to play a role [123,124]. For optical activation, pulsed laser illumination photothermally heats the droplet core above a certain threshold and the liquid vaporizes into a gas. However, the liquid fluorocarbon cores exhibit poor optical absorption, and optical absorbers, either dyes or plasmonic nanoparticles, are incorporated in the droplet core or on the droplet shell. This provides an additional benefit, as the optical absorbing species combined with the droplet may be imaged using photoacoustics, for example, before and after vaporization.

During phase change, the liquid undergoes explosive vaporization, resulting in a gas core diameter that is on the order of 5 times larger. The exact expansion ratio depends on the specific core material used. This process produces a large, nonlinear acoustic emission and improved

signal-to-noise ratio (SNR) may be achieved. For example, a recent study by Wei *et. al.* utilized a differential imaging strategy to improve the photoacoustic SNR in tissue phantoms [128]. Here, two images were taken at two different fluences. By normalizing each image by the fluence and taking the difference, the nonlinear droplet signal is increased relative to the linearly responding noise. In addition, droplet vaporization has been shown in improve high intensity focused ultrasound thermal therapy [134,135].

After vaporization, a microbubble remains and is able to provide ultrasound contrast [127]. Hence, an optically active phase-change agent may serve as a dual mode contrast agent. Vaporization of the droplet after extravasation in leaky tumor vasculature allows for acoustic interrogation of the tumor outside of the vascular compartment, something not possible with microbubbles alone.

1.8. Objectives of this dissertation

1.8.1. Scope

The main objective of this dissertation was to develop a nanoparticle-coated microbubble capable of acoustic and optical excitation. This work covers the theory of pulsed laser heating and fabrication of plasmonic microbubbles. Various experiments are presented that explore the unique properties of plasmonic microbubbles. A brief outline of the chapters are given.

Chapter 2 Modeling photothermal bubble oscillations: A model describing pulsed laser heating of spherical gold nanoparticles is discussed. The effect of size and pulse length on nanoparticle heating are studied. The thermal model is extended to a shelled bubble and the influence of bubble size on heating is examined. The heat flux into the gas core is used to estimate average temperature increases in the gas such that pulsed laser heating of a bubble can be coupled

into a modified Rayleigh-Plesset equation. The dynamics of a pulsed laser heated bubble are examined and the influence of the temporal profile of the heating function, bubble size, and shell properties are studied.

Chapter 3 Fabrication & characterization of plasmonic microbubbles: A conjugation scheme is developed to coat lipid-encapsulated microbubbles with plasmonic gold nanoparticles. Various physiochemical experiments are performed to verify nanoparticle loading on the microbubble shell. The photoacoustic response was characterized over a range of nanoparticle loading densities. The plasmonic microbubbles were used as contrast agents for *in vitro* imaging experiments.

Chapter 4 Optical activation of plasmonic microbubbles: Photoacoustic experiments are performed on individual plasmonic microbubbles. A microscope is used to track the bubble wall radius as a function of time using forward light scattering. The response of a plasmonic microbubble to pulsed laser illumination was measured. The eigenfrequency and vibrational amplitude of microbubbles in the 1-6 μm radius range was measured and compared to theory.

Chapter 5 Vaporization of condensed plasmonic microbubbles: Plasmonic microbubbles are condensed into droplets with liquid cores. The effect of the core material on vaporization threshold fluence was studied with a microscope. The transient response of the droplet vaporization was measured and ability to optically excite the vaporized bubble was demonstrated. The optical vaporization threshold for three different core materials, octafluoropropane, decafluorobutane and dodecafluoropentane was measured. Nanoparticle heating was proposed as a mechanism to explain the board transitions. In addition, the size dependence on vaporization threshold was discussed.

Chapter 6 Lipid-encapsulated microbubble shell elasticity: Preliminary results are presented on a theoretical model for the shell elasticity of a lipid-encapsulated microbubble. The model is based on intermolecular force fields and is derived from the Lennard-Jones potential. Experiments are performed on plasmonic microbubbles with four different lipid shells to validate the theoretical model.

1.8.2. Significance

A versatile approach was developed for the generation of plasmonic nanoparticle-templated microbubbles. Using an avidin-biotin method for nanoparticle conjugation to the microbubble shell, stoichiometric control over nanoparticle surface density and optical absorption was achieved. The plasmonic microbubbles are exceptionally efficient photoacoustic agents, with the photoacoustic response well above what was observed in free nanoparticle solutions or unconjugated mixtures of nanoparticles and microbubbles. Destruction of the microbubble gas core with high intensity ultrasound results in a marked reduction in the photoacoustic signal amplitude produced by plasmonic microbubbles. The latter result may find use as a powerful theranostic agent as the nanoparticle may be tracked photoacoustically before and after microbubble destruction. The plasmonic microbubbles were used as dual mode contrast agents to construct enhanced ultrasound and photoacoustic images *in vitro*.

For the first time, pulsed laser illumination was used to induce microbubble oscillations. The plasmonic microbubble was driven into resonance via photothermal heating of the nanoparticle shell. Using an optical scattering approach, the bubble oscillations can be tracked as a function of time. The eigenfrequency and vibrational amplitude of the bubbles can be measured with high resolution. For bubbles in the 1-10 μm diameter range the resonant frequency is in the low-megahertz regime. Considering the frequency dependent nature of acoustic attenuation in tissue,

where higher frequencies may be quickly attenuated, strong photoacoustic emission in the low-megahertz regime is desirable. The ability to optical excite and detect plasmonic microbubble oscillations with high fidelity and sensitivity offers a potentially powerful technique for the study of basic microbubble physics.

Application of high pressure to plasmonic microbubbles causes the gas core to condense creating optically active droplets in a metastable state. Pulsed laser illumination above a certain fluence threshold causes the liquid core to undergo explosive vaporization. The use of different, volatile perfluorocarbon gases allows for control over the threshold fluence required for vaporization. The fluence threshold was found to strongly depend on the volatility of the core with more volatile cores, with lower boiling points, vaporizing at lower fluence thresholds. Engineering optically active droplets with specific vaporization thresholds is a potentially powerful tool for imaging or therapeutic applications.

Preliminary results are given for a theoretical model that estimates of the shell elasticity for lipid-encapsulated microbubbles. The model was compared to experimental measurements on plasmonic microbubbles with different lipid shells. The theoretical model predicted that additional methylene groups would cause the shell elasticity to increase. This general trend was observed experimentally where the theoretical and experimental shell elasticity agreed within a factor of two.

References

[1] Gramiak, R., and Shah, P. M., 1968, "Echocardiography of the aortic root," Invest. Radiol., 3(5), pp. 356–366.

[2] Kwan, J. J., and Borden, M. A., 2010, "Microbubble Dissolution in a Multigas Environment," Langmuir, 26(9), pp. 6542–6548.

[3] Sarkar, K., Katiyar, A., and Jain, P., 2009, "Growth and Dissolution of an Encapsulated Contrast Microbubble: Effects of Encapsulation Permeability," Ultrasound Med. Biol., 35(8), pp. 1385–1396.

[4] Stride, E., and Saffari, N., 2003, "Microbubble ultrasound contrast agents: A review," Proc. Inst. Mech. Eng. [H], 217(6), pp. 429–447.

[5] Frinking, P. J. ., Bouakaz, A., Kirkhorn, J., Ten Cate, F. J., and de Jong, N., 2000, "Ultrasound contrast imaging: current and new potential methods," Ultrasound Med. Biol., 26(6), pp. 965–975.

[6] Simpson, D. H., Chin, C. T., and Burns, P. N., 1999, "Pulse inversion Doppler: a new method for detecting nonlinear echoes from microbubble contrast agents," IEEE Trans. Ultrason. Ferroelectr. Freq. Control, 46(2), pp. 372–382.

[7] Wilson, S. R., Jang, H.-J., Kim, T. K., Iijima, H., Kamiyama, N., and Burns, P. N., 2008, "Real-Time Temporal Maximum-Intensity-Projection Imaging of Hepatic Lesions with Contrast-Enhanced Sonography," Am. J. Roentgenol., 190(3), pp. 691–695.

[8] Porter, T. R., Oberdorfer, J., Rafter, P., Lof, J., and Xie, F., 2003, "Microbubble responses to a similar mechanical index with different real-time perfusion imaging techniques," Ultrasound Med. Biol., 29(8), pp. 1187–1192.

[9] Eckersley, R. J., Chin, C. T., and Burns, P. N., 2005, "Optimising phase and amplitude modulation schemes for imaging microbubble contrast agents at low acoustic power," Ultrasound Med. Biol., 31(2), pp. 213–219.

[10] Kruse, D. E., and Ferrara, K. W., 2005, "A new imaging strategy using wideband transient response of ultrasound contrast agents," IEEE Trans. Ultrason. Ferroelectr. Freq. Control, 52(8), pp. 1320–1329.

[11] Helfield, B. L., Cherin, E., Foster, F. S., and Goertz, D. E., 2012, "Investigating the Subharmonic Response of Individual Phospholipid Encapsulated Microbubbles at High Frequencies: A Comparative Study of Five Agents," Ultrasound Med. Biol., 38(5), pp. 846–863.

[12] Shekhar, H., Rychak, J. J., and Doyley, M. M., 2013, "Modifying the size distribution of microbubble contrast agents for high-frequency subharmonic imaging," Med. Phys., 40(8), p. 082903.

[13] Shankar, P. M., Krishna, P. D., and Newhouse, V. L., 1999, "Subharmonic backscattering from ultrasound contrast agents," J. Acoust. Soc. Am., 106(4), p. 2104.

[14] Biagi, E., Breschi, L., Vannacci, E., and Masotti, L., 2007, "Stable and transient subharmonic emissions from isolated contrast agent microbubbles," IEEE Trans. Ultrason. Ferroelectr. Freq. Control, 54(3), pp. 480–497.

[15] Sijl, J., Dollet, B., Overvelde, M., Garbin, V., Rozendal, T., Jong, N. de, Lohse, D., and Versluis, M., 2010, "Subharmonic behavior of phospholipid-coated ultrasound contrast agent microbubbles," J. Acoust. Soc. Am., 128(5), pp. 3239–3252.

[16] Goertz, D. E., Frijlink, M. E., Tempel, D., Bhagwandas, V., Gisolf, A., Krams, R., de Jong, N., and van der Steen, A. F. W., 2007, "Subharmonic Contrast Intravascular Ultrasound for Vasa Vasorum Imaging," Ultrasound Med. Biol., 33(12), pp. 1859–1872.

[17] Wilson, S. R., and Burns, P. N., 2010, "Microbubble-enhanced US in Body Imaging: What Role?," Radiology, 257(1), pp. 24–39.

[18] Kaul, S., 2008, "Myocardial Contrast Echocardiography A 25-Year Retrospective," Circulation, 118(3), pp. 291–308.

[19] Baish, J. W., Stylianopoulos, T., Lanning, R. M., Kamoun, W. S., Fukumura, D., Munn, L. L., and Jain, R. K., 2011, "Scaling rules for diffusive drug delivery in tumor and normal tissues," Proc. Natl. Acad. Sci., 108(5), pp. 1799–1803.

[20] Goldberg, B. B., Liu, J.-B., and Forsberg, F., 1994, "Ultrasound contrast agents: A review," Ultrasound Med. Biol., 20(4), pp. 319–333.

[21] Wei, K., Jayaweera, A. R., Firoozan, S., Linka, A., Skyba, D. M., and Kaul, S., 1998, "Quantification of Myocardial Blood Flow With Ultrasound-Induced Destruction of Microbubbles Administered as a Constant Venous Infusion," Circulation, 97(5), pp. 473–483.

[22] Unger, E. C., Porter, T., Culp, W., Labell, R., Matsunaga, T., and Zutshi, R., 2004, "Therapeutic applications of lipid-coated microbubbles," Adv. Drug Deliv. Rev., 56(9), pp. 1291–1314.

[23] Chen, H., Kreider, W., Brayman, A. A., Bailey, M. R., and Matula, T. J., 2011, "Blood Vessel Deformations on Microsecond Time Scales by Ultrasonic Cavitation," Phys. Rev. Lett., 106(3), p. 034301.

[24] Tung, Y.-S., Marquet, F., Teichert, T., Ferrera, V., and Konofagou, E. E., 2011, "Feasibility of noninvasive cavitation-guided blood-brain barrier opening using focused ultrasound and microbubbles in nonhuman primates," Appl. Phys. Lett., 98(16), pp. 163704–163704–3.

[25] McDannold, N., Arvanitis, C. D., Vykhodtseva, N., and Livingstone, M. S., 2012, "Temporary Disruption of the Blood–Brain Barrier by Use of Ultrasound and Microbubbles: Safety and Efficacy Evaluation in Rhesus Macaques," Cancer Res., 72(14), pp. 3652–3663.

[26] Tung, Y.-S., Vlachos, F., Feshitan, J. A., Borden, M. A., and Konofagou, E. E., 2011, "The mechanism of interaction between focused ultrasound and microbubbles in blood-brain barrier opening in mice," J. Acoust. Soc. Am., 130(5), pp. 3059–3067.

[27] Chadderdon, S. M., and Kaul, S., 2010, "Molecular imaging with contrast enhanced ultrasound," J. Nucl. Cardiol. Off. Publ. Am. Soc. Nucl. Cardiol., 17(4), pp. 667–677.

[28] Streeter, J. E., Gessner, R., Miles, I., and Dayton, P. A., 2010, "Improving Sensitivity in Ultrasound Molecular Imaging by Tailoring Contrast Agent Size Distribution: In Vivo Studies," Mol. Imaging, 9(2), pp. 87–95.

[29] Lindner, J. R., Coggins, M. P., Kaul, S., Klibanov, A. L., Brandenburger, G. H., and Ley, K., 2000, "Microbubble Persistence in the Microcirculation During Ischemia/Reperfusion and Inflammation Is Caused by Integrin- and Complement-Mediated Adherence to Activated Leukocytes," Circulation, 101(6), pp. 668–675.

[30] Klibanov, A. L., Rychak, J. J., Yang, W. C., Alikhani, S., Li, B., Acton, S., Lindner, J. R., Ley, K., and Kaul, S., 2006, "Targeted ultrasound contrast agent for molecular imaging of inflammation in high-shear flow," Contrast Media Mol. Imaging, 1(6), pp. 259–266.

[31] Inaba, Y., and Lindner, J. R., 2012, "Molecular imaging of disease with targeted contrast ultrasound imaging," Transl. Res., 159(3), pp. 140–148.

[32] Gessner, R., and Dayton, P. A., 2010, "Advances in Molecular Imaging with Ultrasound," Mol. Imaging, 9(3), pp. 117–127.

[33] Sirsi, S. R., Hernandez, S. L., Zielinski, L., Blomback, H., Koubaa, A., Synder, M., Homma, S., Kandel, J. J., Yamashiro, D. J., and Borden, M. A., 2012, "Polyplex-microbubble hybrids for ultrasound-guided plasmid DNA delivery to solid tumors," J. Controlled Release, 157(2), pp. 224–234.

[34] Mauldin, F. W. J., Dhanaliwala, A. H., Patil, A. V., and Hossack, J. A., 2012, "Real-time targeted molecular imaging using singular value spectra properties to isolate the adherent microbubble signal," Phys. Med. Biol., 57(16), p. 5275.

[35] Gessner, R. C., Streeter, J. E., Kothadia, R., Feingold, S., and Dayton, P. A., 2012, "An In Vivo Validation of the Application of Acoustic Radiation Force to Enhance the Diagnostic Utility of Molecular Imaging Using 3-D Ultrasound," Ultrasound Med. Biol., 38(4), pp. 651–660.

[36] Borden, M. A., Streeter, J. E., Sirsi, S., and Dayton, P. A., 2012, "In Vivo Demonstration of Cancer Molecular Imaging with Ultrasound Radiation Force and Buried-ligand Microbubbles.," Mol. Imaging, 12(0), pp. 1–8.

[37] Chen, C. C., and Borden, M. A., 2010, "Ligand Conjugation to Bimodal Poly(ethylene glycol) Brush Layers on Microbubbles," Langmuir, 26(16), pp. 13183–13194.

[38] Chen, C. C., Sirsi, S. R., Homma, S., and Borden, M. A., 2012, "Effect of Surface Architecture on In Vivo Ultrasound Contrast Persistence of Targeted Size-Selected Microbubbles," Ultrasound Med. Biol., 38(3), pp. 492–503.

[39] Sirsi, S. R., 2012, "Advances in Ultrasound Mediated Gene Therapy Using Microbubble Contrast Agents," Theranostics, 2(12), pp. 1208–1222.

[40] Unger, E. C., Hersh, E., Vannan, M., Matsunaga, T. O., and McCreery, T., 2001, "Local drug and gene delivery through microbubbles," Prog. Cardiovasc. Dis., 44(1), pp. 45–54.

[41] Caskey, C. F., Hu, X., and Ferrara, K. W., 2011, "Leveraging the power of ultrasound for therapeutic design and optimization," J. Controlled Release, 156(3), pp. 297–306.

[42] Dayton, P. A., Morgan, K. E., Klibanov, A. L., Brandenburger, G. H., and Ferrara, K. W., 1999, "Optical and acoustical observations of the effects of ultrasound on contrast agents," IEEE Trans. Ultrason. Ferroelectr. Freq. Control, 46(1), pp. 220–232.

[43] Chomas, J. E., Dayton, P. A., May, D., Allen, J., Klibanov, A., and Ferrara, K., 2000, "Optical observation of contrast agent destruction," Appl. Phys. Lett., 77(7), p. 1056.

[44] Chen, W.-S., Matula, T. J., Brayman, A. A., and Crum, L. A., 2003, "A comparison of the fragmentation thresholds and inertial cavitation doses of different ultrasound contrast agents," J. Acoust. Soc. Am., 113(1), pp. 643–651.

[45] Bloch, S. H., Wan, M., Dayton, P. A., and Ferrara, K. W., 2004, "Optical observation of lipid- and polymer-shelled ultrasound microbubble contrast agents," Appl. Phys. Lett., 84(4), p. 631.

[46] Thomas, D. H., Butler, M., Anderson, T., Emmer, M., Vos, H., Borden, M., Stride, E., de Jong, N., and Sboros, V., 2012, "The 'quasi-stable' lipid shelled microbubble in response to consecutive ultrasound pulses," Appl. Phys. Lett., 101(7), pp. 071601–071601–4.

[47] Thomas, D. H., Butler, M., Pelekasis, N., Anderson, T., Stride, E., and Sboros, V., 2013, "The acoustic signature of decaying resonant phospholipid microbubbles," Phys. Med. Biol., 58(3), p. 589.

[48] Luan, Y., Lajoinie, G., Gelderblom, E., Skachkov, I., van der Steen, A. F. W., Vos, H. J., Versluis, M., and De Jong, N., "Lipid Shedding from Single Oscillating Microbubbles," Ultrasound Med. Biol.

[49] Ferrara, K., Pollard, R., and Borden, M., 2007, "Ultrasound Microbubble Contrast Agents: Fundamentals and Application to Gene and Drug Delivery," Annu. Rev. Biomed. Eng., 9(1), pp. 415–447.

[50] Katiyar, A., Sarkar, K., and Jain, P., 2009, "Effects of encapsulation elasticity on the stability of an encapsulated microbubble," J. Colloid Interface Sci., (336), pp. 519–525.

[51] Kwan, J. J., and Borden, M. A., 2012, "Lipid monolayer dilatational mechanics during microbubble gas exchange," Soft Matter, 8(17), pp. 4756–4766.

[52] Stride, E., and Edirisinghe, M., 2008, "Novel microbubble preparation technologies," Soft Matter, 4(12), pp. 2350–2359.

[53] Dicker, S., Mleczko, M., Siepmann, M., Wallace, N., Sunny, Y., Bawiec, C. R., Schmitz, G., Lewin, P., and Wrenn, S. P., 2013, "Influence of Shell Composition on the Resonance Frequency of Microbubble Contrast Agents," Ultrasound Med. Biol., 39(7), pp. 1292–1302.

[54] Garg, S., Thomas, A. A., and Borden, M. A., 2013, "The effect of lipid monolayer in-plane rigidity on in vivo microbubble circulation persistence," Biomaterials, 34(28), pp. 6862–6870.

[55] Qin, S., Caskey, C. F., and Ferrara, K. W., 2009, "Ultrasound contrast microbubbles in imaging and therapy: physical principles and engineering," Phys. Med. Biol., 54(6), p. R27.

[56] Rayleigh, Lord, 1917, "VIII. On the pressure developed in a liquid during the collapse of a spherical cavity," Philos. Mag. Ser. 6, 34(200), pp. 94–98.

[57] Plesset, M. S., 1949, "The Dynamics of Cavitation Bubbles," J. Appl. Mech., 16(3), pp. 277–282.

[58] Ainslie, A, M., Leighton, and G, T., 2011, "Review of scattering and extinction cross-sections, damping factors, and resonance frequencies of a spherical gas bubble," J. Acoust. Soc. Am., 130(5), pp. 3184–3208.

[59] Prosperetti, A., 1977, "Thermal effects and damping mechanisms in the forced radial oscillations of gas bubbles in liquids," J. Acoust. Soc. Am., 61(1), pp. 17–27.

[60] Leighton, T., 1994, The Acoustic Bubble, Academic Press.

[61] Neppiras, E. A., 1980, "Acoustic cavitation," Phys. Rep., 61(3), pp. 159–251.

[62] Plesset, M. S., and Prosperetti, A., 1977, "Bubble Dynamics and Cavitation," Annu. Rev. Fluid Mech., 9(1), pp. 145–185.

[63] Hoff, L., 2001, Acoustic Characterization of Contrast Agents for Medical Ultrasound IMaging, Springer.

[64] Lauterborn, W., and Kurz, T., 2010, "Physics of bubble oscillations," Rep. Prog. Phys., 73(10), p. 106501.

[65] Marmottant, P., Meer, S. van der, Emmer, M., Versluis, M., Jong, N. de, Hilgenfeldt, S., and Lohse, D., 2005, "A model for large amplitude oscillations of coated bubbles accounting for buckling and rupture," J. Acoust. Soc. Am., 118(6), pp. 3499–3505.

[66] Doinikov, A. A., and Bouakaz, A., 2011, "Review of shell models for contrast agent microbubbles," IEEE Trans. Ultrason. Ferroelectr. Freq. Control, 58(5), pp. 981–993.

[67] Renaud, G., Bosch, J. G., Steen, A. F. W. van der, and Jong, N. de, 2012, "Chirp resonance spectroscopy of single lipid-coated microbubbles using an 'acoustical camera,'" J. Acoust. Soc. Am., 132(6), pp. EL470–EL475.

[68] Sijl, J., Vos, H. J., Rozendal, T., Jong, N. de, Lohse, D., and Versluis, M., 2011, "Combined optical and acoustical detection of single microbubble dynamics," J. Acoust. Soc. Am., 130(5), pp. 3271–3281.

[69] Thomas, D. H., Looney, P., Steel, R., Pelekasis, N., McDicken, W. N., Anderson, T., and Sboros, V., 2009, "Acoustic detection of microbubble resonance," Appl. Phys. Lett., 94(24), p. 243902.

[70] Helfield, B. L., and Goertz, D. E., 2013, "Nonlinear resonance behavior and linear shell estimates for Definity[trademark sign] and MicroMarker[trademark sign] assessed with acoustic microbubble spectroscopy," J. Acoust. Soc. Am., 133(2), pp. 1158–1168.

[71] Chen, X., Wang, J., Versluis, M., Jong, N. de, and Villanueva, F. S., 2013, "Ultra-fast bright field and fluorescence imaging of the dynamics of micrometer-sized objects," Rev. Sci. Instrum., 84(6), p. 063701.

[72] Gelderblom, E. C., Vos, H. J., Mastik, F., Faez, T., Luan, Y., Kokhuis, T. J. A., van der Steen, A. F. W., Lohse, D., De Jong, N., and Versluis, M., 2012, "Brandaris 128 ultra-high-speed imaging facility: 10 years of operation, updates, and enhanced features," Rev. Sci. Instrum., 83(10), pp. 103706–103706–11.

[73] Guan, J., and Matula, T. J., 2004, "Using light scattering to measure the response of individual ultrasound contrast microbubbles subjected to pulsed ultrasound in vitro," J. Acoust. Soc. Am., 116(5), p. 2832.

[74] Hsu, M. J., Eghtedari, M., Goodwin, A. P., Hall, D. J., Mattrey, R. F., and Esener, S. C., 2011, "Characterization of individual ultrasound microbubble dynamics with a light-scattering system," J. Biomed. Opt., 16(6), p. 067002.

[75] Holt, R. G., and Crum, L. A., 1990, "Mie scattering used to determine spherical bubble oscillations," Appl. Opt., 29(28), pp. 4182–4191.

[76] Versluis, M., Goertz, D. E., Palanchon, P., Heitman, I. L., van der Meer, S. M., Dollet, B., de Jong, N., and Lohse, D., 2010, "Microbubble shape oscillations excited through ultrasonic parametric driving," Phys. Rev. E, 82(2), p. 026321.

[77] Vos, H. J., Dollet, B., Versluis, M., and de Jong, N., 2011, "Nonspherical Shape Oscillations of Coated Microbubbles in Contact With a Wall," Ultrasound Med. Biol., 37(6), pp. 935–948.

[78] Van der Meer, S. M., Dollet, B., Voormolen, M. M., Chin, C. T., Bouakaz, A., de Jong, N., Versluis, M., and Lohse, D., 2007, "Microbubble spectroscopy of ultrasound contrast agents," J. Acoust. Soc. Am., 121(1), p. 648.

[79] Overvelde, M., Garbin, V., Sijl, J., Dollet, B., de Jong, N., Lohse, D., and Versluis, M., 2010, "Nonlinear Shell Behavior of Phospholipid-Coated Microbubbles," Ultrasound Med. Biol., 36(12), pp. 2080–2092.

[80] Renaud, G., Bosch, J. G., van der Steen, A. F. W., and de Jong, N., 2012, "An 'acoustical camera' for in vitro characterization of contrast agent microbubble vibrations," Appl. Phys. Lett., 100(10), pp. 101911–101911–4.

[81] De Jong, N., Emmer, M., Chin, C. T., Bouakaz, A., Mastik, F., Lohse, D., and Versluis, M., 2007, "'Compression-Only' Behavior of Phospholipid-Coated Contrast Bubbles," Ultrasound Med. Biol., 33(4), pp. 653–656.

[82] Morgan, K. E., Allen, J. S., Dayton, P. A., Chomas, J. E., Klibaov, A. L., and Ferrara, K. W., 2000, "Experimental and theoretical evaluation of microbubble behavior: effect of transmitted phase and bubble size," IEEE Trans. Ultrason. Ferroelectr. Freq. Control, 47(6), pp. 1494 –1509.

[83] Feshitan, J. A., Vlachos, F., Sirsi, S. R., Konofagou, E. E., and Borden, M. A., 2012, "Theranostic Gd(III)-lipid microbubbles for MRI-guided focused ultrasound surgery," Biomaterials, 33(1), pp. 247–255.

[84] Yang, F., "Superparamagnetic iron oxide nanoparticle-embedded encapsulated microbubbles as dual contrast agents of magnetic resonance and ultrasound imaging," BIOMATERIALS.

[85] Benchimol, M. J., Hsu, M. J., Schutt, C. E., Hall, D. J., Mattrey, R. F., and Esener, S. C., 2013, "Phospholipid/carbocyanine dye-shelled microbubbles as ultrasound-modulated fluorescent contrast agents," Soft Matter, 9(8), pp. 2384–2388.

[86] Yuan, B., Uchiyama, S., Liu, Y., Nguyen, K. T., and Alexandrakis, G., 2012, "High-resolution imaging in a deep turbid medium based on an ultrasound-switchable fluorescence technique," Appl. Phys. Lett., 101(3), p. 033703.

[87] Ke, H., Xing, Z., Zhao, B., Wang, J., Liu, J., Guo, C., Yue, X., Liu, S., Tang, Z., and Dai, Z., 2009, "Quantum-dot-modified microbubbles with bi-mode imaging capabilities," Nanotechnology, 20(42), p. 425105.

[88] Sorace, A. G., Saini, R., Rosenthal, E., Warram, J. M., Zinn, K. R., and Hoyt, K., 2013, "Optical fluorescent imaging to monitor temporal effects of microbubble-mediated ultrasound therapy," IEEE Trans. Ultrason. Ferroelectr. Freq. Control, 60(2), pp. 281–289.

[89] Kruger, R. A., Lam, R. B., Reinecke, D. R., Rio, S. P. D., and Doyle, R. P., 2010, "Photoacoustic angiography of the breast," Med. Phys., 37(11), pp. 6096–6100.

[90] Kim, C., Erpelding, T. N., Jankovic, L., Pashley, M. D., and Wang, L. V., 2010, "Deeply penetrating in vivo photoacoustic imaging using a clinical ultrasound array system," Biomed. Opt. Express, 1(1), pp. 278–284.

[91] Beard, P., 2011, "Biomedical photoacoustic imaging," Interface Focus, 1(4), pp. 602 –631.

[92] Wang, L. V., and Hu, S., 2012, "Photoacoustic Tomography: In Vivo Imaging from Organelles to Organs," Science, 335(6075), pp. 1458 –1462.

[93] Xu, M., and Wang, L. V., 2006, "Photoacoustic imaging in biomedicine," Rev. Sci. Instrum., 77(4), p. 041101.

[94] Wang, L. V., 2009, "Multiscale photoacoustic microscopy and computed tomography," Nat Photon, 3(9), pp. 503–509.

[95] Li, C., and Wang, L. V., 2009, "Photoacoustic tomography and sensing in biomedicine," Phys. Med. Biol., 54(19), pp. R59–R97.

[96] Wang, L. V., and Gao, L., 2014, "Photoacoustic Microscopy and Computed Tomography: From Bench to Bedside," Annu. Rev. Biomed. Eng., 16(1), pp. 155–185.

[97] Luke, G. P., Yeager, D., and Emelianov, S. Y., 2012, "Biomedical Applications of Photoacoustic Imaging with Exogenous Contrast Agents," Ann. Biomed. Eng., 40(2), pp. 422–437.

[98] Emelianov, S. Y., Li, P.-C., and O'Donnell, M., 2009, "Photoacoustics for molecular imaging and therapy," Phys. Today, 62(8), pp. 34–39.

[99] Yang, X., Stein, E., Ashkenazi, S., and Wang, L., 2009, "Nanoparticles for photoacoustic imaging," Wiley Interdiscip Rev Nanomed Nanobiotechnol, 1(4), pp. 360–368.

[100] Jain, P. K., Lee, K. S., El-Sayed, I. H., and El-Sayed, M. A., 2006, "Calculated Absorption and Scattering Properties of Gold Nanoparticles of Different Size, Shape, and Composition: Applications in Biological Imaging and Biomedicine," J. Phys. Chem. B, 110(14), pp. 7238–7248.

[101] Yang, X., Skrabalak, S. E., Li, Z.-Y., Xia, Y., and Wang, L. V., 2007, "Photoacoustic Tomography of a Rat Cerebral Cortex in vivo with Au Nanocages as an Optical Contrast Agent," Nano Lett., 7(12), pp. 3798–3802.

[102] Lu, W., Huang, Q., Ku, G., Wen, X., Zhou, M., Guzatov, D., Brecht, P., Su, R., Oraevsky, A., Wang, L. V., and Li, C., 2010, "Photoacoustic imaging of living mouse brain vasculature using hollow gold nanospheres," Biomaterials, 31(9), pp. 2617–2626.

[103] Eghtedari, M., Oraevsky, A., Copland, J. A., Kotov, N. A., Conjusteau, A., and Motamedi, M., 2007, "High Sensitivity of In Vivo Detection of Gold Nanorods Using a Laser Optoacoustic Imaging System," Nano Lett, 7(7), pp. 1914–1918.

[104] Wang, Y., Xie, X., Wang, X., Ku, G., Gill, K. L., O'Neal, D. P., Stoica, G., and Wang, L. V., 2004, "Photoacoustic Tomography of a Nanoshell Contrast Agent in the in Vivo Rat Brain," Nano Lett, 4(9), pp. 1689–1692.

[105] Kim, C., Qin, R., Xu, J. S., Wang, L. V., and Xu, R., 2010, "Multifunctional microbubbles and nanobubbles for photoacoustic and ultrasound imaging," J. Biomed. Opt., 15(1), p. 010510.

[106] Huynh, E., Lovell, J. F., Helfield, B. L., Jeon, M., Kim, C., Goertz, D. E., Wilson, B. C., and Zheng, G., 2012, "Porphyrin Shell Microbubbles with Intrinsic Ultrasound and Photoacoustic Properties," J. Am. Chem. Soc.

[107] Jeon, M., Song, W., Huynh, E., Kim, J., Kim, J., Helfield, B. L., Leung, B. Y. C., Goertz, D. E., Zheng, G., Oh, J., Lovell, J. F., and Kim, C., 2014, "Methylene blue microbubbles as a model dual-modality contrast agent for ultrasound and activatable photoacoustic imaging," J. Biomed. Opt., 19(1), pp. 016005–016005.

[108] Seo, M., Gorelikov, I., Williams, R., and Matsuura, N., 2010, "Microfluidic Assembly of Monodisperse, Nanoparticle-Incorporated Perfluorocarbon Microbubbles for Medical Imaging and Therapy," Langmuir, 26(17), pp. 13855–13860.

[109] Park, J. I., Jagadeesan, D., Williams, R., Oakden, W., Chung, S., Stanisz, G. J., and Kumacheva, E., 2010, "Microbubbles Loaded with Nanoparticles: A Route to Multiple Imaging Modalities," ACS Nano, 4(11), pp. 6579–6586.

[110] Yang, F., Wang, Q., Gu, Z., Fang, K., Marriott, G., and Gu, N., 2013, "Silver Nanoparticle-Embedded Microbubble as a Dual-Mode Ultrasound and Optical Imaging Probe," ACS Appl. Mater. Interfaces, 5(18), pp. 9217–9223.

[111] Dove, J. D., Murray, T. W., and Borden, M. A., 2013, "Enhanced photoacoustic response with plasmonic nanoparticle-templated microbubbles," Soft Matter, 9(32), pp. 7743–7750.

[112] Stride, E., Pancholi, K., Edirisinghe, M. ., and Samarasinghe, S., 2008, "Increasing the nonlinear character of microbubble oscillations at low acoustic pressures," J. R. Soc. Interface, 5(24), pp. 807 –811.

[113] Wang, Y.-H., Li, P.-C., Liao, A.-H., Chen, J.-H., and Wang, C.-R. C., 2012, "Photoacoustic/ultrasound dual-modality contrast agent and its application to thermotherapy," J Biomed Opt, 17(4).

[114] Agarwal, A., Huang, S. W., O'Donnell, M., Day, K. C., Day, M., Kotov, N., and Ashkenazi, S., 2007, "Targeted gold nanorod contrast agent for prostate cancer detection by photoacoustic imaging," J. Appl. Phys., 102(6), pp. 064701–064701–4.

[115] Mallidi, S., Larson, T., Tam, J., Joshi, P. P., Karpiouk, A., Sokolov, K., and Emelianov, S., 2011, "Multiwavelength Photoacoustic Imaging and Plasmon Resonance Coupling of Gold Nanoparticles for Selective Detection of Cancer," Nano Lett, 9(8), pp. 2825–2831.

[116] Kim, C., Cho, E. C., Chen, J., Song, K. H., Au, L., Favazza, C., Zhang, Q., Cobley, C. M., Gao, F., Xia, Y., and Wang, L. V., 2010, "In Vivo Molecular Photoacoustic Tomography of Melanomas Targeted by Bioconjugated Gold Nanocages," ACS Nano, 4(8), pp. 4559–4564.

[117] Wang, P.-H., Liu, H.-L., Hsu, P.-H., Lin, C.-Y., Chris Wang, C.-R., Chen, P.-Y., Wei, K.-C., Yen, T.-C., and Li, M.-L., 2012, "Gold-nanorod contrast-enhanced photoacoustic micro-

imaging of focused-ultrasound induced blood-brain-barrier opening in a rat model," J. Biomed. Opt., 17(6), p. 061222.

[118] Matsunaga, T. O., Sheeran, P. S., Luois, S., Streeter, J. E., Mullin, L. B., Banerjee, B., and Dayton, P. A., 2012, "Phase-Change Nanoparticles Using Highly Volatile Perfluorocarbons: Toward a Platform for Extravascular Ultrasound Imaging," Theranostics, 2(12), pp. 1185–1198.

[119] Sheeran, P. S., and Dayton, P. A., 2014, "Improving the Performance of Phase-Change Perfluorocarbon Droplets for Medical Ultrasonography: Current Progress, Challenges, and Prospects," Scientifica, 2014, p. e579684.

[120] Rapoport, N., 2012, "Phase-shift, stimuli-responsive perfluorocarbon nanodroplets for drug delivery to cancer," Wiley Interdiscip. Rev. Nanomed. Nanobiotechnol., 4(5), pp. 492–510.

[121] Brown, J. M., and Giaccia, A. J., 1998, "The Unique Physiology of Solid Tumors: Opportunities (and Problems) for Cancer Therapy," Cancer Res., 58(7), pp. 1408–1416.

[122] Iyer, A. K., Khaled, G., Fang, J., and Maeda, H., 2006, "Exploiting the enhanced permeability and retention effect for tumor targeting," Drug Discov. Today, 11(17–18), pp. 812–818.

[123] Shpak, O., Verweij, M., Vos, H. J., Jong, N. de, Lohse, D., and Versluis, M., 2014, "Acoustic droplet vaporization is initiated by superharmonic focusing," Proc. Natl. Acad. Sci., 111(5), pp. 1697–1702.

[124] Li, D. S., Kripfgans, O. D., Fabiilli, M. L., Fowlkes, J. B., and Bull, J. L., 2014, "Initial nucleation site formation due to acoustic droplet vaporization," Appl. Phys. Lett., 104(6), p. 063703.

[125] Sheeran, P. S., Luois, S., Dayton, P. A., and Matsunaga, T. O., 2011, "Formulation and Acoustic Studies of a New Phase-Shift Agent for Diagnostic and Therapeutic Ultrasound," Langmuir, 27(17), pp. 10412–10420.

[126] Sheeran, P. S., Wong, V. P., Luois, S., McFarland, R. J., Ross, W. D., Feingold, S., Matsunaga, T. O., and Dayton, P. A., 2011, "Decafluorobutane as a phase-change contrast agent for low-energy extravascular ultrasonic imaging," Ultrasound Med. Biol., 37(9), pp. 1518–1530.

[127] Wilson, K., Homan, K., and Emelianov, S., 2012, "Biomedical photoacoustics beyond thermal expansion using triggered nanodroplet vaporization for contrast-enhanced imaging," Nat Commun, 3, p. 618.

[128] Wei, C., Lombardo, M., Larson-Smith, K., Pelivanov, I., Perez, C., Xia, J., Matula, T., Pozzo, D., and O'Donnell, M., 2014, "Nonlinear contrast enhancement in photoacoustic molecular imaging with gold nanosphere encapsulated nanoemulsions," Appl. Phys. Lett., 104(3), p. 033701.

[129] Hannah, A., Luke, G., Wilson, K., Homan, K., and Emelianov, S., 2014, "Indocyanine Green-Loaded Photoacoustic Nanodroplets: Dual Contrast Nanoconstructs for Enhanced Photoacoustic and Ultrasound Imaging," ACS Nano, 8(1), pp. 250–259.

[130] Hannah, A. S., VanderLaan, D., Chen, Y.-S., and Emelianov, S. Y., 2014, "Photoacoustic and ultrasound imaging using dual contrast perfluorocarbon nanodroplets triggered by laser pulses at 1064 nm," Biomed. Opt. Express, 5(9), pp. 3042–3052.

[131] Strohm, E., Rui, M., Gorelikov, I., Matsuura, N., and Kolios, M., 2011, "Vaporization of perfluorocarbon droplets using optical irradiation," Biomed. Opt. Express, 2(6), pp. 1432–1442.

[132] Jian, J., Liu, C., Gong, Y., Su, L., Zhang, B., Wang, Z., wang, D., Zhou, Y., Xu, F., Li, P., Zheng, Y., Song, L., and Zhou, X., 2014, "India Ink Incorporated Multifunctional Phase-transition Nanodroplets for Photoacoustic/Ultrasound Dual-modality Imaging and Photoacoustic Effect Based Tumor Therapy," Theranostics, 4(10), pp. 1026–1038.

[133] Wei, C., Xia, J., Lombardo, M., Perez, C., Arnal, B., Larson-Smith, K., Pelivanov, I., Matula, T., Pozzo, L., and O?Donnell, M., 2014, "Laser-induced cavitation in nanoemulsion with gold nanospheres for blood clot disruption: in vitro results," Opt. Lett., 39(9), pp. 2599–2602.

[134] Zhang, P., and Porter, T., 2010, "An in vitro Study of a Phase-Shift Nanoemulsion: A Potential Nucleation Agent for Bubble-Enhanced HIFU Tumor Ablation," Ultrasound Med. Biol., 36(11), pp. 1856–1866.

[135] Phillips, L. C., Puett, C., Sheeran, P. S., Dayton, P. A., Miller, G. W., and Matsunaga, T. O., 2013, "Phase-shift perfluorocarbon agents enhance high intensity focused ultrasound thermal delivery with reduced near-field heating," J. Acoust. Soc. Am., 134(2), pp. 1473–1482.

Chapter 2

Modeling photothermal bubble oscillations

2.1. Introduction

Heat generation by nanoparticles illuminated with either continuous wave or pulsed lasers can be used for therapeutic or biomedical imaging applications. For therapeutic applications, the heat generated by the nanoparticles is used to provide selective heating to diseased tissue [1–3]. In certain cases, the heat production can be extremely intense causing a phase change of the surrounding water resulting in cavitation of a vapor bubble which can produce intense mechanical shock local to the nanoparticle [4,5]. For imaging applications, the enhanced heating provided by the nanoparticles improves the photoacoustic contrast [6,7]. This allows for deep tissue photoacoustic imaging or molecular imaging of a certain diseased tissue [8].

In this chapter, a model is presented where pulsed laser illumination causes a gold nanoparticle-coated microbubble to oscillate. There are three distinct physical processes that must occur in order for a pulsed laser source to drive a nanoparticle-coated bubble into oscillation. First, the optical

pulse must be absorbed and converted into heat by the nanoparticle shell. Then the heat generated in the shell needs to diffuse into the gas core of the bubble. Lastly, the heated gas core must rapidly expand causing the bubble to oscillate once the laser pulse is terminated. Optical absorption by a nanoparticle is explained by Mie theory. The specific details of Mie theory have been omitted here as several reviews and texts have already covered the details [9–11]. Instead the focus is placed on pulsed laser heating of nanoparticles, a nanoparticle-coated bubbles and coupling the heated gas core into the dynamics of a bubble. First, pulsed laser heating of individual nanoparticles is examined. Then the model is expanded to a shelled bubble and the temperature rise in the gas core is calculated. Finally, the heated gas core is coupled into a modified Rayielgh-Plesset equation specific for lipid-shelled microbubbles.

2.2. Photothermal response of a nanoparticle

2.2.1. Thermal model for a nanosphere

Nanoparticles efficiently convert the absorbed optical energy into heat, which then diffuses into the surrounding medium. Using linear heat transfer theory, a solution for the transient thermal field surrounding a nanoparticle can be obtained. The focus will be placed on spherical nanoparticles where an analytical solution exists. The heat equation for a gold nanosphere surrounded by a fluid can be represented in spherical coordinates (r, θ, φ) with angular symmetry and can be expressed as:

$$\frac{1}{r}\frac{\partial}{\partial r^2}\left(rT_L\right)=\frac{1}{\alpha_L}\frac{\partial T_L}{\partial t} \tag{2.1}$$

$$\frac{1}{r}\frac{\partial}{\partial r^2}\left(rT_{NP}\right)-\frac{1}{\alpha_{NP}}\frac{\partial T_{NP}}{\partial t}=-\frac{Q(t)}{k_{NP}} \tag{2.2}$$

Here, T is the temperature, α is the thermal diffusivity, k is the thermal conductivity and $Q(t)$ is the heating function. The subscripts, NP and L, represent the nanoparticle and the liquid, respectively. Because of the length and time scales involved in pulsed laser heating of nanoparticles, the heat transfer process is purely conductive and convection is neglected. This assumption is valid if the Grashof number is sufficiently small (<1). The Grashof number is a ratio of the buoyancy to viscous forces and scales by the 3rd power of the characteristic length. Using the nanoparticle radius (2.5 nm) as the characteristic length, the Grashof number is found to be <<1 allowing for convection to be neglected.

The heating function for pulsed laser illumination describes conversion of the optical absorption rate to the thermal power density (thermal energy per unit volume and time) within the nanoparticle. Because the quantum yield exhibited by metallic nanoparticles is very low (~10^{-6}) (i.e. the nanoparticle does not fluoresce), the conversion of optical absorption to heating can be assumed to be unity [12]. The form for the heating function can then be expressed as:

$$Q(t) = \frac{F_0 C_{abs}}{4/3\,\pi R_{NP}^3}\, g(t) \tag{2.3}$$

Where F_0 is the fluence of the incident laser pulse, C_{abs} is the optical absorption coefficient calculated from Mie theory, R_{NP} is the radius of the nanoparticle, and $g(t)$ is the temporal profile of the pulsed laser having been normalized in time (i.e. the integrated temporal response represents unity). Here, $F_0 C_{abs}$ is the amount of optical energy the nanoparticle can absorb, which is distributed over the nanoparticle volume to give an absorbed energy density. The temporal profile of the pulsed laser can be described as [13]:

$$g(t) = 2\frac{t^3}{\tau_p{}^4} e^{-\left(\frac{t}{\tau}\right)^2} \tag{2.4}$$

Here, τ_p is the pulse width. The boundary conditions at the gold-liquid interface are continuous temperature and heat flux; and are expressed as:

$$T_L\,|_{r=R_{NP}} = T_{NP}\,|_{r=R_{NP}} \tag{2.5}$$

$$k_L \frac{\partial T_L}{\partial r}\bigg|_{r=R_{NP}} = k_{NP} \frac{\partial T_{NP}}{\partial r}\bigg|_{r=R_{NP}} \tag{2.6}$$

The temperature of the nanoparticle and liquid are initially equal to the ambient temperature (T_0) before the optical pulse arrives.

$$T_L\,|_{t=0} = T_{NP}\,|_{t=0} = T_0 \tag{2.7}$$

For convenience, the substitution, $\theta = T\text{-}T_0$, can be used such that the initial condition is $\theta = 0$ at $t=0$. To solve Eqns. (2.1) and (2.2), integral transform techniques are used. Here, the Laplace transform is used to transform the time domain into the s-domain.

$$\frac{\partial}{\partial r^2}\left(r\tilde{\theta}_L\right) - r\left(\frac{s}{\alpha_L}\right)\tilde{\theta}_L = 0 \tag{2.8}$$

$$\frac{\partial^2}{\partial r^2}\left(r\tilde{\theta}_{NP}\right) - r\left(\frac{s}{\alpha_{NP}}\right)\tilde{\theta}_{NP} = -\frac{r\tilde{Q}(s)}{k_{NP}} \tag{2.9}$$

Where $\tilde{\theta}$ is the Laplace transformed temperature.

The functional form of the q-switched laser pulse provided in Eq. (2.3) does not have an explicit Laplace transform. Therefore, a slightly different functional form for the temporal profile of laser pulse will be used as described below.

$$\hat{g}(t) = \frac{5^7}{6!}\frac{t^6}{\tau^7}e^{-\left(\frac{5t}{\tau}\right)} \tag{2.10}$$

The temporal profile of each pulse is shown in Fig. 2.1. The error in using Eqn. (2.10) instead of (2.3) is minimal; it approaches 5% for times greater than 2 τ_p and then approaches zero for times greater than 3 τ_p.

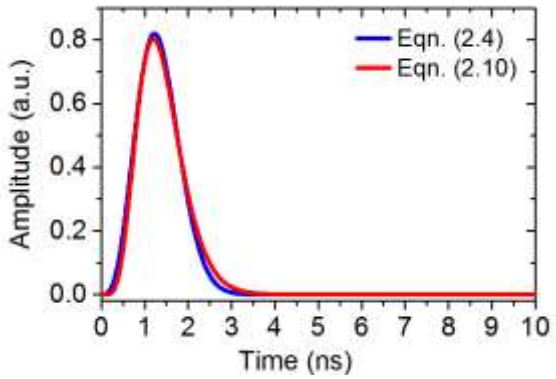

Figure 2.1 Temporal profile of the laser pulse (τ_p = 1 ns) described in Eqn. 2.4 which does not have a Laplace transform and Eqn. 2.10 which does.

The Laplace transform of the heating function can be expressed as:

$$\tilde{Q}(s) = \frac{5^7}{6!}\frac{F_0 C_{abs}}{4/3\pi R_{NP}^3}\left(5+s\tau\right)^{-7} \tag{2.11}$$

Applying the boundary conditions, Eqns. (2.5) and (2.6), to Eqns. (2.8) and (2.9) with the condition that as r approaches zero the temperature must be defined (i.e. not approach infinity), the transient thermal field in the surrounding liquid and inside the nanoparticle takes the form:

$$\tilde{\theta}_L(r,s)=\frac{\tilde{Q}(s)}{k_{NP}p_{NP}^2}\frac{R_{NP}}{r}\frac{\left[\sinh(p_{NP}R_{NP})-p_{NP}R_{NP}\cosh(p_{NP}R_{NP})\right]e^{-p_L(r-R_{NP})}}{(1+p_LR_{NP})M(s)} \tag{2.12}$$

$$\tilde{\theta}_{NP}(r,s)=\frac{\tilde{Q}(s)}{k_{NP}p_{NP}^2}\left[1+\frac{k_L}{k_p}\frac{R\sinh(p_{NP}r)}{rM(s)}\right] \tag{2.13}$$

Where,

$$M(s)=\frac{\sinh(p_{NP}R_{NP})-p_{NP}R_{NP}\cosh(p_{NP}R_{NP})}{1+p_LR_{NP}}-\frac{k_L}{k_{NP}}\sinh(p_{NP}R_{NP}) \tag{2.14}$$

$$p_{NP}=\sqrt{\frac{s}{\alpha_{NP}}} \tag{2.15}$$

$$p_L=\sqrt{\frac{s}{\alpha_L}} \tag{2.16}$$

The temporal solution can be obtained through a numerical Laplace inversion of Eqns. (2.12) and (2.13). Using this solution the optical heating provided by a nanoparticle can be examined.

2.2.2. Pulsed laser heating of a gold nanosphere

The ability of a nanoparticle to undergo pulsed laser heating and dissipate the heat into the surrounding environment is shown in Fig. 2.2. The densites of gold and water are 19,300 kg/m^3 and 1000 kg/m^3, respectively. The specific heats of gold and water are 129 J/kg*K and 4,181 J/kg*K, respectively. The thermal conductivities of the gold and water are 318 W/m*K (the thermal diffusivity is 1.277x10^{-4} m^2/s) and 0.6 W/m*K (the thermal diffusivity is 1.437x10^{-7} m^2/s), respectively. The illumination source was a 1 ns optical pulse with a fluence of 1 mJ/cm^2 and a wavelength of 532 nm. The absorption efficiency (absorption cross-section normalized by

nanoparticle cross-section) for a 5 nm gold sphere illuminated at 532 nm in water was estimated from Mie theory to be 0.2921 [9].

Fig. 2.2(a) shows the calculated temperature rise at the nanoparticle surface as a function of time. Initially the nanoparticle heating follows the heating function (optical pulse profile) reaching a maximum temperature of 2 K. The maximum temperature occurs slightly after the optical pulse has reached a maximum. This is because heat dissipation from the nanoparticle is occurring slightly slower than heat generation within the nanoparticle. This is evident as the nanoparticle cools, where the cooling rate lags the optical pulse.

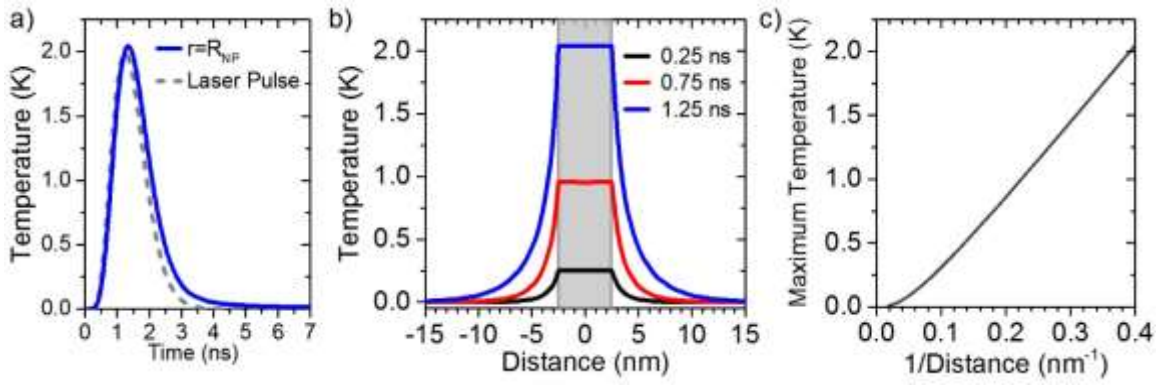

Figure 2.2 (a) Transient thermal response of a 5-nm gold sphere to pulsed laser illumination is shown as the solid blue line. The dashed line is the temporal profile of the pulsed laser. (b) The spatial thermal profile at three different times. The shaded grey area represents the gold nanoparticle and the white is water. (c) The maximum temperature rise in the water as function of inverse distance from the nanoparticle center.

The spatial thermal profile is shown at three different times in Fig. 2.2(b). The thermal diffusion length of the gold nanoparticle for a 1 ns optical pulse $\left(l_T = \sqrt{\alpha_{NP}\tau_p} = 350\text{nm}\right)$ is much larger than the nanoparticle radius (2.5 nm) and the temperature within the nanoparticle is observed to be uniform. The ability of the nanoparticle to heat the surrounding liquid is evident, even at early times.

The thermal diffusion length of the water is 12 nm, and as a result, the temperature profile in water decays away from the nanoparticle surface. Referring to Eq. (2.12), the decay rate is found to scale with the inverse distance from the nanoparticle center. The maximum temperature rise is plotted as a function of inverse distance in Fig. 2.2(c) and is observed to increase with inverse distance.

The effect of nanoparticle diameter on heat generation is explored in Fig. 2.3. The pulse length and fluence were held constant at 1 ns and 1 mJ/cm^2, respectively. The temperature rise at the nanoparticle surface is plotted for varying diameters in Fig. 2.3(a). The largest nanoparticle was 100 nm in diameter but did not provide the largest temperature increase, only heating to 54.2 K. The smallest nanoparticle was 5 nm in diameter and provided the lowest temperature rise of 2K. The largest temperature increase occurred for a nanoparticle with a diameter of 65 nm, with a maximum temperature of 87.9 K.

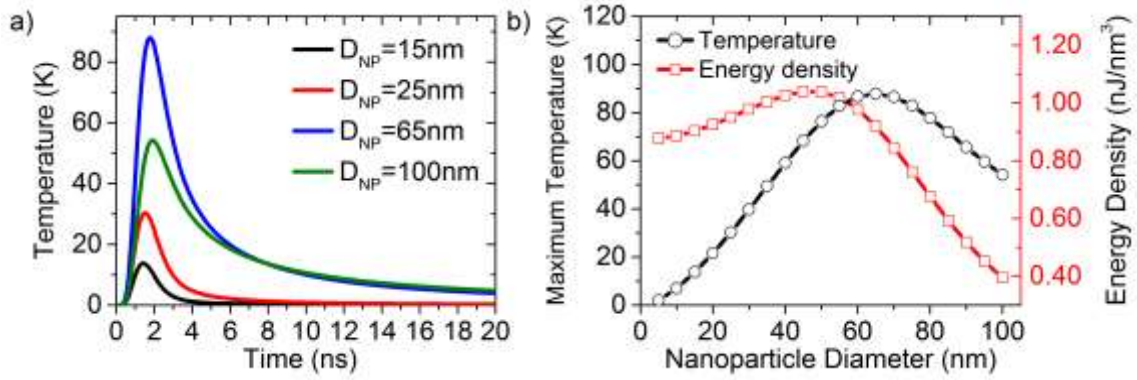

Figure 2.3 (a) Transient thermal response of gold spherical nanoparticles with different diameters. (b) The maximum temperature as a function of nanoparticle diameter plotted as circles with ordinate on the left side of the plot, and the absorbed energy density of the nanoparticle plotted as the squares with the ordinate on the right side of the plot.

The maximum temperature and absorbed energy density are plotted as a function of nanoparticle diameter in Fig. 2.3(b). The absorbed energy density increases as the absorption cross

section (calculated from Mie Theory) increases with nanoparticle diameter. Referring to Eqn. (2.3), the heating function scales directly with the absorbed energy density. Hence, as the absorbed energy density of the nanoparticle increases, so does the maximum temperature. This trend continues until the nanoparticle diameter is 50 nm, where larger nanoparticles have a lower absorbed energy density but display a greater maximum temperature. This is due to slower heat dissipation into the surrounding medium as the volume-to-surface ratio increases with nanoparticle size.

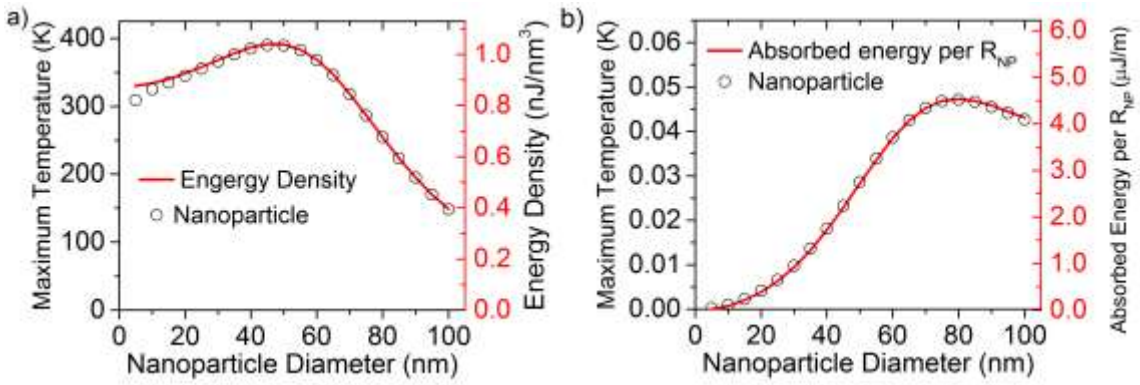

Figure 2.4 The maximum temperature as a function of nanoparticle diameter, where the line corresponds to the right ordinate and the circles are for the left ordinate. (a) A laser pulse width of 10 fs where heat transfer has minimal effect with the solid red line representing the absorbed energy density ($\tau_p << t_{exch}$**)** (b) for a laser pulse of 10 μs where the generation and dissipation reach a steady state with the solid red line representing the absorbed energy density normalized by nanoparticle surface area ($\tau_p >> t_{exch}$).

As the nanoparticle absorbs the optical pulse and increases in temperature, heat begins to dissipate into the surrounding medium. The heat generation and dissipation rates determine when the maximum temperature is reached. The characteristic time for the heat exchange from the nanoparticle to the surrounding medium is $t_{exh} \sim R_{NP}^2 / 4\alpha_L$ [14]. For a gold sphere with a 5 nm diameter, t_{exh} is 0.01 ns as compared to the 100 nm diameter gold sphere where t_{exh} is 4.4 ns.

Only when the optical pulse width is much smaller than heat exchange process ($\tau_p << t_{exch}$) will the maximum temperature rise follow the absorbed energy density, shown as the red solid line in Fig. 2.4(a). In this regime, nanoparticle heating is much faster than the heat transfer with the medium. This results in enhanced heating of the nanoparticle, and in the limiting case (no heat transfer), the maximum temperature approaches E_{abs}/C_{NP}, where C_{NP} is the heat capacity of the nanoparticle. This occurs for a gold sphere with a 45 nm diameter and results in a maximum achievable temperature rise of 414 K. By setting the pulse to 10 fs ($\tau_p << t_{exch}$), the maximum temperature rise follows the absorbed energy density and is plotted in Fig. 2.4 (a).

When $\tau_p >> t_{exch}$ the heating approaches a quasi-stationary regime [14]. Here, the rate of heat dissipation and generation reach a steady state. Heat generation scales with the absorbed energy density. However, the dissipation rate scales with the surface area of the nanoparticle. Hence, the maximum temperature rise in the quasi-stationary regime scales with absorbed energy normalized by the nanoparticle radius ($F_0 C_{abs}/R_{NP}$), which is shown as the red solid line in Fig. 2.4(b). In this regime, a gold sphere with an 80 nm diameter achieves the maximum the temperature, as shown in Fig. 2.4 (b). In addition, the temperature rise is diminished in this regime as heat dissipation plays a major role.

When τ_p approaches t_{exch}, nanoparticle heating and dissipation are on the same time scale. Here, the maximum temperature the nanoparticle can achieve depends on the pulse length and thermal diffusivity of the medium varying from the case of no heat diffusion (45 nm) to the quasi-stationary case (80 nm).

The dependence on the pulse width is shown in Fig. 2.5. Here, the nanoparticle diameter and fluence were held constant at 5 nm and 1 mJ/cm^2, respectively. The transient temperature rise at the nanoparticle surface is plotted for different optical pulse widths as shown in Fig. 2.5 (a). The

heating function described in Eqn. (2.10) has an inverse dependence on the pulse length. Hence, for the same nanoparticle, the maximum temperature rise increases linearly as the pulse length decreases, as shown in Fig. 2.5 (b). Thus, enhanced heating is a benefit from utilizing a pulsed laser with a shorter pulse width.

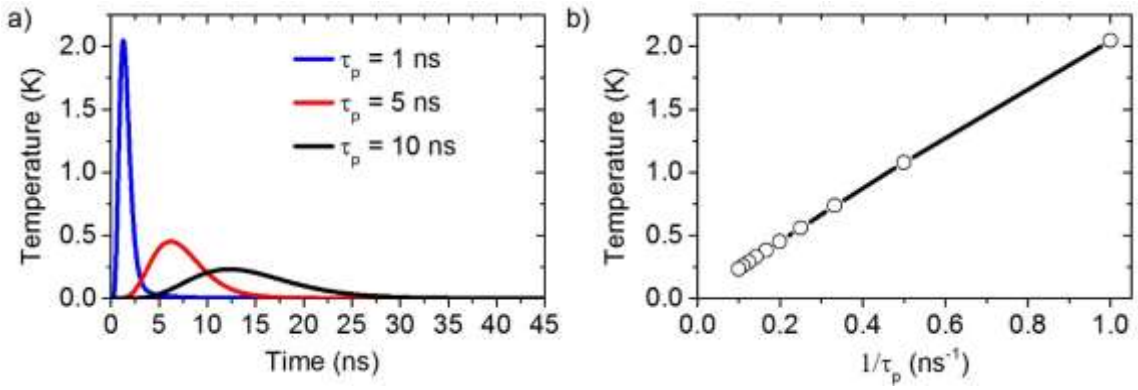

Figure 2.5 (a) Transient temperature rise at the surface of a 5 nm gold spherical nanoparticle excited by optical pulses with different temporal widths. (b) The maximum temperature as a function of inverse pulse length.

In the analysis above, it was demonstrated that pulsed laser illumination of gold spherical nanoparticles causes heating within the nanoparticle and the surrounding liquid, with the maximum temperature rise in the liquid occurring at the nanoparticle surface. The heating within a nanoparticle was found to remain relatively constant. The maximum temperature rise depends on the nanoparticle diameter, pulse length and the rate of heat exchange with the surrounding medium.

2.3. Photothermal response of a nanoparticle-coated gas bubble

2.3.1. Thermal model for a shelled bubble

The photothermal heating of a nanoparticle-coated bubble can now be considered. Here, it is assumed that the gold nanoparticles coat the bubble at a high surface density, such that the problem

can be simplified to a thin shell of gold surrounding a bubble submersed in water. The equations governing heat diffusion are expressed as:

$$\frac{1}{r}\frac{\partial}{\partial r^2}\left(rT_g\right)=\frac{1}{\alpha_g}\frac{\partial T_g}{\partial t} \tag{2.17}$$

$$\frac{1}{r}\frac{\partial}{\partial r^2}\left(rT_S\right)-\frac{1}{\alpha_{NP}}\frac{\partial T_S}{\partial t}=-\frac{Q(t)}{k_{NP}} \tag{2.18}$$

$$\frac{1}{r}\frac{\partial}{\partial r^2}\left(rT_L\right)=\frac{1}{\alpha_L}\frac{\partial T_L}{\partial t} \tag{2.19}$$

Here the subscripts, *g*, *S*, and *L* represent the gas, shell, and liquid, respectively. The heating function *Q(t)* now represents the thermal power distributed throughout the shell volume and can be represented as:

$$Q(t)=\frac{E_{abs}}{4\pi R_g^2\left(2R_{NP}\right)}\hat{g}(t) \tag{2.20}$$

Here, R_g is the radius of the gas bubble, the shell thickness is equal the diameter of the nanoparticle (here it is assumed $R_{NP}<<R_g$) and E_{abs} is the amount of absorbed optical energy. Assuming the nanoparticles coat the bubble with a surface density ρ_{Load}, the absorbed optical energy can be expressed as:

$$E_{abs}=F_0 C_{abs}\rho_{Load}\,4\pi R_g^2 \tag{2.21}$$

Combing Eqns. (2.20) and (2.21) gives:

$$Q(t) = \frac{F_0 C_{abs} \rho_{Load}}{2R_{NP}} \hat{g}(t) \tag{2.22}$$

The heating function for a nanoparticle-templated microbubble is found to scale with nanoparticle loading density, ρ_{Load}, and is independent of bubble size.

The boundary conditions are the continuity of temperature and heat flux across the interfaces, and are expressed as:

$$T_g \mid_{r=R_g} = T_S \mid_{r=R_g} \tag{2.23}$$

$$T_S \mid_{r=R_g+2R_{NP}} = T_L \mid_{r=R_g+2R_{NP}} \tag{2.24}$$

$$k_g \left.\frac{\partial T_g}{\partial r}\right|_{r=R_g} = k_S \left.\frac{\partial T_S}{\partial r}\right|_{r=R_g} \tag{2.25}$$

$$k_S \left.\frac{\partial T_S}{\partial r}\right|_{r=R_g+2R_{NP}} = k_L \left.\frac{\partial T_L}{\partial r}\right|_{r=R_g+2R_{NP}} \tag{2.26}$$

To solve Eqns. (2.17) to (2.19), the Laplace transform is used. The solutions for the transformed temperatures of the gas, shell and liquid can be expressed in the Laplace domain (using the subsition, $\theta = T\text{-}T_0$) as:

$$\tilde{\theta}_g(r,s) = \frac{1}{r} A_1 \sinh(p_g r) \tag{2.27}$$

$$\tilde{\theta}_S(r,s) = \frac{1}{r}\left[A_2 \sinh(p_S r) + A_3 \cosh(p_S r)\right] + \frac{\tilde{Q}(s)}{k_2 p_L^2} \tag{2.28}$$

$$\tilde{\theta}_g(r,s)=\frac{1}{r}A_4 e^{-(p_L r)} \tag{2.29}$$

Where,

$$p_S=\sqrt{\frac{s}{\alpha_{NP}}} \tag{2.30}$$

$$p_g=\sqrt{\frac{s}{\alpha_g}} \tag{2.31}$$

Applying the boundary conditions, Eqns. (2.23) to (2.26), to Eqns. (2.27) to (2.29), the unknowns, A_1, A_2, A_3, and A_4 can be solved and are represented in matrix form below.

$$\mathbf{M}=\begin{bmatrix} \frac{\sinh(p_g R_g)}{R_g} & -\frac{\sinh(p_S R_g)}{R_g} & -\frac{\cosh(p_S R_g)}{R_g} & 0 \\ 0 & \frac{\sinh(p_S R_O)}{R_O} & \frac{\cosh(p_S R_g)}{R_O} & \frac{e^{-(p_L R_O)}}{R_O} \\ \frac{k_g p_g}{R_g}\cosh(p_g R_g)-\frac{k_g}{R_g^2}\sinh(p_g R_g) & \frac{k_S}{R_g^2}\sinh(p_S R_g)-\frac{k_S p_S}{R_g}\cosh(p_S R_g) & \frac{k_S}{R_g^2}\cosh(p_S R_g)-\frac{k_S p_S}{R_g}\sinh(p_S R_g) & 0 \\ 0 & \frac{k_S p_S}{R_O}\cosh(p_S R_O)-\frac{k_S}{R_O^2}\sinh(p_S R_O) & \frac{k_S p_S}{R_O}\sinh(p_S R_O)-\frac{k_S}{R_O^2}\cosh(p_S R_O) & \frac{k_L}{R_O}e^{-(p_L R_O)}\left(p_3+\frac{1}{R_O}\right) \end{bmatrix} \tag{2.32}$$

Such that:

$$\mathbf{M}\begin{bmatrix} A_1 \\ A_2 \\ A_3 \\ A_4 \end{bmatrix}=\begin{bmatrix} -\frac{\tilde{Q}(s)}{k_s p_S^2} \\ \frac{\tilde{Q}(s)}{k_s p_S^2} \\ 0 \\ 0 \end{bmatrix} \tag{2.33}$$

The temporal solution for pulsed laser heating of a shelled bubble can be obtained through use of a numerical Laplace inversion.

2.3.2. Pulsed laser heating of a shelled bubble

Fig. 2.6 shows the thermal response of a nanoparticle-coated bubble irradiated with a 1 ns optical pulse at 1 mJ/cm^2. The nanoparticle surface density, ρ_{Load}, was 15,000 nanoparticles per μm^2. The gas core was decafluorobutane (C_4F_{10}) with a density of 9.7 kg/m^3, a specific heat of 791 J/kg*K, and a thermal conductivity of 0.0133 W/m*K (the thermal diffusivity was 1.73x10^{-6} m^2/s). The maximum temperature was observed to occur at the gas-shell interface. Similar to a nanoparticle, heat dissipates into the surrounding medium immediately. Due to the order of magnitude difference in thermal diffusivities, heat can propagate into the gas core quicker than the water. For example, in 10 ns the thermal diffusion length is 132 nm and 38 nm for the core and water, respectively. This is evident in Fig. 2.6 (red line is for t = 10 ns) when comparing the temperature profile in the gas and water where the heat has propagated much further in the gas than the water.

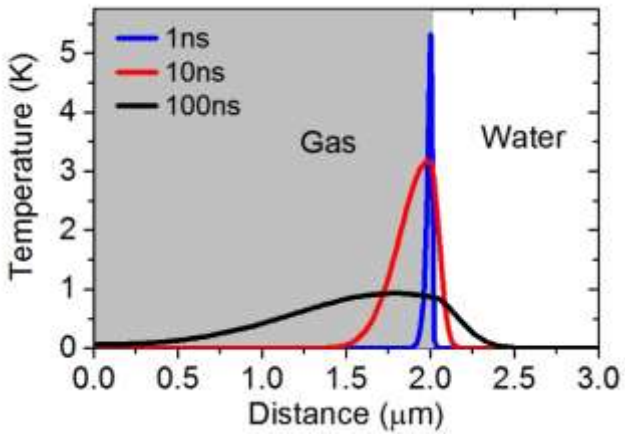

Figure 2.6 The spatial profile of the temperature rise in the gas and liquid at varying times for a gold-shelled bubble with a radius of 2 μm irradiated with a 1 ns pulse at 1 mJ/cm^2.

The total thermal energy delivered to the gas can be calculated by considering the temperature gradient created in the gas core. Essentially, the presence of the heated shell creates a heat flux into the gas that can be expressed as:

$$q(t) = -k_g \left. \frac{\partial T_g(r,t)}{\partial r} \right|_{r=R_g} \tag{2.34}$$

The total heat flux can be integrated over time to quantify the thermal energy delivered, *W*, to the gas core.

$$W(t) = \int_0^t 4\pi R_g^2 q(t) dt \tag{2.35}$$

Fig. 2.7 (a) shows the resulting heat flux into the gas core from a 1 ns optical pulse at 1 mJ/cm^2. The heat flux follows the optical pulse profile, with the majority of heat delivered within the first few nanoseconds. At later times, heat transfer from the gas core into the surrounding medium occurs, which results in a negative heat flux shown in inset of Fig. 2.7 (a). Note the initial heat flux into the bubble (heat generation) is orders of magnitude greater than the heat flux out of the bubble (cooling), but the timescales associated with cooling are orders of magnitude longer than the heating.

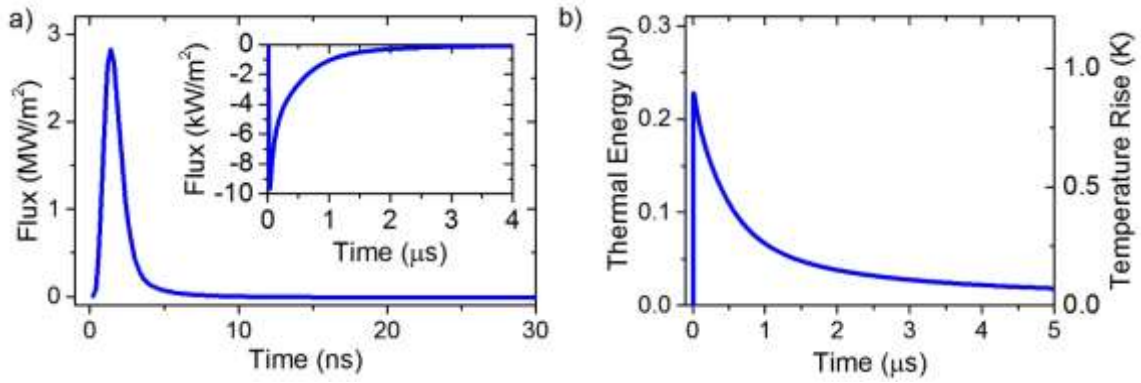

Figure 2.7 (a) The resulting heat flux at the gas boundary and the inset is the heat flux rescaled to visualize the negative flux. (b) The total thermal energy deposited into the gas core as the left ordinate and the temperature rise for gas core as the right ordinate.

The thermal energy delivered to the gas core is plotted in Fig. 2.7 (b). The initial positive heat flux results in a rapid increase in thermal energy. As time increases the negative heat flux (heat transfer out of gas core) results in the thermal decay in Fig. 2.7 (b). The right ordinate corresponds to the rise in temperature due to the increase in thermal energy. This is a simple conversion taking into account the heat capacity of the gas core such that the average temperature of the gas core, T_B, can be calculated.

$$T_B(t) = \frac{W(t)}{C_{p,g}}\left(\frac{BT_0}{P_{e,g}\,4\pi R_g^3}\right) \tag{2.36}$$

Where, $C_{p,g}$ is the specific heat of the gas, $P_{e,g}$ is the pressure of the gas core when the bubble is at rest, T_0 is the temperature of the gas core, and B is the ideal gas constant. It is should be noted that this is a simplification that ignores the time scales associated with heat diffusion into the gas core (there is no dependence on r). However, the estimates for the thermal energy delivered to the gas core are still correct. It is the spatial distribution of the thermal energy that has been simplified. This model gives a first approximation of the temperature rise in the gas core for a nanoparticle-coated bubble illuminated with a pulsed laser.

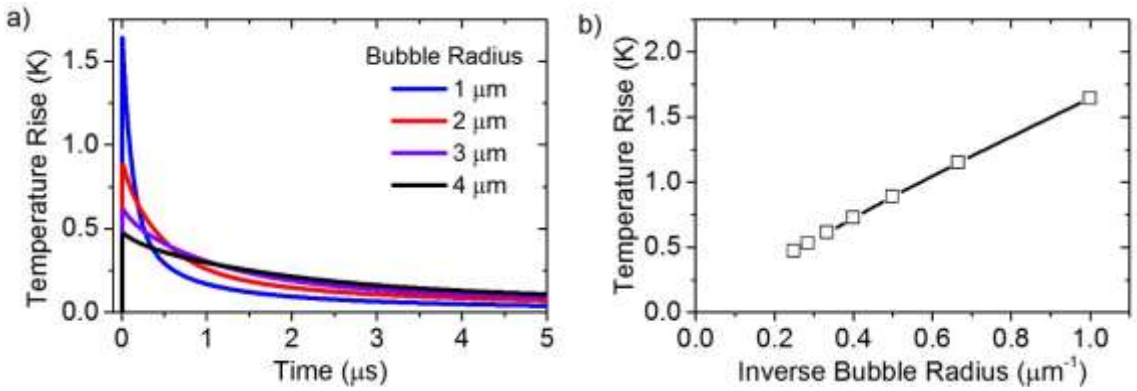

Figure 2.8 (a) The transient temperature rise in the gas core for bubbles with different radii (b) the maximum temperature rise plotted against inverse bubble radius.

The average temperature rise of the gas core for different sized bubbles illuminated with a 1 ns laser pulse at 1 mJ/cm^2 is shown in Fig. 2.8 (a). Here, the nanoparticle shell consisted of 5 nm gold spheres with a loading density of ρ_{NP} =15,000 nanoparticles per μm^2. The maximum temperature occurs within the first few nanoseconds (corresponding to the pulse length) after which the heat slowly diffuses away from the gas core on the μs time scale. As the bubble radius is increased, the maximum temperature increases and the rate of heat dissipation is diminished. As a result, the larger the bubble, the closer the temperature profile approaches a step rise in temperature.

Maximum temperature is plotted as a function of inverse bubble radius is shown in Fig. 2.8(b). Here, the maximum temperature increases as the bubble decreases in size. Referring to Eqn. (2.22) the heating function is found to not depend on bubble radius, rather the loading density of the nanoparticles. Thus, for a constant nanoparticle surface density, the heat flux into the bubble is independent of bubble radius. The total energy delivered to the bubbles (Eqn, (2.35)) increased with R_g^2. However, the temperature in the bubble core described by Eqn. (2.36) distributes the thermal energy over the volume of the gas (R_g^3) leading to a temperature rise in the core that depends on R_g^{-1}.

2.4. Photothermal oscillations of a gas bubble

2.4.1. Modified Rayleigh-Plesset model for a heated bubble

The dynamic response of the gas bubble to a pulsed laser will now be examined. As the gas core of the bubble heats up the volume increases, driving bubble oscillation. The pressure of the gas core at equilibrium can be expressed as:

$$P_{g,e} = P_0 + \frac{2\sigma}{R_0} \tag{2.37}$$

Where P_0 is the ambient hydrostatic pressure of the liquid, σ is the surface tension of the gas liquid interface, and R_0 is the resting radius of the gas bubble (equal to R_g in the sections describing bubble heating). Eqn. (2.37) is the Laplace equation which describes the increase in pressure due to a curved surface in tension. Assuming the gas obeys the ideal gas law, the pressure of the gas core during laser heating can be expressed as:

$$P_g(t) = \frac{nBT_g(t)}{V(t)} \tag{2.38}$$

Where, n is the number of moles of the gas, B is the ideal gas constant, and V is the volume of the gas core. The use of the ideal gas law is only valid for timescales much slower than the heat diffusion through the gas core. Given the time and length scales associated with laser heating, the gas is not expected to behave ideally. However, to a first approximation the ideal gas law is used, and an average temperature increase in the gas, Eqn. (2.36), can be calculated to estimate a pressure increase. Assuming the gas is not diffusing into or out of the core, this quantity can be related to the state of the bubble at equilibrium through the following expression:

$$P_g(t) = P_{g,e}\left(\frac{V_0}{V(t)}\right)\left(\frac{T(t)}{T_0}\right) \tag{2.39}$$

Combining Eqns. (2.39) and (2.37) the pressure of the liquid, P_L, just surrounding the bubble can be expressed as:

$$P_L(t) = P_{g,e}\left(\frac{R_0}{R}\right)^3\left(\frac{T(t)}{T_0}\right) - \frac{2\sigma}{R} \tag{2.40}$$

Here, R has been introduced as the time dependent radius of the bubble. Eqn. (2.37) can be combined with Eqn. (2.40) giving:

$$P_L(t) = \left(P_0 + \frac{2\sigma}{R_0} \right) \left(\frac{R_0}{R} \right)^3 \left(\frac{T(t)}{T_0} \right) - \frac{2\sigma}{R} \tag{2.41}$$

While the bubble is oscillating, there is a restoring force due to the shell elasticity. In addition, there are viscous losses in both the surrounding fluid and the shell. Balancing the normal stresses at the interface results in the following expression [15]:

$$P_g(t) - P_L(t) = 4\chi \left(\frac{1}{R_0} - \frac{1}{R} \right) + 4\mu \frac{\dot{R}}{R} + 4\kappa_s \frac{\dot{R}}{R^2} \tag{2.42}$$

Here, the χ is the shell elasticity, μ is the viscosity of the liquid, κ_s is the viscosity in the shell and the dot represents a derivative with respect to time. The Rayleigh-Plesset equation models the dynamics of an oscillating spherical gas bubble and is described as [16–18]:

$$\frac{P_L(t) - P_0}{\rho_L} = \frac{3\dot{R}^2}{2} + R\ddot{R} \tag{2.43}$$

Where, ρ_L is the density of the liquid. Combining the Rayleigh-Plesset equation, Eqn. (2.43), to the dynamics of the heated gas as described by Eqn. (2.41) and with Eqn. (2.42), which describes the boundary of the gas liquid interface, an expression for the dynamic response of a heated gas bubble can be described as:

$$\frac{3\dot{R}^2}{2} + R\ddot{R} = \frac{1}{\rho_L} \left[\left(P_0 + \frac{2\sigma}{R_0} \right) \left(\frac{R_0}{R} \right)^3 \left(\frac{T(t)}{T_0} \right) - P_0 - 4\chi \left(\frac{1}{R_0} - \frac{1}{R} \right) - 4\mu \frac{\dot{R}}{R} - 4\kappa_s \frac{\dot{R}}{R^2} \right] \tag{2.44}$$

The above equation can be solved using a finite-difference numerical approach. The initial conditions are:

$$R = R_0 \big|_{t=0} \tag{2.45}$$

$$\dot{R} = 0 \big|_{t=0} \tag{2.46}$$

Using the expression for the temperature of the gas bubble, Eqn. 2.36, the dynamic response of a bubble to a pulsed laser heating can be examined.

2.4.2. Dynamic response of a pulsed laser heated bubble

The transient response of a bubble due to pulsed laser heating is shown in Fig. 2.9. Here, the ambient pressure was 1 atm (0.83 bar in Boulder, CO), ρ_L was 1000 kg/m^3, μ was 8.9x10^{-4} Pa*s, χ was 1.0 N/m, κ_s was 5x10^{-9} kg/s, σ was assumed to be negligible [19] and T_0 was 298 K. The heating, $T(t)$, was calculated from Eqn. (2.36), with an optical pulse width of 1 ns and a fluence of 1 mJ/cm^2. The ability to optically drive a bubble to oscillate is demonstrated in Fig. 2.9. Here, the amplitude of the bubble oscillations are shown as radial displacement where 0 corresponds to the resting radius of the bubble. Initially, the bubble expands due to the heated gas core reaching the maximum radial displacement on the first oscillation. Due to viscous losses in the shell and liquid the subsequent oscillations decay over time. The oscillation frequency increases as bubble size is decreased. In addition, the amplitude of the radial oscillations increases with increasing bubble diameter. These features will be studied in more detail below.

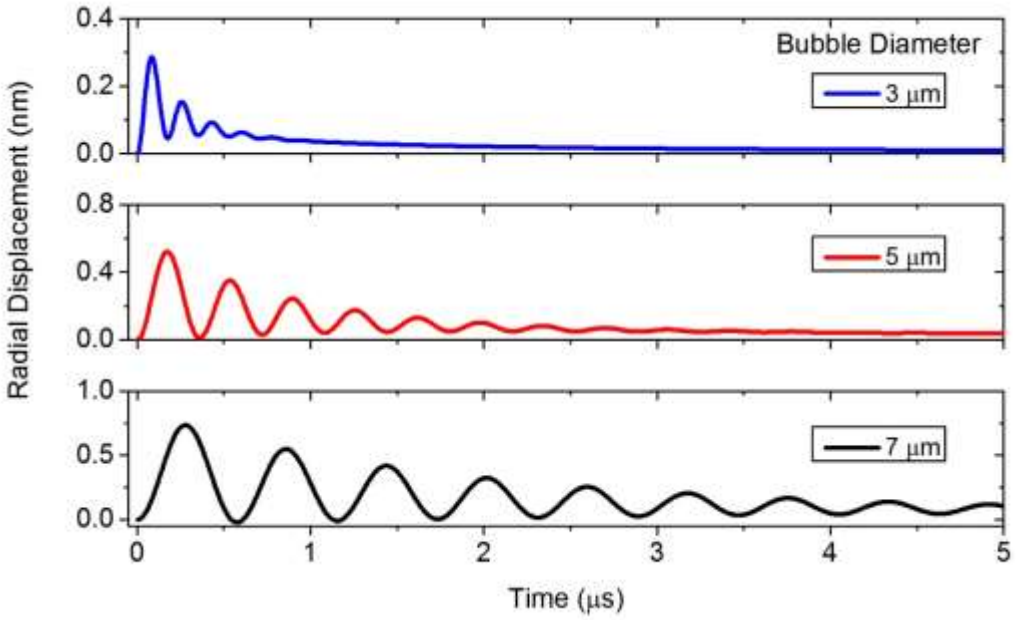

Figure 2.9 The transient response of a bubble (diameter of 3, 5, and 7 μm) to pulsed laser illumination.

The resonant frequency, which was measured by performing a Fourier transform on the time-domain response (Fig. 2.9), is plotted in Fig. 2.10 (a). In addition, the eigenfrequencies (undamped natural frequency) are plotted in Fig 2.9 (a) and are related to the resonant frequency by the following expression:

$$\omega_0 = \frac{\omega_r}{\sqrt{1-\zeta^2}} \tag{2.47}$$

The eigenfrequency can be found by linearizing Eqn. (2.44) for small amplitude fluctuations, $x(t)$, about the resting radius R_0 ($R = x(t)+R_0$), such that the dynamic motion of the bubble wall can be expressed as a second order system. The eigenfrequency from the linearized model can be expressed as:

$$f_0 = \frac{1}{2\pi}\sqrt{\frac{1}{\rho_L R_0^2}\left(3P_0 + \frac{4(\sigma+\chi)}{R_0}\right)} \tag{2.48}$$

Comparing the predicted eigenfrequencies (Eqn. (2.48)) from the linearized model to the resonant frequency of the time-domain response, the differences are close to those predicted by Eqn. (2.47), except for the smallest bubble. The predicted resonance frequency for the bubble with a 1 μm radius is lower than expected. This is because the temporal profile of the heating function (Fig. 2.8 (a)) is between a step and impulse response. Consequently, Eqn. (2.47) is only valid when considering an impulse or step drive and does not predict the shift for the smallest bubble.

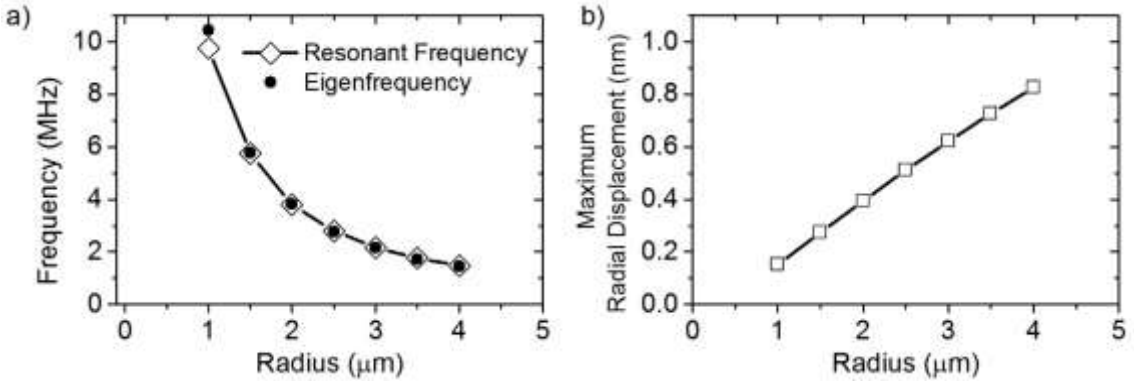

Figure 2.10 (a) The resonant frequency, open diamonds, of the bubble oscillations and eigenfrequency, black circles, are plotted as a function of bubble radius. (b) The maximum radial displacement plotted as a function of bubble radius.

The result that the resonant frequencies fall into the low megahertz regime is important. The acoustic attenuation of tissue is frequency dependent, with high frequencies receiving more attenuation. An optically driven bubble produces a strong response in the low megahertz regime, where acoustic attenuation is minimal. This is a promising result for deep tissue imaging. In addition, the importance of a monomodal size distribution is evident from Fig. 2.10 (a). The signal-to-noise ratio may be improved by minimizing destructive interference effects from bubbles with different radii by utilizing a population of bubbles with similar sizes. Here, the photoacoustic

emission from similar sized bubbles (spaced less than half a wavelength away $c_s/2f_0$, where c_s is the speed of sound in water) will sum coherently leading to an improved photoacoustic response from the population of bubbles.

As the bubble diameter is increased, the amplitude of the oscillations increases as shown in Fig. 2.10 (b). This is in contrast to the maximum temperature the gas core reaches, which decreases as bubble size increases (Fig. 2.8 (b)). However, the maximum temperature is only one factor to consider for the heating function. Another important factor is the amount of time the bubble core is heated.

2.4.3. Influence of the heating function

The temporal profile of the heating function can influence the response of a bubble. To understand the impact of the heating function on bubble response the two limiting cases, an impulse heating function and a step rise in temperature, are studied. Here, the amplitude of the heating function follows the same surface area to volume relationship shown in Fig. 2.8 (b). The time the gas core is heated is varied from the two extremes, an impulse and step heating function as shown in Fig. 2.10 (a).

In the case of the step increase in temperature, the maximum radial displacement increases with bubble radius, as shown as the red circles in Fig. 2.11 (b). Following the ideal gas law ($V/V_0=T/T_0$), it is apparent that given a constant increase in temperature, the larger the bubble, the larger the change in radius. However, if T decreases with bubble size, the maximum radial displacement can increase, remain constant or decrease depending on the rate at which T decreases with bubble size. The simulations show that as T decreases following the surface area to volume relationship (Fig. 2.8(b)), the maximum radial displacement increases with increasing radius.

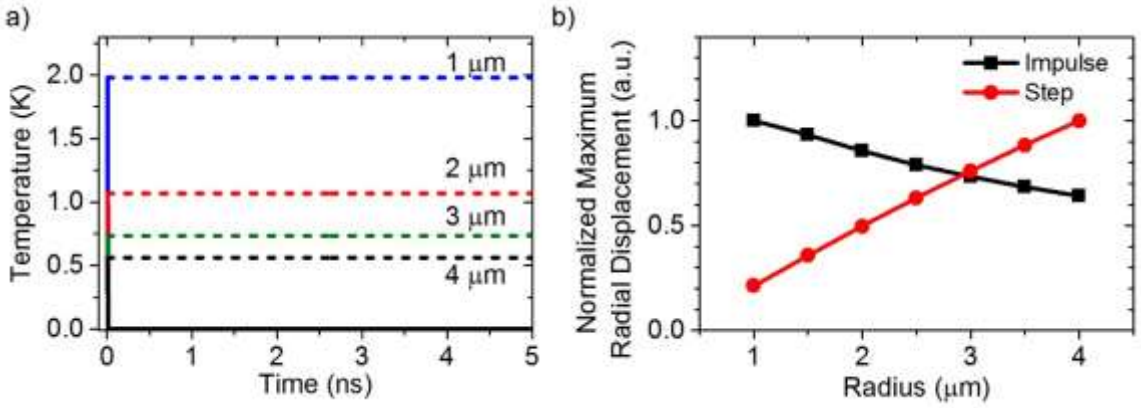

Figure 2.11 (a) Impulse, solid lines, and step, dashed lines, heating functions. (b) The maximum amplitude of bubble oscillations for impulse and step heating functions.

For an impulse heating function, the maximum radial displacement decreases with increasing radius, shown as the black squares in Fig. 2.11 (b). Here, the bubble response follows a similar trend as the maximum temperature rise in the gas core (i.e. the amplitude of the forcing function). In this regime, all the heating occurs before any of the bubbles complete one oscillation. As a result, the maximum radial displacements follow a similar trend as the maximum temperature, shown in Fig. 2.8 (b).

The temporal profile of the heating function is found to have a strong effect on the trend of maximum radial displacement and bubble size. The maximum radial displacement can scale with bubble radius, or inversely with bubble radius, depending on the amount of time the gas core is heated. Using the heat flux described in Eqn. (2.34) to drive the bubble, the maximum radial displacement increases with bubble size.

2.4.4. Influence of shell properties on bubble dynamics

The dynamic response of the bubble wall radius depends on the properties of the encapsulating shell. From Eqn. (2.44) the shell viscosity, κ_s, influences the damping of the bubble oscillations.

This is evident in the time-domain response of a bubble with a 2.5 μm resting radius plotted in Fig. 2.12 (a). Here, the shell elasticity is held constant at 1.0 N/m and the shell viscosity was varied. As the shell viscosity increases from 0 to $1x10^{-8}$ kg/s, the settling time for the bubble response decreases.

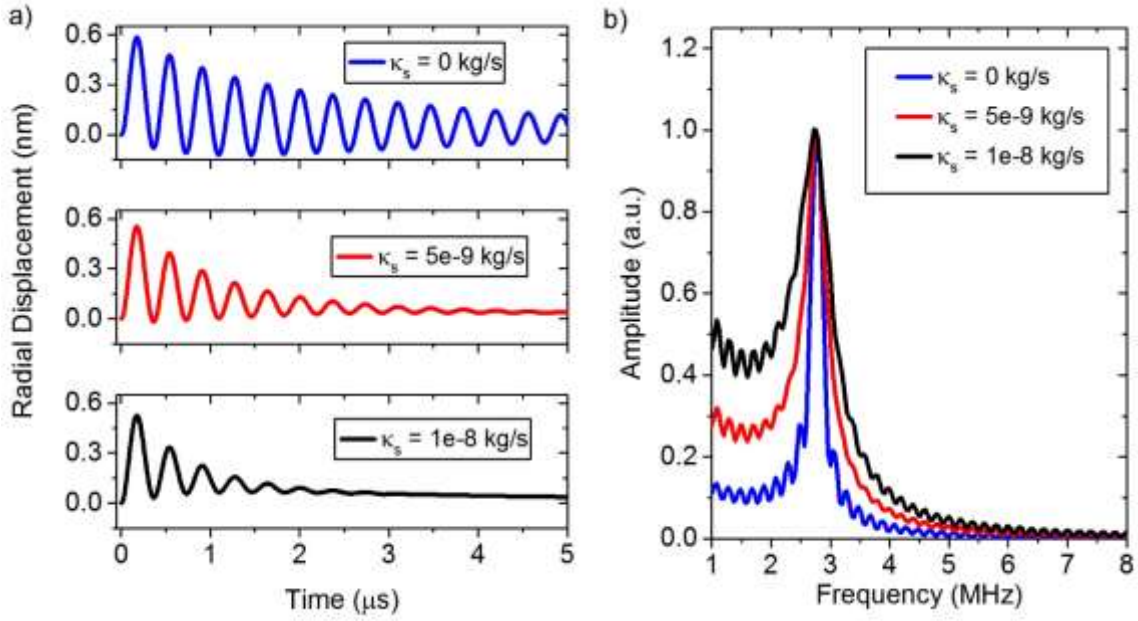

Figure 2.12 (a) The bubble wall radius of a 2.5 μm bubble is plotted as a function of time for varying shell viscosities (b) The corresponding frequency content of the time-domain response normalized to the resonance peak.

The Fourier transform of the time-domain response is shown in Fig. 2.12 (b). The resonance peak does not shift in frequency but broadens as shell viscosity is increased. The quality factor ($Q = f_0/\Delta f$) which is related to the damping ratio, $Q = 1/2\zeta$, is a measure of the stored energy over the dissipated energy. A resonator with a high Q factor will undergo more oscillations than a resonator with a lower Q factor. As shell viscosity is increased, the Q factor of the bubble is lowered. Considering an optically driven bubble as a photoacoustic contrast agent, the higher the Q factor the more acoustic power is radiated from bubble. Hence, an encapsulating shell that minimizes viscous losses would be ideal.

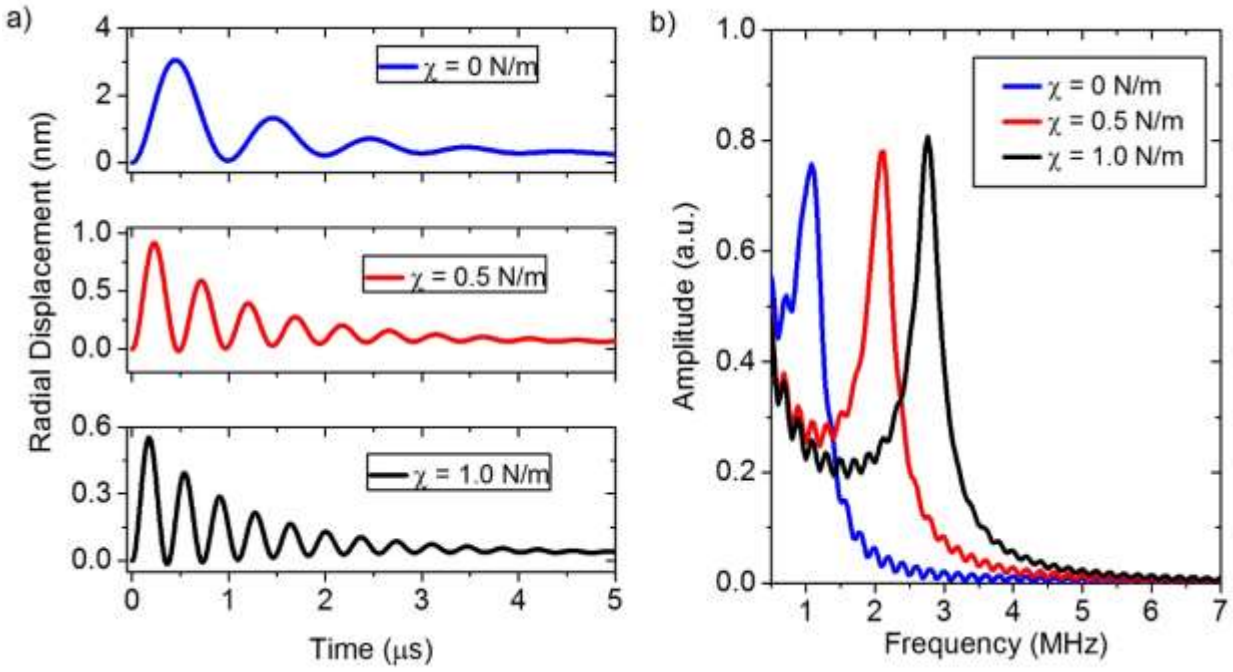

Figure 2.13 (a) The bubble wall radius of a 2.5 μm bubble is plotted as a function of time for varying shell elasticies. (b) The corresponding frequency content of the time-domain response.

The shell elasticity, χ, adds an additional restoring force causing the eigenfrequency to shift to higher values. The time-domain response of a bubble with a resting radius of 2.5 μm is shown in Fig. 2.13 (a). Here, the shell viscosity is held constant at $5x10^{-9}$ kg/s, and the shell elasticity of the bubble is increased from 0 to 1 N/m. As a result of the changing elasticity, the resonance frequency shifts. Fig. 2.13 (b) shows the Fourier transform of the time-domain responses. The resonance peak shifts from 1.08 MHz to 2.76 MHz as the shell elasticity is increased from 0 to 1.0 N/m, respectively. This is an important result, as populations of bubbles that all have exactly a 2.5 μm radius but exhibit variations in shell elasticity will produce a photoacoustic response over a wide frequency band. It would be beneficial to minimize the variations in shell elasticity such that photoacoustic emission is over a narrow bandwidth and destructive interference effects from multiple bubbles is minimized.

The amplitude of the radial oscillations decreases as the shell elasticity increases, as shown in Fig. 2.13 (a). The thermal drive, T_B, and the bubble diameter are held constant, and the only changing factor is the shell elasticity. This is a result of the increased resonance frequency, as predicted from Eqn. (2.47). Here, it is helpful to consider the response of a second order system to an impulse, which scales inversely with the resonant frequency. The added shell elasticity causes an increase in the restoring forces, which will minimize the overshoot in response to an impulse, causing the first oscillation to decrease in amplitude. This result indicates that bubbles with a low shell elasticity would offer improved signal-to-noise ratio due to the larger amplitude oscillations.

2.5. Model Improvements

This model provides estimates on the response of a nanoparticle-coated microbubble. However, the heating of the gas core was simplified to a uniform temperature distribution throughout the volume of the core. This simplification neglects the heat diffusion process in the gas core averaging out the temperature over space. Considering the thermal diffusion length for a 1 ns optical pulse in the decafluorobutane gas core is 42 nm, heat diffusion is expected to play a role.

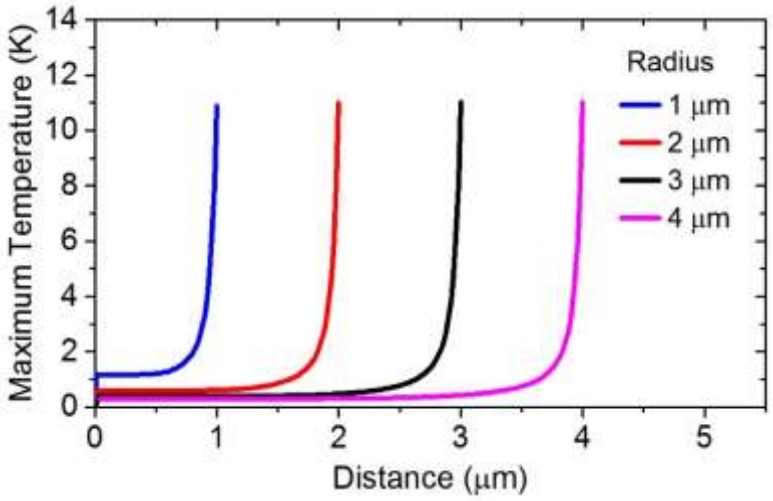

Figure 2.14 The maximum temperature within the gas core for varying bubble radii as a function of distance from the bubble center.

The maximum temperature within the gas core is plotted as a function of distance from the bubble center in Fig. 2.14. The optical pulse length was 1 ns and 1 mJ/cm^2. Here, the maximum temperature is observed to occur next to the heated shell and is similar for different sized bubbles. In addition, within 20 nm of the shell the temperature drops by 80%. To improve accuracy of the model the spatial dependence of the gas core heating, as evident from Fig. 2.14, would need to be accounted for.

2.6. Conclusions

To conclude, a model was developed for the photothermal drive of bubble oscillations. The classical heat diffusion equation was used to model pulsed laser heating of an individual nanoparticle, and then for a shelled bubble. The heat flux from the bubble wall was calculated and used to estimate a uniform temperature increase of the gas core. The uniform temperature increase of the gas core was coupled into a modified Rayleigh-Plesset equation to describe the bubble dynamics. The results from heating of individual nanoparticles indicate that larger nanoparticles may offer improved heating. In addition, different nanoparticle geometries, such as nanorods or nanoshells, may offer further improvements in optical absorption and heating.

The results indicate a microbubble coated with gold nanoparticles 5 nm in diameter can be driven to oscillate with a pulsed laser source. The amplitude of the oscillation is on the order of 1 nm for 1 mJ/cm^2 with frequencies in the low megahertz regime. In addition, the dynamic response of the bubble to pulsed laser illumination depends on bubble size and shell properties. The results indicate minimizing both the shell viscosity and elasticity would improve the photoacoustic emission from the bubble.

References

[1] Jain, P. K., Huang, X., El-Sayed, I. H., and El-Sayed, M. A., 2008, "Noble Metals on the Nanoscale: Optical and Photothermal Properties and Some Applications in Imaging, Sensing, Biology, and Medicine," Acc. Chem. Res., 41(12), pp. 1578–1586.

[2] Huang, X., Qian, W., El-Sayed, I. H., and El-Sayed, M. A., 2007, "The potential use of the enhanced nonlinear properties of gold nanospheres in photothermal cancer therapy," Lasers Surg. Med., 39(9), pp. 747–753.

[3] Tong, L., Wei, Q., Wei, A., and Cheng, J., 2009, "Gold Nanorods as Contrast Agents for Biological Imaging: Optical Properties, Surface Conjugation and Photothermal Effects†," Photochemistry and Photobiology, 85(1), pp. 21–32.

[4] Ju, H., Roy, R. A., and Murray, T. W., 2012, "Gold nanoparticle targeted photoacoustic cavitation for potential deep tissue imaging and therapy," Biomed Opt Express, 4(1), pp. 66–76.

[5] Lapotko, D., 2009, "Optical excitation and detection of vapor bubbles around plasmonic nanoparticles," Opt. Express, 17(4), pp. 2538–2556.

[6] Yang, X., Stein, E., Ashkenazi, S., and Wang, L., 2009, "Nanoparticles for photoacoustic imaging," Wiley Interdiscip. Rev.: Nanomed. Nanobiotechnol., 1(4), pp. 360–368.

[7] Zhang, Q., Iwakuma, N., Sharma, P., Moudgil, B. M., Wu, C., McNeill, J., Jiang, H., and Grobmyer, S. R., 2009, "Gold nanoparticles as a contrast agent for in vivo tumor imaging with photoacoustic tomography," Nanotechnology, 20(39), p. 395102.

[8] Agarwal, A., Huang, S. W., O'Donnell, M., Day, K. C., Day, M., Kotov, N., and Ashkenazi, S., 2007, "Targeted gold nanorod contrast agent for prostate cancer detection by photoacoustic imaging," Journal of Applied Physics, 102(6), pp. 064701–064701–4.

[9] Kerker, M., 1969, The scattering of light, and other electromagnetic radiation, Academic Press.

[10] Bohren, C. F., Clothiaux, E., and Huffman, D. R., 2010, Absorption and Scattering of Light by Small Particles, Wiley-VCH.

[11] Jain, P. K., Lee, K. S., El-Sayed, I. H., and El-Sayed, M. A., 2006, "Calculated Absorption and Scattering Properties of Gold Nanoparticles of Different Size, Shape, and Composition: Applications in Biological Imaging and Biomedicine," The Journal of Physical Chemistry B, 110(14), pp. 7238–7248.

[12] Richardson, H. H., Carlson, M. T., Tandler, P. J., Hernandez, P., and Govorov, A. O., 2009, "Experimental and Theoretical Studies of Light-to-Heat Conversion and Collective Heating Effects in Metal Nanoparticle Solutions," Nano Lett., 9(3), pp. 1139–1146.

[13] Schleichert, U., Langenberg, K. J., Arnold, W., and Fabbender, S., 1989, "A Quantitative Theory of Laser-Generated Ultrasound," Review of Progress in Quantitative Nondestructive Evaluation, D.O. Thompson, and D.E. Chimenti, eds., Springer US, pp. 489–496.

[14] Pustovalov, V. K., 2005, "Theoretical study of heating of spherical nanoparticle in media by short laser pulses," Chemical Physics, 308(1–2), pp. 103–108.

[15] Marmottant, P., Meer, S. van der, Emmer, M., Versluis, M., Jong, N. de, Hilgenfeldt, S., and Lohse, D., 2005, "A model for large amplitude oscillations of coated bubbles accounting for buckling and rupture," The Journal of the Acoustical Society of America, 118(6), pp. 3499–3505.

[16] Rayleigh, Lord, 1917, "VIII. On the pressure developed in a liquid during the collapse of a spherical cavity," Philosophical Magazine Series 6, 34(200), pp. 94–98.

[17] Leighton, T., 1994, The Acoustic Bubble, Academic Press.

[18] Plesset, M. S., and Prosperetti, A., 1977, "Bubble Dynamics and Cavitation," Annual Review of Fluid Mechanics, 9(1), pp. 145–185.

[19] Overvelde, M., Garbin, V., Sijl, J., Dollet, B., de Jong, N., Lohse, D., and Versluis, M., 2010, "Nonlinear Shell Behavior of Phospholipid-Coated Microbubbles," Ultrasound in Medicine & Biology, 36(12), pp. 2080–2092.

Chapter 3

Fabrication and characterization of plasmonic microbubbles

3.1. Introduction

This section will cover the fabrication and characterization of nanoparticle-templated microbubbles. The majority of the work presented in this section is from a paper published in Soft Matter titled *"Enhanced photoacoustic response with plasmonic nanoparticle-templated microbubbles"* [1]. A method to controllably template nanoparticles to the shell of a lipid encapsulated microbubble is presented. Physiochemical and photoacoustic characterization is performed on the nanoparticle-coated microbubbles. The plasmonic microbubbles are used to demonstrate dual mode contrast enhanced imaging.

3.2. Motivation

To optimize the molecular design of a nanoparticle-templated microbubble, an approach is desired that allows for robust control over microbubble size, nanoparticle placement, and nanoparticle loading density. Microbubble size can be controlled through microfluidics during generation or through differential centrifugation, a post processing technique [2,3]. In previous studies, nonplasmonic nanoparticles, such as polymer nanobeads, lipoplexes or liposomes, were loaded

onto microbubbles with controlled density by utilizing avidin-biotin coupling chemistry.[4–7] In these studies, the microbubble contained a lipid-anchored, poly(ethylene glycol)-terminal biotin, and avidin is used to conjugate the nanoparticle to the microbubble. The ratio of biotinylated lipopolymer to phospholipid molecules coating the microbubble was varied to control the nanoparticle surface density, up to the maximum limit allowed by geometric constraints of nanoparticle packing. These studies showed that avidin-biotin coupling is a very useful and straightforward conjugation scheme to control nanoparticle-to-microbubble stoichiometry. We propose to utilize this methodology to decorate microbubbles with plasmonic nanoparticles.

Here, a dual mode contrast agent, plasmonic gold nanoparticle-loaded microbubbles (referred to as plasmonic microbubbles), is presented that is capable of enhancing the photoacoustic response over that of free nanoparticles while retaining the microbubble's ability to effectively scatter ultrasound. We fabricated size-selected, biotin-functionalized microbubbles and loaded them with avidin-conjugated gold nanoparticles to generate plasmonic microbubbles. Nanoparticle surface coverage was controlled by modifying the ratio of biotinylated lipid self-assembling into the microbubble shell. We then characterized the physicochemical properties of the plasmonic microbubbles, and observed a marked enhancement in the photoacoustic response of the plasmonic microbubbles over that observed from free nanoparticle solutions. We performed dual mode ultrasound and photoacoustic imaging in a flow-through tissue phantom to demonstrate the potential of the approach in biomedical imaging applications.

3.3. Materials and Methods

3.3.1. Materials

The microbubbles were fabricated using 1,2-distearoyl-sn-glycero-3-phosphocholine (DSPC) purchased from NOF America (White Plains, NY, USA), 1,2-distearyol-sn-glycero-3-

phosphoethanolamine-N-[methoxy(polyethylene glycol)2000] (DSPE-PEG2000) purchased from Avanti Polar Lipids (Alabaster, AL, USA), and 1,2-distearoyl–sn–glycerol–3-phospho-ethanolamine-N[biotinyl (polyethylene glycol)-2000] (DSPE-PEG2000-B) purchased from Avanti Polar Lipids (Alabaster, AL, USA). The gas used to form the microbubbles was perfluorobutane (PFB) at 99 wt % purity obtained from FluoroMed (Round Rock, TX, USA). The avidin-tagged nanoparticles were purchased from Nanopartz (Loveland, CO, USA)

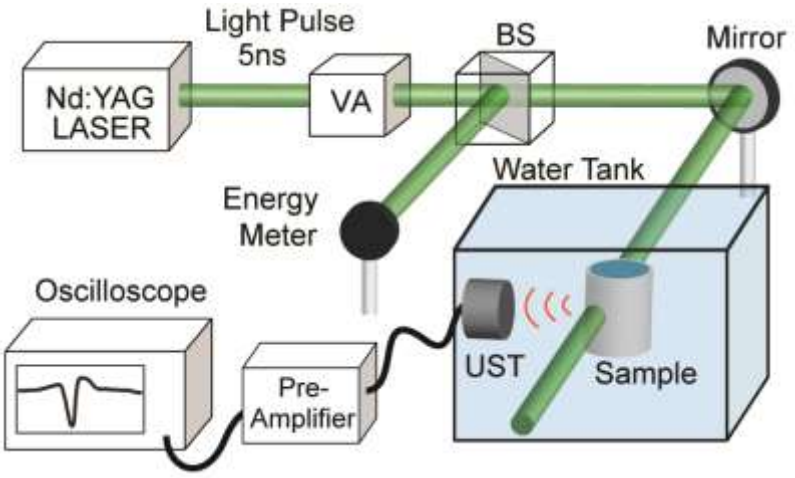

Figure 3.1 Diagram outlining the general experimental set-up for photoacoustic measurements. The following abbreviations are used- VA: variable attenuator, BS: beam splitter, and UST: ultrasound transducer.

3.3.2. Fabrication of plasmonic microbubbles

For the study, microbubbles coated with DSPC:DSPE-PEG2000:DSPE-PEG2000-B at molar ratios of 90:9:1, 90:9.25:0.75, 90:9.5:0.5, 90:9.75:0.25 and 90:9.9:0.1, were fabricated using probe sonication and size isolated to 2-8 microns using differential centrifugation.[2] Briefly, the lipid solutions were placed in a sonicator to fully disperse the lipid solution and heat it above the main phase transition temperature (~55^{o}C for DSPC). The sonicator tip was then raised to the liquid-gas interface and PFB gas was allowed to fill the head space. The solution was then sonicated at high power for 10s to generate lipid-encapsulated microbubbles with a PFB gas core. Size-isolation was

performed with a bucket-rotor centrifuge model 5804 Eppendorf (Westbury, NY, USA). First the polydisperse microbubble solution was centrifuged at 300 relative centrifuge force (RCF) for 5 minutes and the cake was collected. The polydisperse microbubbles were then size-selected through a three-step centrifuge process. First, microbubbles 4 microns and greater were collected by centrifugation at 90 RCF for 1 minute. The resulting cake was then re-suspended and centrifuged at 70 RCF for 1 minute. The infranatant was collected, removing 5 micron and greater microbubbles and centrifuged at 90 RCF concentrating the remaining size-isolated microbubbles. Size-selected, biotin-functionalized microbubbles were then combined with 5-7 nm, avidin-gold spheres at a 1:1 ratio of biotin: avidin, where one nanoparticle contains one avidin (as specified by the manufacturer), and mixed for 2 hours. After conjugation, the plasmonic microbubbles were dispersed in phosphate buffer saline and allowed to separate from unconjugated nanoparticles through gravitational flotation.

3.3.3. Photoacoustic measurements

The experimental setup for measuring the photoacoustic response from the plasmonic microbubbles is shown in Fig 4. The light source for all the photoacoustic experiments was a Q-switched and frequency doubled neodymium-doped yttrium aluminum garnet (Nd:YAG) laser Surelite I-20 (Santa Clara, CA, USA) operating at a wavelength of 532 nm with a laser pulse width of approximately 5 ns. The emitted photoacoustic signals were detected with a focused ultrasound transducer with a center frequency of 2.25 MHz and a focal length of 50.8 mm. The ultrasound transducer was placed perpendicular to the optical beam, with the transducer focal point at the center of the optical axis. The output of the transducer was sent to a 40 dB preamplifier before being recorded with an oscilloscope for further processing. Two methods were employed to hold the sample. In the first approach, the plasmonic microbubbles were placed in a plastic vial with

thin, acoustically and optically transparent polymer windows and the solution was continuously mixed using a magnetic stirrer. In the second technique, a flow through apparatus was constructed that allowed plasmonic microbubbles to be injected into a thin walled, optically transparent fluorinatedethyleneproplylene tube with a syringe pump, Kent Scientific Genie Plus (Torrington, Connecticut, USA). The flow was stopped to fix the plasmonic microbubbles in space such that the same plasmonic microbubbles could be interrogated over multiple laser shots. To measure the photoacoustic response, samples of plasmonic microbubbles were diluted to a concentration of 10^6 mL^{-1} while the controls of free nanoparticles matched the measured gold content of the plasmonic microbubbles.

3.3.4. Ultrasound and photoacoustic imaging

Ultrasound and photoacoustic imaging was performed on a 2% agarose gel flow through phantom. The agarose was purchased from Sigma-Aldrich (St. Louis, MO, USA). Ultrasound images were produced using a Siemens Sequoia Imaging System, Acuson Sequoia 512 from Siemens Healthcare (Malvern, Pennsylvania, USA) at 7MHz in cadence pulse sequencing mode and 8 MHz for B-mode images. The transducer was placed perpendicular to the axial direction of flow through the agarose gel phantom recording a circular cross section of the flow channel. The photoacoustic images were produced by illuminating agarose flow through phantom with the pulsed laser system. The diameter of the excitation beam was 2.75 mm (at the 1/e point). Acoustic waves emitted from the sample were detected using a 10MHz focused transducer aligned to the center of the channel. The gel phantom was scanned along the ultrasound transducer's focal plane such that the focus of the ultrasound transducer remained aligned to the center of the channel and an axial cross section was imaged with a step size of 0.2 mm in both directions. The maximum intensity of the detected photoacoustic signal was plotted to form an image. Samples of microbubbles and plasmonic

microbubbles were diluted to 10^6 mL^{-1} for both ultrasound and photoacoustic imaging. The concentration of nanoparticles used during ultrasound imaging matched that of plasmonic microbubbles. However, the free gold nanoparticles at this concentration did not register a detectable photoacoustic signal under these conditions. We therefore used 15-times the concentration of free gold nanoparticles for photoacoustic imaging.

3.4. Results and discussion

3.4.1. Physiochemical characterization

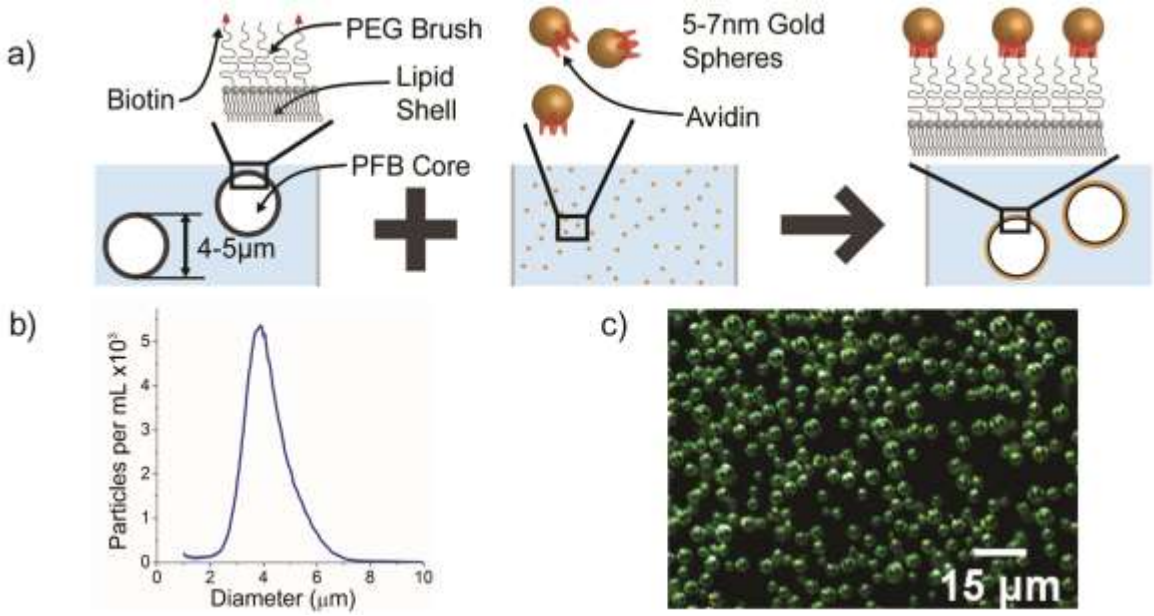

Figure 3.2 (a) Schematic illustrating the conjugation scheme allowing for stoichiometric control over nanoparticle templating on microbubbles. (b) A typical size distribution measured after conjugation of nanoparticles to size-selected microbubbles with a 0.25% biotin mole fraction. (c) Dark field microscopy image of plasmonic microbubbles with a 0.25% biotin mole fraction.

Nanoparticle conjugation to the microbubble surface was achieved through the specific binding of avidin to biotin. Fig. 3.2(a) outlines the microbubble templating process. Lipid encapsulated perfluorobutane microbubbles were synthesized and size selected to 4-5 μm diameter. The microbubble surfaces were functionalized with biotin, which binds to the avidin-tagged gold nanoparticles. The ligand-receptor pair was chosen as a straightforward approach to systematically

study the effects of loading density. The 5-nm gold nanoparticle was chosen as it only contained one avidin which helped prevent plasmonic microbubble aggregation during the conjugation process. Fig. 3.2(b) shows a typical size distribution of plasmonic microbubbles measured through electrical impedance sensing with a Beckman-Coulter Multisizer III. The median diameter was 3.9 μm, with 96.6% of the population between diameters of 2 μm and 8 μm. This correlated well with dark field microscopy, as shown in Fig. 3.2(c).

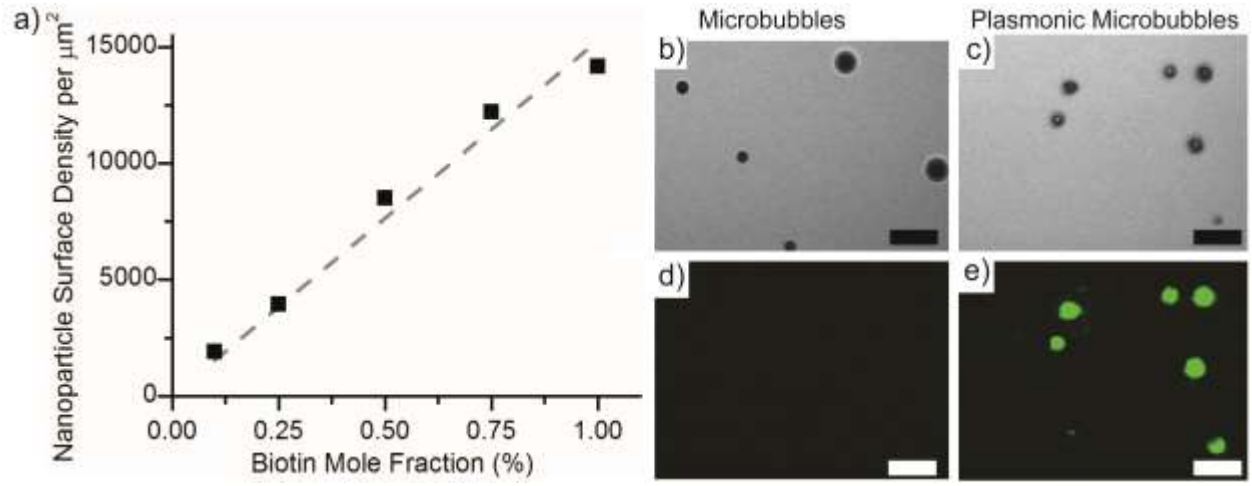

Figure 3.3 Verification of nanoparticle conjugation to microbubble shell. (a) ICP-MS results comparing nanoparticle surface density for varying biotinylated lipid mole fractions of plasmonic microbubbles. Microscopy image of (b) microbubbles and (c) plasmonic microbubbles with laser illumination at 810 nm. Multiphoton luminescence microscopy image of (d) microbubbles and (e) plasmonic microbubbles, scale bars are 15 microns.

Verification of gold nanoparticle binding to the microbubble shell was provided by inductively coupled plasma mass spectroscopy (ICP-MS) and multiphoton luminescent microscopy. Fig. 3.3(a) shows the results from ICP-MS for a series of biotinylated lipid mole fractions. The concentration (microbubbles per mL) and size distribution of the plasmonic microbubbles were measured with the Beckman Multisizer III. The total surface area per mL was calculated from the size distribution data. Given the lipid head group area of 0.4 nm^2, the total number of molecules per mL was estimated. Based on the stoichiometry of the shell, the number of biotinylated lipids

per mL could be estimated. The number of gold nanoparticles was estimated assuming a 1:1, biotin:nanoparticle, binding ratio.

$$C_{E,NP} = \frac{4\pi r_i^2}{A_{lipid}} C_i B_{mol\%} \tag{3.1}$$

Where $C_{E,NP}$ is the estimated concentration of nanoparticles per mL, r_i is the bubble radius and C_i is the bubble concentration per mL at index *i* radius, A_{lipid} is the lipid head group area, and $B_{mol\%}$ is the biotinylated lipid mole percent. The estimated gold nanoparticle concentration was compared to the measured gold nanoparticle concentration from ICP-MS to calculate the binding efficiency. The nanoparticle concentration is related to the gold concentration through a volume calculation based on the average diameter of the nanoparticles.

$$BE = \frac{C_{E,NP}}{C_{M,NP}} \tag{3.2}$$

Where *BE* is the binding efficiency, $C_{M,NP}$ is the measured nanoparticle concentration from ICP-MS. The total number of nanoparticles per square micron was determined using the binding efficiency and the stoichiometry of the shell.

$$NPs = \frac{B_{mol\%}}{A_{lipid}} BE \tag{3.3}$$

Where NP_s is the measured nanoparticle surface density and is plotted as the ordinate of Fig. 3.3(a). For a 3-μm diameter microbubble with 1 mol% biotin, in which 46.0 fg Au per μm^2 was measured, we estimated ~400,000 nanoparticles per microbubble. The measured gold content increased linearly with biotin content, as expected. From a purely geometric perspective, assuming a lipid head group area of 0.40 nm^2 for a compressed lipid monolayer with near-zero surface

tension, the ratio of biotin to avidin was approximately 60% for all mole fractions, even though we mixed in a 1:1 ratio of avidin-to-biotin. This is consistent with previous reports of avidin saturation occurring at ~50% (indicating a 1:2 avidin:biotin ratio) onto microbubbles containing 2 mol% biotin [8]. It has been suggested that avidin contains two opposing faces, with two biotin binding pockets per face [9]. In our system, one avidin face was occupied by the gold nanosphere, while the other face exposed two free binding pockets to the biotin moieties on the microbubble surface.

Confirmation of nanoparticle localization to the microbubble surface was provided through multiphoton luminescent microscopy and extinction spectroscopy. Gold nanoparticles have been shown to exhibit multiphoton luminescence when excited in the near infrared wavelength range [10,11]. In these experiments, a picosecond laser operating at 810 nm was used to illuminate samples of uncoated microbubbles and plasmonic microbubbles. The scattered light was collected and filtered as the sample was scanned through the field of view of the microscope. Images produced by collecting the scattered light at the excitation laser wavelength (810 nm) are shown in Fig. 3.3(b) for the uncoated microbubbles and Fig. 3.3(c) for the plasmonic microbubble, with several microbubbles clearly evident in both images. Figs. 3(d) and 3(e), on the other hand, show images of the same samples produced by filtering the collected light in the 450-550 nm wavelength range for microbubbles and plasmonic microbubbles, respectively. The uncoated microbubbles (Fig. 3.3(d)) did not produce a detectable nonlinear optical response. However, the plasmonic microbubble image (Fig. 3.3(e)) shows a strong nonlinear optical response which, through comparison with Fig. 3.3(b), is seen to be localized to the position of the microbubbles. We attribute this to a multiphoton luminescence produced at the dense population of nanoparticles at

the plasmonic microbubble surface, providing further evidence of nanoparticle conjugation onto the microbubble shell.

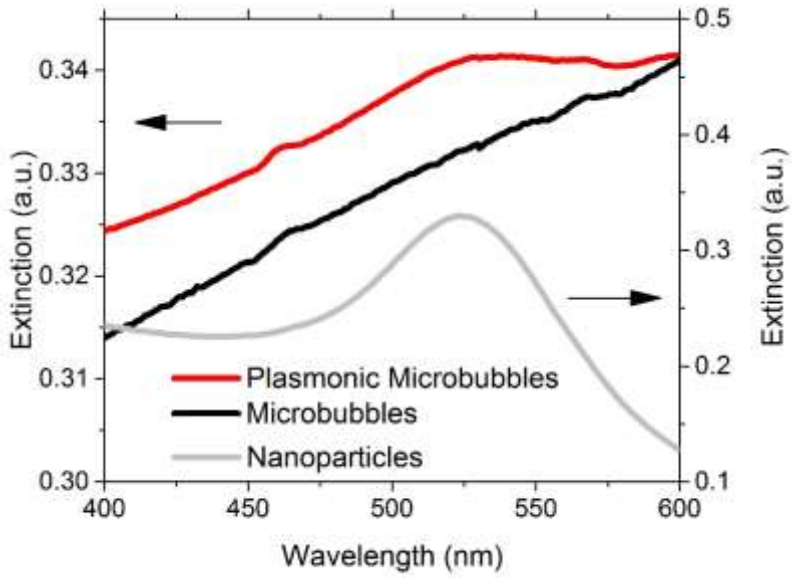

Figure 3.4 Optical extinction spectroscopy of plasmonic microbubbles with a 0.75% biotin mole fraction, microbubbles and free nanoparticles with the left vertical axis corresponding to plasmonic microbubbles and microbubbles and the right vertical axis corresponding to free nanoparticles.

The optical extinction spectrum was measured for the plasmonic microbubbles, microbubbles and free gold nanoparticles as shown in Fig. 3.4. For plasmonic microbubbles and microbubbles, due to their gas core, both optical scattering and absorption contribute to the measured extinction in contrast with the nanoparticles where optical absorption dominates the extinction measurement. The plasmonic microbubbles displayed a resonance at a similar wavelength to that of the surface plasmon resonance wavelength of the gold nanoparticles while no resonance was measured for unloaded microbubbles. The plasmonic microbubble resonance provides additional confirmation of nanoparticle loading and the optical absorption required for a photoacoustic response.

3.4.2. Photoacoustic characterization

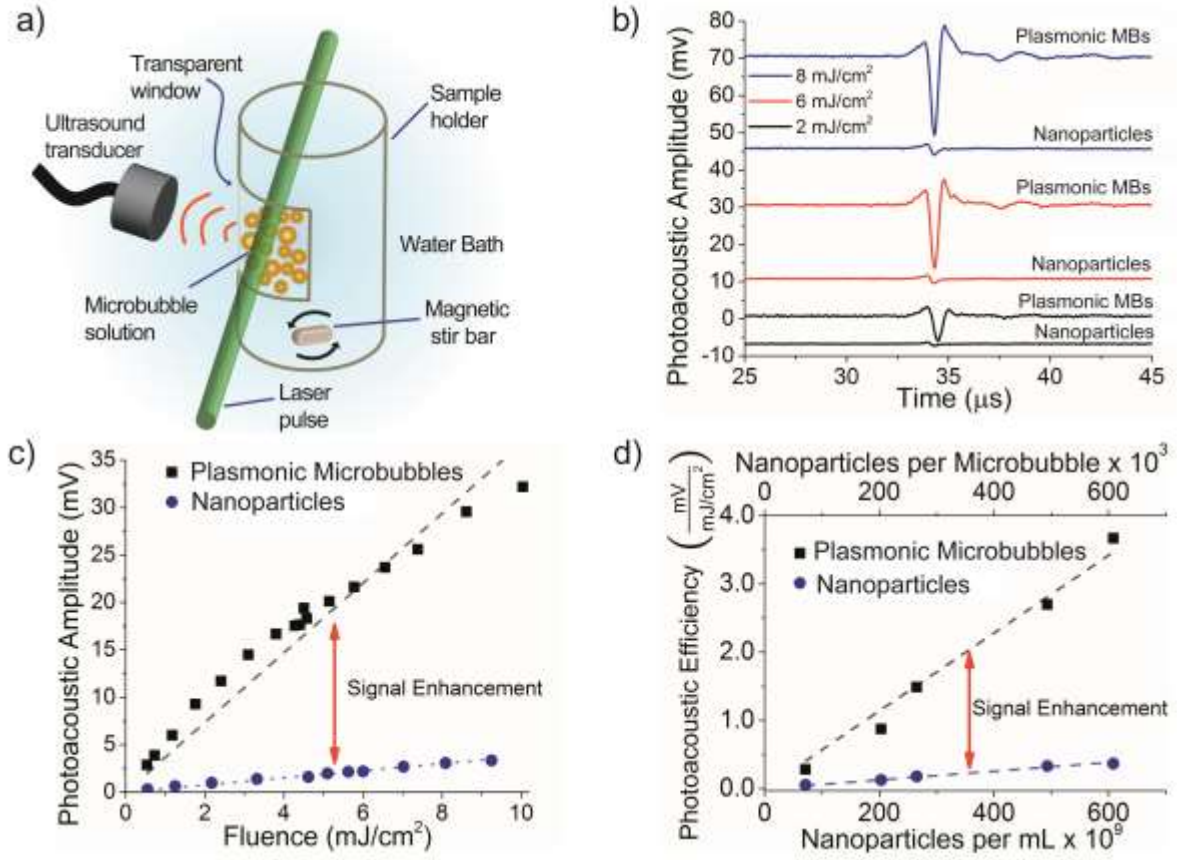

Figure 3.5 (a) A schematic outlining the experimental approach to measure the photoacoustic response. (b) Signal averaged (100 times) photoacoustic waveforms from plasmonic microbubbles at a 0.75% biotin mole fraction, and nanoparticles at the same concentration illuminated with laser fluences of 2, 6 and 8 mJ/cm^2. (c) Peak-to-peak amplitude of the photoacoustic waveforms recorded at varying fluences for plasmonic microbubbles and nanoparticles at the same gold concentration. (d) Photoacoustic efficiency for varying the number of nanoparticles per microbubble and nanoparticles at the same microbubble concentration for all five biotin mole fractions.

While the ultrasound response of plasmonic microbubbles has been studied in some detail,[12–14] the photoacoustic characteristics have received little attention. A sketch showing the experimental approach for measuring the photoacoustic response from the plasmonic microbubbles is shown in Fig. 3.5(a). To characterize the plasmonic microbubbles response at varying laser fluences, 25 mL of plasmonic microbubbles (at a concentration of 10^6 mL^{-1}) were held in a plastic vial and continually mixed while subjected to pulsed laser illumination. Fig. 3.5(b) shows typical

photoacoustic signals recorded for plasmonic microbubbles with a biotin mole fraction of 0.75% at laser fluences of 2, 6, and 8 mJ/cm^2. Also shown in Fig. 3.5(b) are the photoacoustic signals measured from free nanoparticles in solution, with the same nanoparticle concentration as the plasmonic microbubbles. The photoacoustic signals were delayed with respect to laser illumination by approximately 33.8μs, corresponding to the ultrasound propagation time from the focal position to the transducer. The amplitude, given in mV and proportional to pressure, is analogous to pixel intensity during photoacoustic imaging. The nanoparticle solution produced a bipolar ultrasonic signal, similar to that expected from a homogeneous cylindrical photoacoustic source [15]. However, the photoacoustic emission from the plasmonic microbubbles produced a more pronounced negative peak followed by several weak oscillations. In addition, the amplitude of the photoacoustic signal emitted by plasmonic microbubbles was consistently higher, by a factor of 8-9, than that of free nanoparticles.

The photoacoustic response observed for plasmonic microbubbles was found to depend on the nanoparticle loading density. Fig. 3.5(c) shows the peak-to-peak amplitudes of the photoacoustic signals as a function of fluence over the 0.5–10 mJ/cm^2 range, with the dotted line showing a linear fit to the data. The free nanoparticles showed a linear increase in signal amplitude with fluence. The plasmonic microbubbles showed some deviations from linearity, with a larger increase in photoacoustic amplitude at lower fluences. The slope of the linear fits in Fig. 3.8(c) provided a measure of the photoacoustic efficiency, giving the photoacoustic signal amplitude achievable for a given laser fluence. Fig. 3.5(d) shows the photoacoustic efficiency for all five biotin mole fractions of plasmonic microbubbles and the corresponding free nanoparticle solutions at the same gold content. In both cases, the efficiency was found to be proportional to the overall nanoparticle

concentration. However, the efficiency was 8.9-fold higher for plasmonic microbubbles than free nanoparticles.

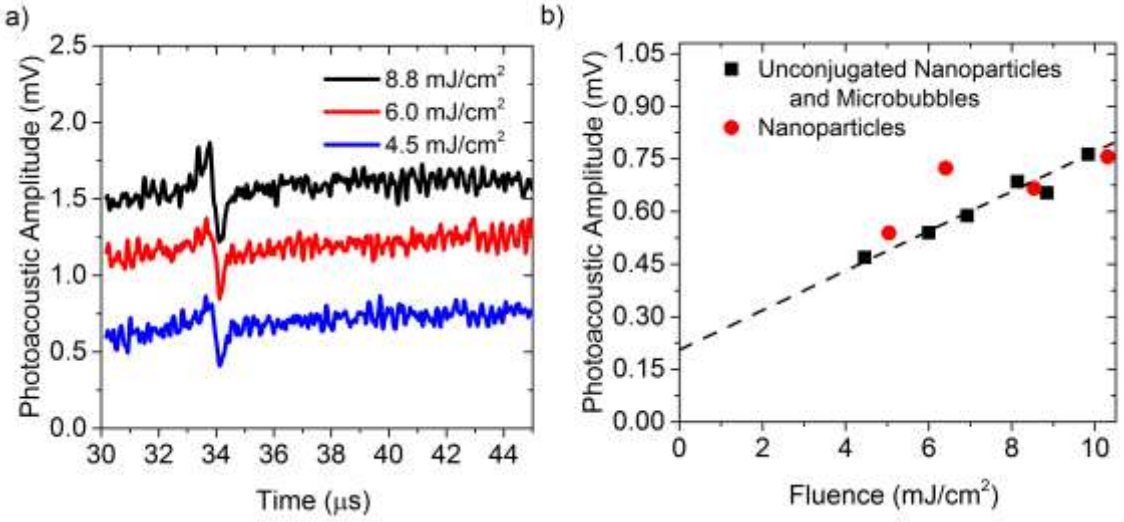

Figure 3.6 (a) Photoacoustic signals from unconjugated microbubbles mixed with nanoparticles. (b) Peak-to-peak amplitude from nanoparticles and unconjugated microbubbles mixed with nanoparticles.

To confirm the enhancement was due to attaching nanoparticles to the microbubble shell and not just the presence of the microbubble, experiments with unconjugated mixtures were performed. Fig. 3.6(a) shows the averaged photoacoustic signals recorded for the unconjugated nanoparticles and microbubble mixture for fluences at 4.5, 6.0 and 8.8 mJ/cm^2. The lower signal-to-noise is apparent when compared to Fig. 3.5(b). The measured signal is bipolar and similar to that of the free nanoparticles. Fig. 3.6(b) shows the peak-to-peak amplitudes of the photoacoustic signals as a function of fluence over a 5-10 mJ/cm^2 range. The dashed line is a linear fit to the peak-to-peak amplitude of unconjugated nanoparticles and microbubbles. The nonzero intercept arises from noise in the system, and indicates a noise level of ~0.19 mV. The photoacoustic amplitudes emitted from the free nanoparticles and the nanoparticles mixed with microbubbles both increased with fluence. The observed amplitudes from both cases were similar, indicating that the addition of

microbubbles in low concentration had little effect, with the photoacoustic response dictated primarily by the nanoparticles. The photoacoustic response of microbubbles alone yielded signals below the noise level due to the lack of optical absorption.

The marked increase in signal amplitude and efficiency suggests a potential coupling between the gold nanoparticles and the compressible microbubble gas core. With a spatially confined photoacoustic source (small with respect to the acoustic wavelength) the photoacoustic response is expected to be dictated by the total nanoparticle concentration, leading to similar responses for the plasmonic microbubbles and nanoparticles. However, the fact that the nanoparticles are arrayed around a compressible gas core may provide enhancement through photoacoustic or photothermal coupling to the microbubble itself (i.e., that microbubble oscillation is driven by optical illumination). As the microbubble resonance (1.5-3 MHz for microbubble diameters of 4-6 μm)[16] falls within the frequency band of the detection transducer (2.25-MHz center frequency), optically driven microbubbles would act to focus the broadband excitation frequencies to those within the detection band, providing an enhancement [17]. Further evidence of coupling is provided from the fact that the shape of the photoacoustic response of the plasmonic microbubbles differs from that of the free nanoparticles.

To explore the signal enhancement provided by the microbubble gas core further, the photoacoustic response was measured before and after ultrasonic destruction of the plasmonic microbubbles. Here, the plasmonic microbubbles with a biotin mole fraction of 1.0% were flowed through a narrow (inner diameter equal to 1.93 mm and outer diameter of 2.33 mm) polymer tube. The flow was stopped once the plasmonic microbubbles populated the tube, and the fixed plasmonic microbubbles were subjected to pulsed laser illumination. Fig. 3.7 (top) shows the photoacoustic signal observed using this geometry. The plasmonic microbubbles in the tube were

then destroyed using a 1.1 MHz, high-intensity ultrasound transducer operating at a peak negative focal pressure of 2.65 MPa [18,19]. The transducer focal point was scanned over the entire illuminated region of the tube to ensure plasmonic microbubble destruction. Fig. 3.7 (bottom) shows the photoacoustic response from the same region of the tube after this procedure. A strong reduction in the amplitude of the photoacoustic signal was observed with plasmonic microbubble destruction. The nanoparticle concentration in the illuminated region was likely unaffected by the high intensity ultrasound irradiation. However, the spatial distribution of nanoparticles, particularly with respect to the gas core, was altered leading to the observed signal reduction. This result demonstrated an ability to "trigger" a particular photoacoustic response through ultrasound exposure of the plasmonic microbubbles, a process that could potentially be used for theranostic applications. Furthermore, we hypothesize that ultrasound could potentially be used to release the nanoparticles from the microbubble shell, potentially allowing for a selective dose of nanoparticles to be delivered to a particular region of tissue.

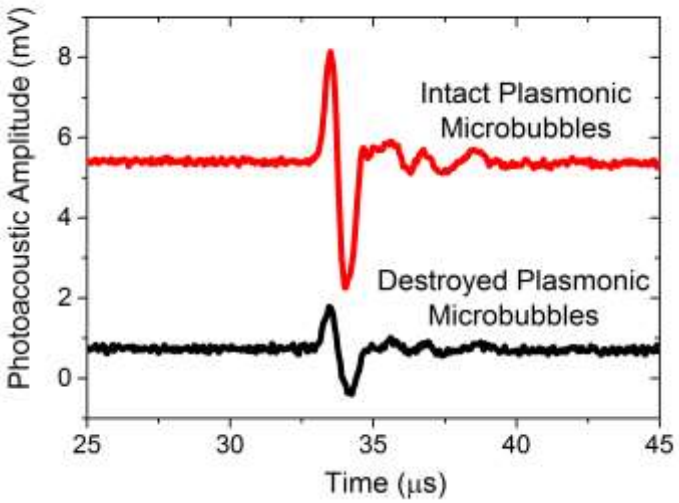

Figure 3.7 Signal averaged photoacoustic signals from fixed plasmonic microbubbles excited at 10mJ/cm^2 before (1000 averages with plasmonic microbubbles) and after (2000 averages with destroyed plasmonic microbubbles) the application of high intensity ultrasound.

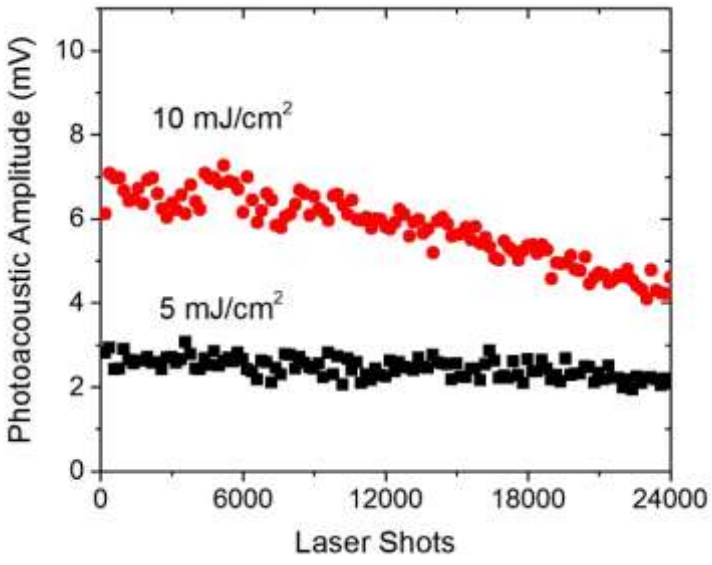

Figure 3.8 Photoacoustic amplitude of fixed plasmonic microbubbles illuminated at two different fluences as a function of laser shots while laser pulsing occurred at a rate of 20Hz. Data points represent peak-to-peak amplitude of a photoacoustic waveform signal averaged 50 times and were collected every 10 seconds.

The photoacoustic enhancement was observed to be sustained over long durations of laser excitation. Here, stability of the plasmonic microbubbles to exposure from multiple laser pulses was evaluated, using the same polymer tube to fix the plasmonic microbubbles in space. Plasmonic microbubbles with a biotin mole fraction of 1.0% were subjected to multiple laser pulses at fluences 5 mJ/cm^2 and 10 mJ/cm^2. The results are shown in Fig. 3.8, where each data point indicates the average peak-to-peak amplitude of the photoacoustic signal measured over 50 laser pulses, with a 10 second interval between data points. The photoacoustic signals observed at a laser fluence of 5 mJ/cm^2 are remarkably stable, showing only a slight reduction after as many as 24,000 laser shots. The total time of this measurement was approximately 20 minutes, and it is unclear if the slight reduction in photoacoustic amplitude was triggered by the laser exposure or microbubble dissolution, a process which is somewhat variable in different microbubble

environments.[20,21] The photoacoustic signal observed at a laser fluence of 10 mJ/cm^2, on the other hand, showed a monotonic reduction in amplitude starting at an exposure of about 6000 shots and continuing until the end of the experiment. Comparison of the data collected at the two laser fluences suggested that the laser is having an effect on the plasmonic microbubbles at the higher fluence, albeit not a significant influence until a very large number of laser shots.

3.4.3. Contrast enhanced dual mode imaging

The results indicate that plasmonic microbubbles may have the potential to be a powerful multi-modal contrast agent, producing signal enhancement in both ultrasound and photoacoustic imaging. To demonstrate this, we performed *in vitro* multimodal imaging in an agarose tissue phantom. The phantom was fabricated with a 2.3-mm diameter cylindrical channel to accommodate the flow of microbubbles and nanoparticles. We first compared the photoacoustic response of nanoparticles, microbubbles and plasmonic microbubbles under a laser fluence of 10 mJ/cm^2. Here the concentration of nanoparticles was 1.33×10^{13} mL^{-1}, approximately 15 times the nanoparticle concentration in the plasmonic microbubbles. The concentration of microbubbles was 10^6 mL^{-1}, identical to the concentration of plasmonic microbubbles. The photoacoustic image was formed by aligning the detection transducer to the center of the channel and scanning the sample about the transducer focal plane, creating an image of the axial cross section of the channel. At each spatial position, the maximum intensity of the photoacoustic signal was captured and plotted to produce an image. All signals were digitally filtered to suppress frequencies below 2 MHz and above 8 MHz. The results of this experiment are shown in Figs. 3.9(a)-(c). The nanoparticle solution alone produced a weak photoacoustic response localized to the region of the tube, shown by the arrows in the image (Fig. 3.9(a)). Microbubbles alone did not produce a detectable photoacoustic response, as expected, due to the lack of optical absorption (Fig. 3.9(b)). The

plasmonic microbubbles produced the largest photoacoustic response, and the border of the channel is clearly observed (Fig. 3.9(c)). The mean pixel intensity for the plasmonic microbubbles was a factor of 4.7 greater than that observed from the free nanoparticle solution. Considering the fact that the nanoparticle concentration was greater in the free nanoparticle solution than the plasmonic microbubble solution, the signal enhancement normalized to nanoparticle concentration was approximately 70.5 for the maximum intensity projection, or 8.4-fold enhancement of the photoacoustic amplitude.

Similar experiments were performed to assess the ultrasound response of nanoparticles, microbubbles and plasmonic microbubbles in the same flow-through phantom. Here the ultrasound transducer array was aligned perpendicular to the flow channel to image the circular cross section. The results for B-Mode ultrasound imaging for nanoparticles, microbubbles and plasmonic microbubbles are shown in Figs. 3.9(d)-(f), respectively. The free nanoparticle solution was not seen in the ultrasound image due to the lack of echogenicity of the nanoparticles. The microbubble and plasmonic microbubble images were similar, with the overall pixel intensity varying by less than 13% between the two images. The gold loading on the microbubbles was found to have little effect on the echogenicity of the microbubbles, indicating that they can be used effectively as ultrasound contrast agents. We also looked at the nonlinear ultrasound response of the different solutions using cadence pulse sequencing. The results, shown in Figs. 3.9(g)-(i), are nearly identical to those observed for B-mode ultrasound imaging. Here the difference in pixel intensity between the images for microbubbles and plasmonic microbubbles was less than 10%, indicating a minimal effect of nanoparticle loading on the microbubble nonlinear ultrasound response.

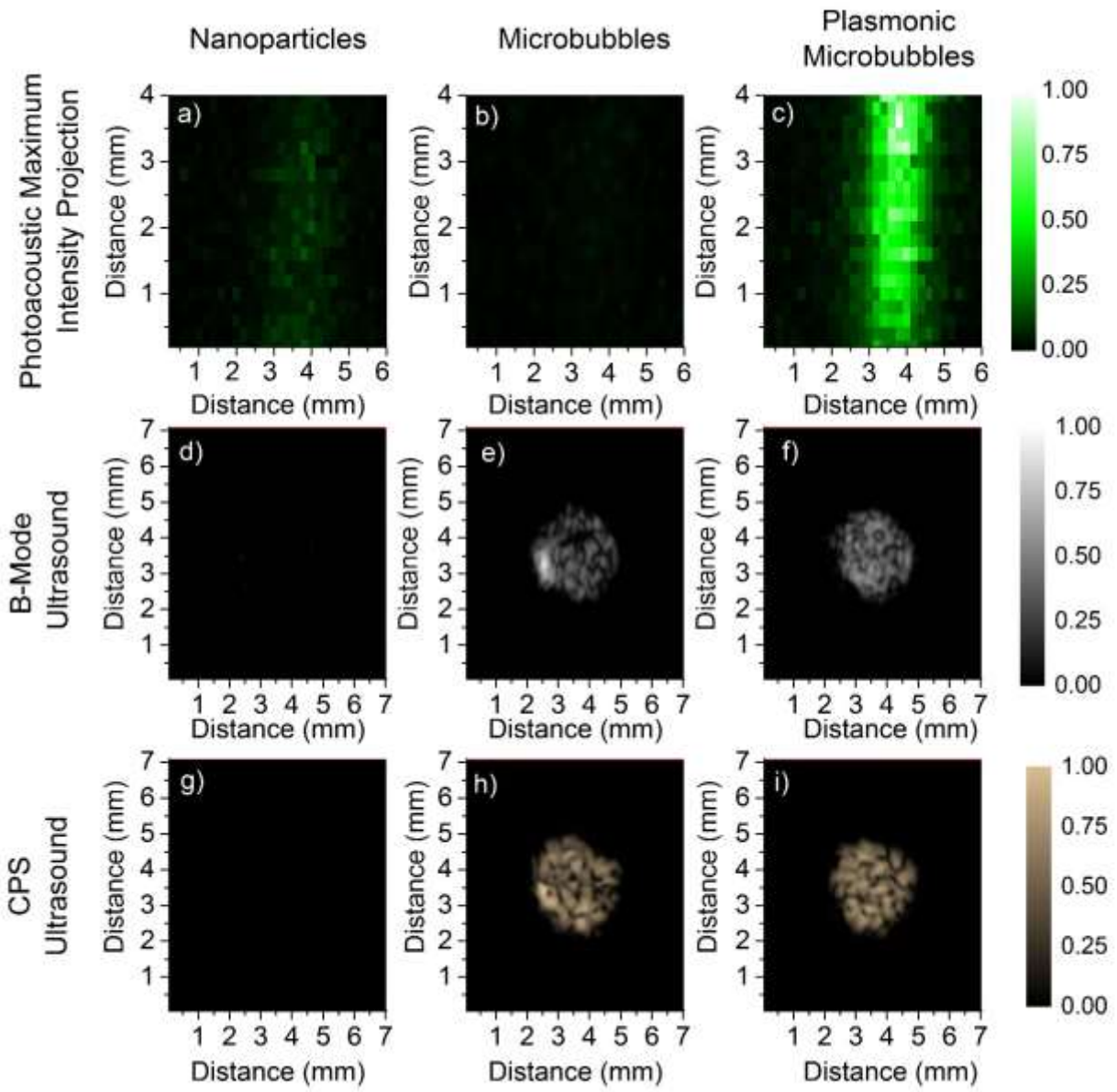

Figure 3.9 (a-c) Photoacoustic maximum intensity projection image, from a custom photoacoustic imaging setup (d-f) B-mode ultrasound and (g-i) CPS ultrasound images acquired from a Siemens Sequoia Imaging System. Images of gold nanoparticles, microbubbles and plasmonic microbubbles were recorded for all modalities.

3.5. Conclusions

In conclusion, a facile methodology for the templating of plasmoinc gold nanoparticles onto lipid-coated microbubbles was demonstrated. Results from ICP-MS and photoluminescent microscopy verified the presence of gold on the microbubble surface. The photoacoustic response from plasmonic microbubbles was found to be significantly stronger than that observed from free nanoparticle solutions with the same nanoparticle concentration. This effect is hypothesized to be associated with the high nanoparticle concentration surrounding the compressible gas core, potentially allowing for laser energy to drive the resonant oscillations of the microbubble. This was supported by an experiment employing high-intensity ultrasound to induce microbubble destruction, in which we observed a sharp decrease in the photoacoustic response. Dual mode ultrasound and photoacoustic imaging of the contrast agent was demonstrated in an agarose flow-through tissue phantom. The plasmonic microbubbles retained the strong linear and nonlinear ultrasound response characteristic of microbubbles, while adding an exceptionally strong photoacoustic response. The latter effect may allow for contrast enhanced photoacoustic imaging at greater depths or at lower nanoparticle concentrations, potentially reducing toxicity [22]. While only 5-nm gold nanospheres were studied here, it is expected that larger nanoparticles with different geometries and larger optical absorption cross sections and plasmon peaks in the near-infrared wavelengths could be attached to the microbubble shell to optimize the plasmonic microbubble for bioimaging. In addition, the proposed methodology may also be used to produce an agent for ultrasound-guided photothermal therapy or photoacoustic-guided focused-ultrasound mediated drug delivery, where nanoparticle surface density can be varied to achieve the desired response.

References

[1] Dove, J. D., Murray, T. W., and Borden, M. A., 2013, "Enhanced photoacoustic response with plasmonic nanoparticle-templated microbubbles," Soft Matter, 9(32), pp. 7743–7750.

[2] Feshitan, J. A., Chen, C. C., Kwan, J. J., and Borden, M. A., 2009, "Microbubble size isolation by differential centrifugation," Journal of Colloid and Interface Science, 329(2), pp. 316–324.

[3] Stride, E., and Edirisinghe, M., 2008, "Novel microbubble preparation technologies," Soft Matter, 4(12), pp. 2350–2359.

[4] Kheirolomoom, A., Dayton, P. A., Lum, A. F. H., Little, E., Paoli, E. E., Zheng, H., and Ferrara, K. W., 2007, "Acoustically-active microbubbles conjugated to liposomes: Characterization of a proposed drug delivery vehicle," Journal of Controlled Release, 118(3), pp. 275–284.

[5] Lentacker, I., De Smedt, S. C., Demeester, J., Van Marck, V., Bracke, M., and Sanders, N. N., 2007, "Lipoplex-Loaded Microbubbles for Gene Delivery: A Trojan Horse Controlled by Ultrasound," Advanced Functional Materials, 17(12), pp. 1910–1916.

[6] Lentacker, I., Wang, N., Vandenbroucke, R. E., Demeester, J., De Smedt, S. C., and Sanders, N. N., 2009, "Ultrasound Exposure of Lipoplex Loaded Microbubbles Facilitates Direct Cytoplasmic Entry of the Lipoplexes," Mol. Pharmaceutics, 6(2), pp. 457–467.

[7] Lum, A. F. H., Borden, M. A., Dayton, P. A., Kruse, D. E., Simon, S. I., and Ferrara, K. W., 2006, "Ultrasound radiation force enables targeted deposition of model drug carriers loaded on microbubbles," Journal of Controlled Release, 111(1–2), pp. 128–134.

[8] Chen, C. C., and Borden, M. A., 2010, "Ligand Conjugation to Bimodal Poly(ethylene glycol) Brush Layers on Microbubbles," Langmuir, 26(16), pp. 13183–13194.

[9] Leckband, D. E., Schmitt, F.-J., Israelachvili, J. N., and Knoll, W., 1994, "Direct Force Measurements of Specific and Nonspecific Protein Interactions," Biochemistry, 33(15), pp. 4611–4624.

[10] Farrer, R. A., Butterfield, F. L., Chen, V. W., and Fourkas, J. T., 2005, "Highly Efficient Multiphoton-Absorption-Induced Luminescence from Gold Nanoparticles," Nano Lett., 5(6), pp. 1139–1142.

[11] Yelin, D., Oron, D., Thiberge, S., Moses, E., and Silberberg, Y., 2003, "Multiphoton plasmon-resonance microscopy," Opt. Express, 11(12), pp. 1385–1391.

[12] Park, J. I., Jagadeesan, D., Williams, R., Oakden, W., Chung, S., Stanisz, G. J., and Kumacheva, E., 2010, "Microbubbles Loaded with Nanoparticles: A Route to Multiple Imaging Modalities," ACS Nano, 4(11), pp. 6579–6586.

[13] Stride, E., Pancholi, K., Edirisinghe, M. ., and Samarasinghe, S., 2008, "Increasing the nonlinear character of microbubble oscillations at low acoustic pressures," Journal of The Royal Society Interface, 5(24), pp. 807 –811.

[14] Seo, M., Gorelikov, I., Williams, R., and Matsuura, N., 2010, "Microfluidic Assembly of Monodisperse, Nanoparticle-Incorporated Perfluorocarbon Microbubbles for Medical Imaging and Therapy," Langmuir, 26(17), pp. 13855–13860.

[15] Tam, A. C., 1986, "Applications of photoacoustic sensing techniques," Rev. Mod. Phys., 58(2), p. 381.

[16] Van der Meer, S. M., Dollet, B., Voormolen, M. M., Chin, C. T., Bouakaz, A., de Jong, N., Versluis, M., and Lohse, D., 2007, "Microbubble spectroscopy of ultrasound contrast agents," J. Acoust. Soc. Am., 121(1), p. 648.

[17] Sassaroli, E., Li, K. C. P., and O'Neill, B. E., 2009, "Linear behavior of a preformed microbubble containing light absorbing nanoparticles: Insight from a mathematical model," J. Acoust. Soc. Am., 126(5), p. 2802.

[18] Chen, W.-S., Matula, T. J., Brayman, A. A., and Crum, L. A., 2003, "A comparison of the fragmentation thresholds and inertial cavitation doses of different ultrasound contrast agents," The Journal of the Acoustical Society of America, 113(1), pp. 643–651.

[19] Hernot, S., and Klibanov, A. L., 2008, "Microbubbles in ultrasound-triggered drug and gene delivery," Advanced Drug Delivery Reviews, 60(10), pp. 1153–1166.

[20] Katiyar, A., Sarkar, K., and Jain, P., 2009, "Effects of encapsulation elasticity on the stability of an encapsulated microbubble," Journal of Colloid and Interface Science, (336), pp. 519–525.

[21] Kwan, J. J., and Borden, M. A., 2010, "Microbubble Dissolution in a Multigas Environment," Langmuir, 26(9), pp. 6542–6548.

[22] Lewinski, N., Colvin, V., and Drezek, R., 2008, "Cytotoxicity of Nanoparticles," Small, 4(1), pp. 26–49.

Chapter 4

Optically Activated Microbubbles

4.1. Introduction

This section will cover the excitation and detection of resonant microbubble oscillations. The majority of this work was published in Optics Letters title "*Optically induced resonance of nanoparticle-loaded microbubbles"*[1]. Optically absorbing nanoparticles were attached to the shell of a lipid-encapsulated microbubble to facilitate photothermal activation. An experimental setup that tracks the bubble wall radius as a function of time using light scattering is discussed. The microbubble response from a nanosecond laser pulse was measured. The eigenfrequency, vibrational amplitude and the quality factor were determined and compared to theory.

4.2. Motivation

The previous chapter demonstrated that gold nanoparticle-loaded microbubbles are efficient photoacoustic contrast agents, and that templating the nanoparticles around microbubbles leads to

a synergistic photoacoustic response from microbubble suspensions that exceeds that from free suspensions of nanoparticles with an equivalent concentration [2]. The enhancement was hypothesized to originate from optically driven resonance of the microbubble population, producing a strong acoustic response in the low MHz frequency range associated with the resonance frequency distribution within the microbubble population. In this section, direct evidence is provided that gold nanoparticle-templated microbubbles can indeed be driven into resonance using a pulsed laser excitation source. The bubble wall radius as a function of time was tracked for individual microbubbles using light scattering. Considering the resonant nature of the microbubble acoustic emission and the frequency-dependent nature of ultrasound absorption in tissue, controlled emission of acoustic energy in the low MHz frequency range is particularly well suited for photoacoustic imaging. In addition, the ability to probe single microbubble oscillations with high fidelity and sensitivity using optical excitation and detection offers a new, and potentially powerful, technique for the study of basic microbubble physics. Here the optical characterization of gold nanoparticale-coated microbubbles through the measurement of the resonance characteristics and radial displacement is demonstrated.

4.3. Materials and Methods

4.3.1. Experimental Setup

The experimental setup is shown in Fig. 4.1. Microbubbles were excited with a pulsed microchip laser with a wavelength of 532 nm, a pulse width of 1.5 ns and a repetition rate of 3.0 kHz. The laser pulses were sent through a variable attenuator and illuminated the sample through a long working distance microscope objective with a numerical aperture of 0.4. The spot size of the beam at the focal plane of the objective was 30 μm (1/e Gaussian diameter) and the variable attenuator

was adjusted such that the fluence was 4.5 mJ/cm^2. A continuous wave laser operating at a wavelength of 488 nm was sent to the sample through the same objective and used to probe the microbubble displacement. The optical power was 2.4 Mw and sent to the sample through the same objective and used to probe the microbubble displacement. The diameters of both the generation and detection beams incident on the objective were controlled to achieve Gaussian spatial profiles with 1/e radii at the objective focal plane of 15 μm and 10 μm, respectively. The light from the probe beam was collected using a lens (focal length = 20 mm) and sent through a 488-nm bandpass filter to a broadband photodetector. The output from the photodetector was then sent to a 40-dB preamplifier and recorded on a digital oscilloscope. A third optical port on the microscope housed a CCD camera and was used to locate, position and size microbubbles within the field of view of the microscope.

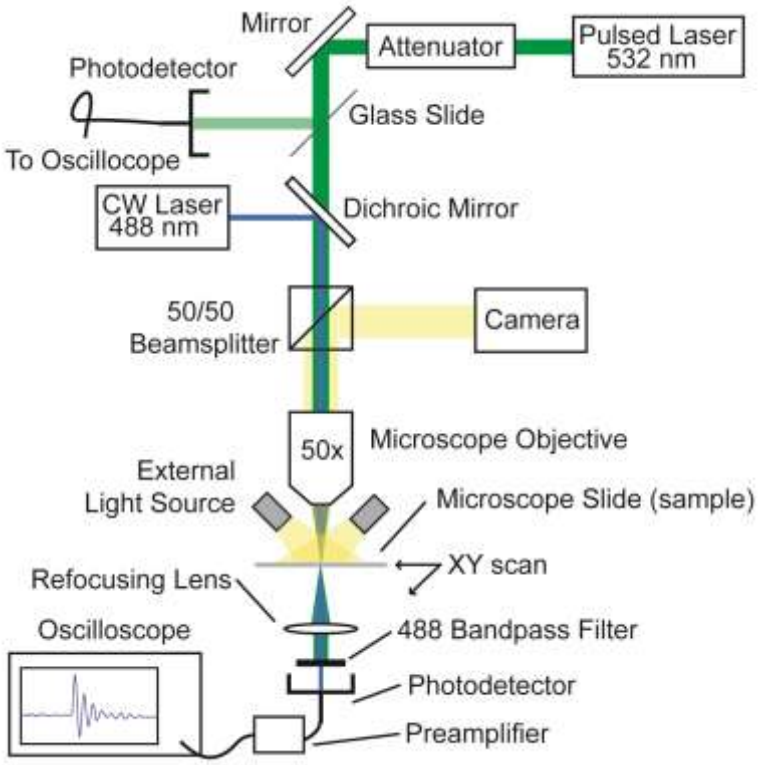

Figure 4.1 Experimental setup used to excite and detect the gold-coated microbubble oscillations

4.3.2. Nanoparticle-coated microbubble fabrication

The procedure for synthesizing gold nanoparticle-coated microbubbles was thoroughly described in Chapter 2. In brief, nanoparticle templating was achieved through specific binding of 5-nm avidin-tagged gold nanospheres to biotin-functionalized lipid-encapsulated microbubbles. The microbubble shell was composed of phospholipid derivatives (90% phosphatidylcholine *PC* and 10% phosphatidylethanolamine *PE* functionalized with polyethylene glycol, of which 10% of the *PE* contained a biotin at the terminus of the polyethylene glycol). The phospholipids were mixed together and heated above the *PC* main phase transition temperature of ~55˚C. The headspace of the precursor solution was filled with perfluorobutane (PFB) gas, and the liquid-gas interface was mechanically agitated with a probe sonicator to produce micron-scale bubbles. The microbubbles were then mixed with avidin-tagged nanoparticles, at a 1:1 ratio of biotin:avidin, where one nanoparticle contained one avidin. The total nanoparticle loading was estimated to be 15,000 nanoparticles per square micron with an absorption peak appearing at 530 nm, near the plasmon resonance wavelength of the gold nanoparticles. The gold nanoparticle-templated microbubbles were then separated from unconjugated nanoparticles through gravitational flotation. For the experimental measurements, the microbubbles were suspended in a 0.01M phosphate-buffered saline solution and injected between a microscope slide and cover slip.

4.4. Results and Discussion

4.4.1. Microbubble detection

The detection of microbubble oscillation was done using forward light scattering. The relationship between the scattered light signal and the microbubble radial displacement was found using a calibration procedure. A microbubble was identified within the field of view of the microscope as shown in Fig. 4.2 (a). Because dark field illumination was used, the scattered light from the gas-

liquid interface causes an increase in pixel intensity. The individual line scans from the dark field image were analyzed to determine the microbubble radius and position. Fig. 4.2 (b) shows the line scan corresponding to a y-position of 2.2 μm (the dotted line in Fig. 4.2 (a)). The half maximum position was located for first rising edge and the second declining edge, as shown as the stars in Fig. 4.2 (b). Repeating this process over the entire bubble resulted in several x-y coordinates that were used to determine the bubble size and location.

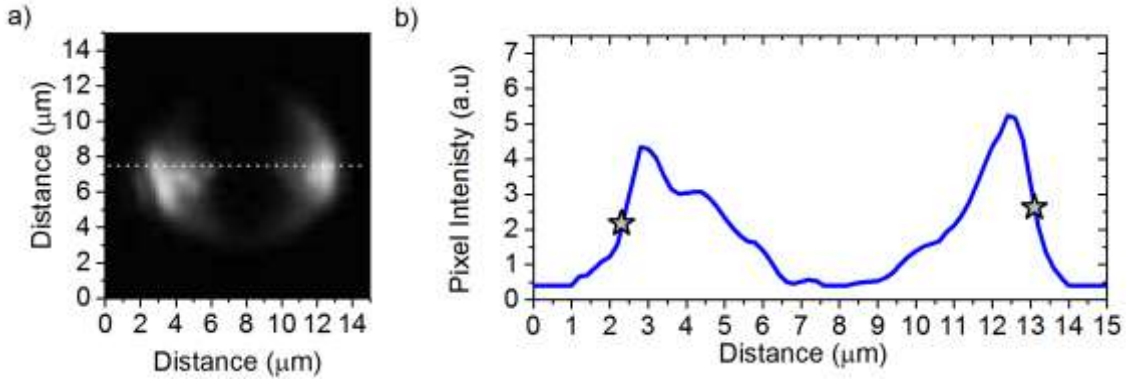

Figure 4.2 (a) Dark field micrograph of a nanoparticle coated microbubble. (b) Line scan corresponding to the dotted line in dark field micrograph. The stars represent the half-maximum points that were recorded for microbubble sizing and location.

A computer controlled positioning stage was then used to move the microbubble to the center of the probe beam, and the reduction in optical power (measured with and without the microbubble) associated with scattering was recorded. The microbubble size was determined from the optical image as discussed above. This process was repeated over a large population of microbubbles in the 1-6 μm size range resulting in the scatter plot shown in Fig. 4.2(a). A second order polynomial was then fit to these data, shown as a dashed line in the plot. For small displacements, the sensitivity of detection for a bubble of resting radius R can be found by evaluating the derivative of the curve fit ($\partial P/\partial R$) at the resting radius, where P is the optical

power. The resulting calibration curve is shown in Fig. 4.2(b), where the absolute sensitivity is seen to increase linearly with microbubble size.

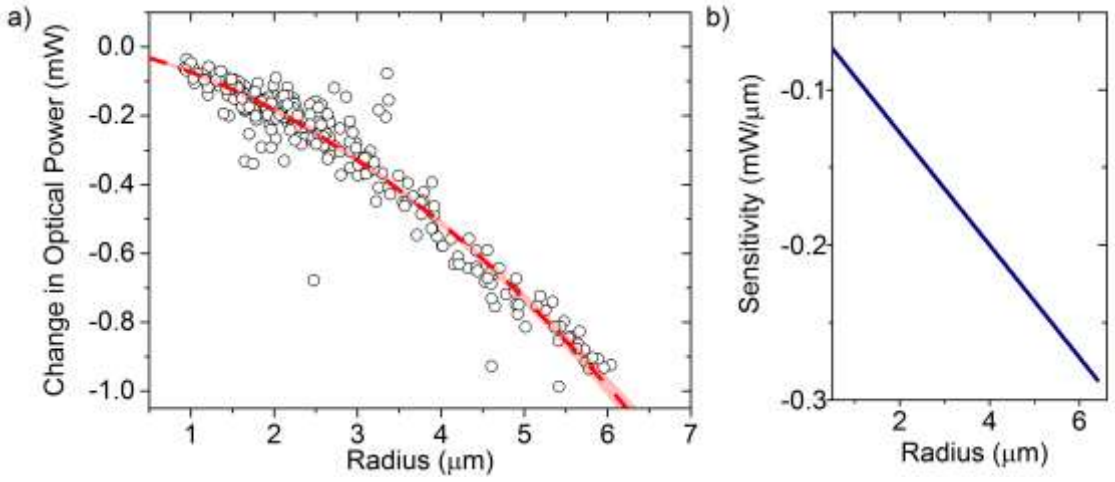

Figure 4.3 (a) Calibration curve used to convert the measured optical power at the photodetector to microbubble radius. The shaded area corresponds to a 95% confidence interval. (b) The static sensitivity as a function of microbubble radius.

The ability to accurately detect of small amplitude bubbles oscillations depends on the error associated with the calibration curve, bubble radius measurements, shot noise from the laser and thermal noise in the electronics. The amplitude of the detected microbubble vibration can be described through Eqn. (4.1) shown below:

$$S = M(R_0)P_m \tag{4.1}$$

Here S is the amplitude of the detected vibration, $M(R_0)$, is the inverse of the sensitivity shown in the inset of Fig 4.3 and is used to convert the fluctuations of optical power, P_M, to radius. Here, $M(R_0)$ depends on the initial resting radius, R_0, of the bubble. The calibration curve was a second order polynomial as shown below.

$$P(R) = AR_0^2 + BR_0 \tag{4.2}$$

Here A and B are fitting parameters. To determine $M(R_0)$, the derivate of the fitted calibration curve is evaluated at the bubble resting radius, R_0.

$$\frac{1}{M} = \frac{\partial P}{\partial R} = 2AR_0 + B$$

(4.3)

The uncertainty associated with detecting the small amplitude oscillations, S, can be evaluated through propagation of error. The uncertainty in the conversion parameter, U_M, is given by the expression below.

$$U_m = \sqrt{\left(\frac{dM}{dA}U_A\right)^2 + \left(\frac{dM}{dB}U_B\right)^2 + \left(\frac{dM}{dR}U_R\right)^2} \tag{4.4}$$

Here, U_A and U_B are the uncertainty in the fitting parameters A and B in Eqn. (4.3), and are determined by the standard error from the fit. The uncertainty in the measured can be expressed as:

$$U_S = \sqrt{\left(\frac{dS}{dM}U_{P_m}\right)^2 + \left(\frac{dS}{dP_m}U_M\right)^2} \tag{4.5}$$

Here, U_{pm} is the root-mean-square of the noise from the photodetector and is a combination of the shot-noise from the laser and the thermal noise from the electronics. The uncertainty in the measurement of the microbubble radius is equal to one pixel on the CCD camera which was 0.2 μm. The measurement uncertainty, Eqn. 4.5, is plotted in Fig. 4.4. Based on the calibration fit and measurement uncertainties was found to range from 9% of the measured amplitude for a bubble of radius 1μm to 5% for a bubble of radius 6 μm.

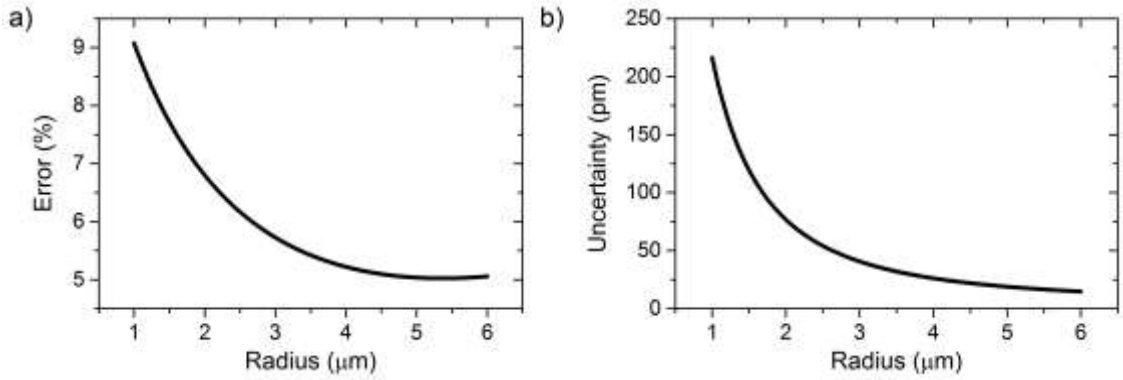

Figure 4.4 The uncertainty associated with the detection of the maximum amplitude vibration of optically stimulated microbubble represented as (a) percent of maximum displacement and (b) displacement.

4.4.2. Microbubble transient response to pulsed laser illumination

Experimental measurements of transient, laser-induced microbubble oscillations were performed in a manner similar to that described above, in that microbubbles were located, moved to the center of the probe beam and sized based on the optical image. The microbubbles were then illuminated using the pulsed laser source, and the probe response was recorded and converted to displacement. The results of these experiments for three microbubbles of radius R = 1.8 μm, 2.3 μm, and 5.6 μm are shown in Fig. 4.5, where the optical images used to determine the microbubble radii are also provided. Note that the signals are artificially offset for ease of viewing. The signals were averaged 130,000 times (at a repetition rate of 200 Hz, limited by the oscilloscope) reducing the *RMS* noise-equivalent displacement level to 35 pm and 14 pm for 1.8 μm and 5.6 μm microbubbles, respectively. The stimulation of microbubble oscillation using a pulsed laser source is clearly demonstrated, and the oscillation frequency increases with decreasing bubble size as expected. The mechanism through which the excitation takes place is believed to be photothermal, where light absorbed at the nanoparticle templated surface is converted to heat, resulting in rapid expansion of the gas core. Experiments on microbubbles without nanoparticles did not produce a

measurable response. In addition, experiments on microbubbles at an excitation wavelength of 1064 nm did not produce a measurable response. The smallest bubble (R = 1.8 μm) had the largest radial excursion of approximately 3 nm or 0.17% of the resting radius. The ability to excite and detect picometer-scale bubble oscillations with excellent temporal resolution (limited by the photodetector bandwidth) is a key benefit of the optical approach taken here.

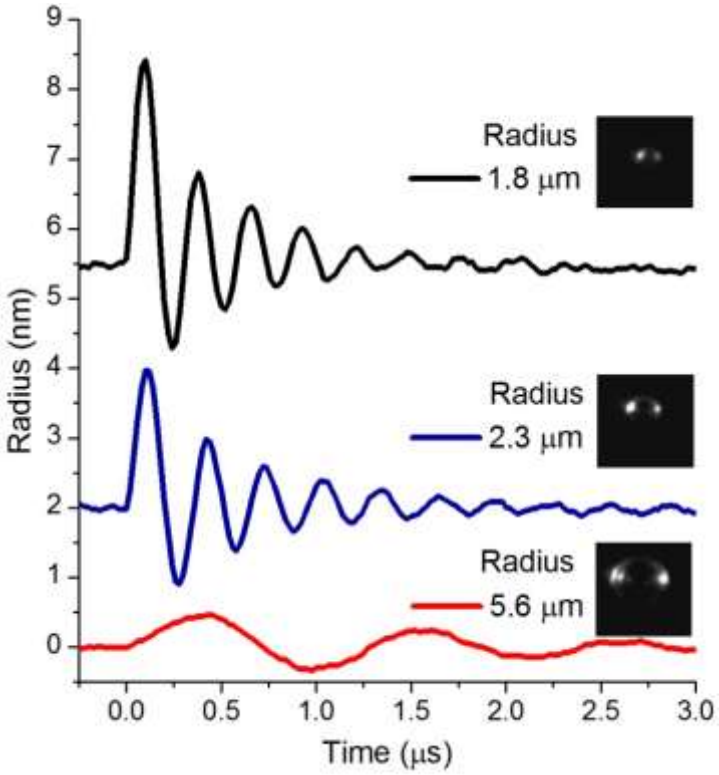

Figure 4.5 The time domain responses of gold-coated microbubbles to pulsed laser excitation for different microbubble sizes. The dark field images of the microbubbles are shown above the measured responses.

The mechanism through which the excitation takes place is believed to be photothermal, where light absorbed at the nanoparticle templated surface is converted to heat, resulting in rapid expansion of the gas core. This was covered in detail in Chapter 2, where the combined effect of all of the nanoparticles on the bubble surface led to significant heating of both the liquid and gas core. Interestingly, the calculated temperature rise in the gas core was on the order of ~5K (for a

4.5 mJ./cm^2 pulse) and the estimated radial displacement was in the 1-5 nm range, depending on bubble size. This estimate is in-line with the experimentally measured bubble response, as shown in Fig. 4.5. In addition, experiments on microbubbles without nanoparticles did not produce a measurable response, nor did experiments on nanoparticle loaded microbubbles at an excitation wavelength of 1064 nm, where the nanoparticles are inefficient absorbers. The smallest bubble (R = 1.8 μm) had the largest radial excursion of approximately 3 nm or 0.17% of the resting radius. The ability to excite and detect picometer-scale bubble oscillations with excellent temporal resolution (limited by the photodetector bandwidth) is a key benefit of the optical approach taken here.

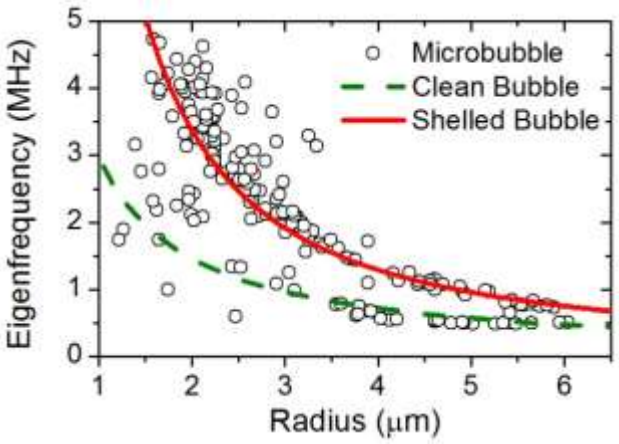

Figure 4.6 The measured eigenfrequencies for 194 gold coated microbubbles as a function of microbubble radius. The solid curve is the theoretical response for a shelled bubble with a shell elasticity of 0.73 N/m, while the dashed curve is the theoretical response for a "clean" or unshelled bubble.

The temporal responses from 194 individual gold-coated microbubbles distributed within the 1-6 μm radius range were measured and processed using the fast Fourier transform to find the resonance frequency. The damping ratio was found using the logarithmic decrement method, and used to calculate the eigenfrequency (undamped natural frequency), which is plotted in Fig. 4.6 as a function of microbubble size. The damping correction leads to an eigenfrequency that is slightly

higher (at most 3% in our case) than the measured resonance frequency. The solid line in Fig. 4.5 shows the fit to the (linearized) eigenfrequency of a shelled bubble given by Marmottant *et al.* Eqn. (4.6) [3,4]

$$f_0 = \frac{1}{2\pi}\sqrt{\frac{1}{\rho_L R^2}\left(3\gamma P_0 + \frac{2(3\gamma-1)\sigma_w}{R} + \frac{4\chi}{R}\right)} \tag{4.6}$$

where ρ_L is the density of the surrounding fluid, γ is the polytropic exponent for the gas core (assumed to be adiabatic and equal 1.07), P_0 is the ambient pressure, R is the resting radius of the gold-coated microbubbles, and σ_w is the surface tension of the gas-liquid interface and was assumed to be negligible. The shell elasticity term χ is used as a fitting parameter, with the constraint that $\chi>0$, and the best fit to the experimental data gives a shell elasticity of 0.74 N/m. A majority of the microbubbles have eigenfrequencies close to that predicted by Eqn. 1, and the scatter may be attributed in part to variations in the lipid concentration in the microbubble shells leading, in turn, to variations in shell elasticity[5]. Also shown in Fig. 4.6 is the curve for the resonance response of an undamped bubble without a stabilizing shell, referred to as a clean bubble, which was calculated using Eqn. 4 while setting the shell elasticity equal to zero $(\chi = 0)$. Interestingly, the resonant frequencies of a sub-population of microbubbles track those predicted for clean bubbles.

To further quantify the measured optical response from individual microbubbles, a histogram of the calculated shell elasticity is shown in Fig. 4.7. Here, the shell elasticity was directly calculated for each bubble by solving Eqn. 4 for χ. The majority of the microbubbles have a shell elasticity greater than 0.5 N/m and lower than 1.5 N/m. However, a small population of microbubbles displayed a low shell elasticity ranging from 0 to 0.25 N/m. We hypothesize that

this behavior may be attributed to some bubbles within the microbubble population having buckled shells. Lipid folds, indicative of a buckled shell, have been observed under fluorescent microscopy for similar microbubbles [6].

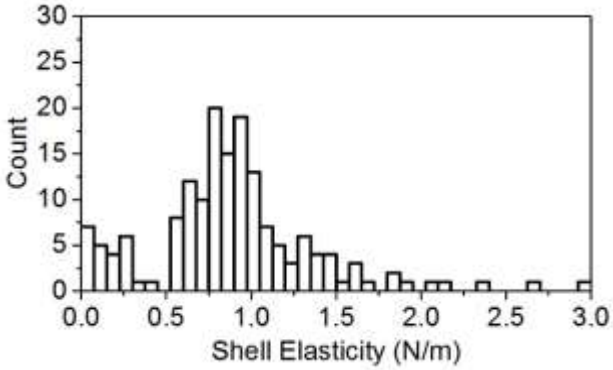

Figure 4.7 Histogram of the calculated shell elasticity.

The maximum radial displacement of the microbubble wall was also determined as a function of microbubble size, and the results are shown in Fig. 4.8 with the abscissa given in terms of inverse initial radius. The microbubbles were binned according to radius in 0.4 μm increments from 1 to 6 μm and the mean displacement plotted.

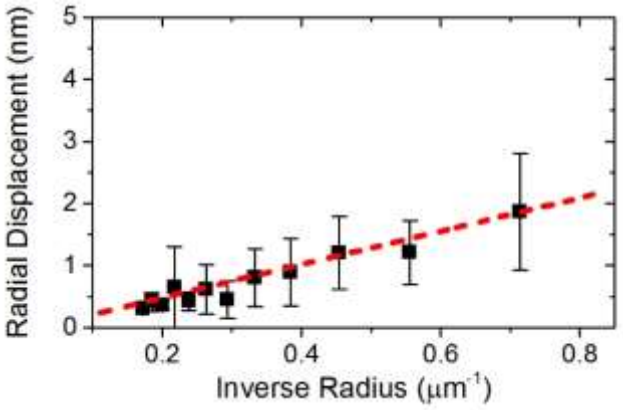

Figure 4.8 Maximum displacement as a function of inverse resting radius, the dashed line is the linear fit to the measured response.

A general trend is observed showing an increase in radial displacement as the microbubble size decreases. This trend was predicted with model when the heating function approached an impulse. Here, nanoparticles incorporated into the microbubble shell drive the oscillation through a photothermal process, then total absorbed energy from the templated nanoparticles scales with the surface area of the bubble, proportional to R^2. The volume of the gas core, on the other hand, which is heated to drive the photothermal oscillations, scales as R^3. In addition, when heat is deposited into the core before any of the bubbles complete an oscillation we can expect the radial displacement to be inversely proportional to the radius, which correlates with the general trend observed experimentally.

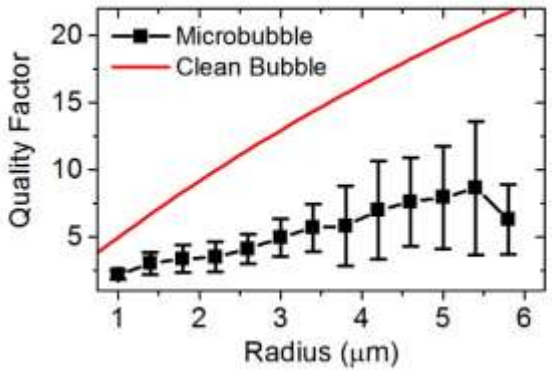

Figure 4.9 Quality factor as a function of resting radius, the solid curve is the predicted values for a clean bubble

The quality factor, Q = $f_0/\Delta f$, was determined as a function of microbubble size and is plotted in Fig 4.9. Here, the microbubbles were binned according to radius in 0.4 μm increments from 1 to 6 μm and the mean quality factor plotted. For a clean bubble only two sources of damping were assumed ($\zeta_{clean} = \zeta_{rad} + \zeta_{vis}$) the radiation of sound and viscous losses in the surrounding liquid (thermal damping in the gas core was assumed negligible) [3,7].

$$\zeta_{vis} = \frac{\mu}{\pi R^2 \rho_L f_0} \tag{4.7}$$

$$\zeta_{rad} = \frac{\pi f_0 R}{c} \tag{4.8}$$

Where μ is the viscosity and c is the speed of sound in the surrounding fluid. The quality factor is related to the damping ratio through the following expression:

$$Q = \frac{1}{2\zeta_{tot}} \tag{4.9}$$

Assuming the viscosity of water is 8.9×10^{-4} Pa*s and the speed of sound in water is 1500 m/s, the quality factor for a clean bubble was calculated and plotted as the solid line in Fig. 4.8. There is a large difference in the measured quality factor and that predicted by Eqn. 4.9. Following a previously described approach, the damping contribution from the shell can be expressed as [3,7]:

$$\zeta_{shell} = \frac{\kappa_s}{\pi R^3 \rho_L f_0} \tag{4.8}$$

Where κ_s is the viscosity of the shell. Assuming the difference between the predicted quality factor for a clean bubble and that measured is due to viscous losses from the encapsulating shell, the shell viscosity can be calculated. Using Eqn. 4.8 and the difference from the measured quality factor and the predicted quality factor for a clean bubble, the shell viscosity can be determined.

The calculated shell viscosity was found to range from 5.7×10^{-9} to 1.9×10^{-8} kg/s as shown in Fig. 4.10. Previous experiments on lipid shelled microbubbles reported the shell viscosity to range from 8×10^{-9} to 1×10^{-7} kg/s [3] and 8×10^{-9} to 4×10^{-8} kg/s [7]. Interestingly, Fig. 4.10 (a) shows the shell viscosity to increase as microbubble radius increases. However, the maximum radial

displacement and frequency also change with bubble radius. Therefore, the dilatational rate offers greater insight to the shell viscosity. The dilatational rate can be expressed as:

$$\frac{\dot{R}}{R} \approx \frac{\omega_0 \Delta R}{R} = \frac{2\pi f_0 \Delta R}{R} \tag{4.9}$$

Where ΔR is the maximum radial displacement, which is plotted in Fig. 4.8. The smallest bubble had the maximum radial displacement and the highest eigenfrequency which results in the maximum dilatational rate. This causes the shell viscosity to decrease with increasing dilatational rate, as shown in Fig. 4.10 (b). This type of rheological thinning behavior has been observed for lipid shelled microbubbles [4] and similar lipid monolayers [8].

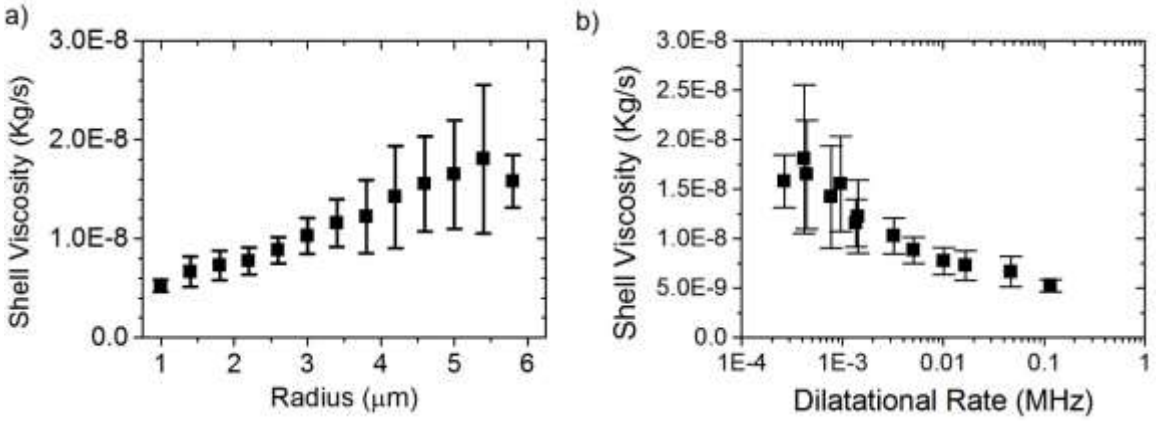

Figure 4.10 Calculated shell viscosity as a function of the (a) bubble radius and (b) dilatational rate of the oscillations.

Thin-film viscosity is known to be non-Newtonian and depend on the shear rate [9]. Here there are two important time scales to consider, the interaction time (τ_m) and the relaxation time (τ_0) of the molecules. The viscous losses are maximized when τ_m and τ_0 are equal or where the Deborah Number is one. The Deborah Number (De) is ratio of the τ_0 to τ_m $\left(\mathrm{De} = \tau_0/\tau_m\right)$ and useful to understand the shear thinning behavior observed in Fig. 4.10 (b). A lipid monolayer, for

example, will behave more solid-like or liquid-like if τ_m is faster or slower than τ_0 (i.e. De >1), respectively. In the liquid phase, lipids may slide past other each relatively slowly allowing for acyl chains to interdigitate and viscous losses will be high. For faster shear rates the lipids may slip past each other where the acyl chains do not interdigitate and viscous losses will be low. For lipids, the relaxation time has been measured to be around 80 ms [10]. From Fig. 4.10 (b), τ_m (or dilatational rates) range from 0.1 MHz to 0.1 kHz which gives Deborah Numbers or 8000 and 8, respectively. Hence, for the higher Deborah Numbers the lipid experience high shear rates and are able to slip past each other. As the dilatational rate decreases the Deborah Number approaches one and the viscosity increases as the acyl chains may interdigitate.

4.5. Conclusions

In the experimental measurements, the microbubbles probed with the optical beams are injected between a glass slide and cover slip and come to rest at the bottom surface of the top cover slip due to the buoyant force. It is well established that the presence of a boundary can change both the amplitude and resonance frequency of microbubble oscillations with respect to a free bubble. The decrease in resonance frequency associated with the presence of the top boundary is expected to be on the order of 20% [23-25]. The additional mass provided by the nanoparticle shell, when compared to the radiation mass of the bubble, was less than 2% and not considered in the analysis. Finally, we note that the microbubbles are exceptionally stable under pulsed laser illumination at a laser fluence of 4.5 mJ/cm^2, with no change in the resting radius observed even after hundreds of thousands of shots. Other effects, such as rapid bubble dissolution or a slow reduction in bubble radius, were observed when the fluence was increased above 10 mJ/cm^2. In addition, the nanoparticle-loaded microbubbles were found to remain optically active after several months of storage.

In conclusion, the optical stimulation of resonant mechanical oscillations of gold nanoparticle-templated microbubbles is demonstrated. A pulsed laser was used to drive the microbubbles through the photothermal effect, while the microbubble motion was tracked using light scattering. The high sensitivity, spatial resolution and fidelity of the optical interface makes it an attractive means for studying single microbubble dynamics and lipid mechanics, so long as light absorbing dyes or nanoparticles are incorporated into the shell. The optical properties of absorbing microbubbles can be tuned and optimized for photoacoustic conversion efficiency by, for example, controlling the nanoparticle type and distribution on the nanoparticle surface, and such optically active microbubbles may find application in multimodality photoacoustic and ultrasound imaging. In addition, the optical platform can potentially be used for the development of microbubble-based resonant mechanical sensors.

References

[1] Dove, J. D., Borden, M. A., and Murray, T. W., 2014, "Optically induced resonance of nanoparticle-loaded microbubbles," Opt. Lett., 39(13), pp. 3732–3735.

[2] Dove, J. D., Murray, T. W., and Borden, M. A., 2013, "Enhanced photoacoustic response with plasmonic nanoparticle-templated microbubbles," Soft Matter, 9(32), pp. 7743–7750.

[3] Van der Meer, S. M., Dollet, B., Voormolen, M. M., Chin, C. T., Bouakaz, A., de Jong, N., Versluis, M., and Lohse, D., 2007, "Microbubble spectroscopy of ultrasound contrast agents," J. Acoust. Soc. Am., 121(1), p. 648.

[4] Marmottant, P., Meer, S. van der, Emmer, M., Versluis, M., Jong, N. de, Hilgenfeldt, S., and Lohse, D., 2005, "A model for large amplitude oscillations of coated bubbles accounting for buckling and rupture," J. Acoust. Soc. Am., 118(6), pp. 3499–3505.

[5] Overvelde, M., Garbin, V., Sijl, J., Dollet, B., de Jong, N., Lohse, D., and Versluis, M., 2010, "Nonlinear Shell Behavior of Phospholipid-Coated Microbubbles," Ultrasound Med. Biol., 36(12), pp. 2080–2092.

[6] Chen, C. C., and Borden, M. A., 2010, "Ligand Conjugation to Bimodal Poly(ethylene glycol) Brush Layers on Microbubbles," Langmuir, 26(16), pp. 13183–13194.

[7] Helfield, B. L., and Goertz, D. E., 2013, "Nonlinear resonance behavior and linear shell estimates for Definity[trademark sign] and MicroMarker[trademark sign] assessed with acoustic microbubble spectroscopy," J. Acoust. Soc. Am., 133(2), pp. 1158–1168.

[8] Espinosa, G., López-Montero, I., Monroy, F., and Langevin, D., 2011, "Shear rheology of lipid monolayers and insights on membrane fluidity," Proc. Natl. Acad. Sci., 108(15), pp. 6008–6013.

[9] Israelachvili, J.N., 1992, Intermolecular and Surface Forces, Second Edition:With Applications to Colloidal and Biological Systems, Academic Press.

[10] Van Osdol, W. W., Johnson, M. L., Ye, Q., and Biltonen, R. L., 1991, "Relaxation dynamicsof the gel to liquid-crystalline transition of phosphatidylcholine bilayers. Effects of chainlength and vesicle size," Biophys. J., 59(4), pp. 775–785.

Chapter 5

Condensed Plasmonic Microbubble Vaporization

5.1. Introduction

This section will cover the condensation and optical vaporization of plasmonic microbubbles. The majority of this work is currently in review at Biomedical Optics Express with the title "*Engineering optically triggered droplets for photoacoustic imaging and therapy"*. I would like to acknowledge Paul Mountford for his efforts in fabrication and characterization of the droplet size and absorption spectrum. Optically absorbing nanoparticles were attached to the shell of a lipid-encapsulated microbubble. A high pressure was applied to the nanoparticle-coated microbubble to condense the gas core into a liquid. The effect of different perfluorocarbon cores on the threshold fluence for vaporization was examined. The core material was found to have a strong effect on optical vaporization threshold, with lower boiling point droplets undergoing vaporization at a lower fluence.

5.2. Motivation

In the previous chapters, the linear photoacoustic response of plasmonic microbubble was examined. The results show that there are several benefits that stem from coating microbubbles with nanoparticles such as, an enhanced photoacoustic response, photoacoustic activation of microbubble resonance and dual mode contrast, to name a few [1,2]. However, further improvements can be achieved by using the plasmonic microbubble as a starting point to create an optically active phase change agent. Phase change agents have a liquid with a low boiling point core and are capable of vaporization into a microbubble.

Phase change agents have been proposed as promising photoacoustic contrast agents [3–9]. In this case, perfluorocarbon (PFC) droplets are designed to absorb light at the wavelength of interest by incorporating a light absorbing species within the droplet or on the periphery. Optical absorption of a pulsed laser creates a local temperature rise within the droplet through the photothermal effect that leads to a phase transition; a process termed optical droplet vaporization (ODV). ODV based contrast agents have several advantages over photoacoustic contrast agents that rely solely on photothermal heating to produce acoustic waves in that a) the vaporization event produces an exceptionally strong photoacoustic response, exceeding that from the thermoelastic expansion and allowing for improved photoacoustic imaging contrast, b) the microbubbles created through ODV can provide ultrasound contrast in dual mode imaging scenarios and c) the light absorbing species incorporated into the droplets remain after vaporization and can be used to provide lasting enhanced photoacoustic contrast [3–5]. There has been progress towards modifying the optical absorbing structure within the droplet core in order to maximize the temperature rise

and thus lower the optical fluence required to produce ODV [4,7]. In addition, ODV in the near-infrared (NIR) region of the spectrum, where the optical penetration within tissue is large, has been demonstrated by incorporating NIR absorbing gold nanorods into the droplet core or clustered gold nanospheres on the droplet surface [4–6].

It has long been known that heterogeneous nucleation can be suppressed by immersing a volatile liquid, in the form of a droplet, in another nonvolatile liquid in which it has low solubility [10,11]. The liquid-liquid interface is free of solid motes and gas pockets, thus inhibiting the nucleation process and, in the case of heated droplets, leading to a superheated liquid core in a metastable state. With sufficient heating, homogeneous nucleation may occur at a temperature that is approximately 90% of the critical temperature for many substances [10–15]. It is also noted that for very small droplets, surface tension at the liquid-liquid interface can lead to a substantial increase in the pressure in the droplet core required to maintain mechanical equilibrium and further hinder bubble nucleation [16]. When large superheats occur, it can lead to explosive vaporization events once bubble nucleation is triggered, which in turn can produce a large acoustic response and potentially induce therapeutic effects in tissue.

Arguably the droplet core material is the most critical parameter to consider in the development of PFC droplets that can be triggered using a laser source at depth in biological tissue (without exceeding laser safety guidelines). In this paper, we study the effect of droplet core material on the ODV threshold with an aim towards reducing the threshold laser fluence at which ODV can be achieved. Nanoparticle-templated microbubbles with different gas cores were subjected to high pressures to induce condensation; producing nanoparticle-templated droplets. The microbubble condensation approach allowed for droplets to be produced of volatile PFCs with equilibrium boiling temperatures below room temperature, but which remain in a metastable liquid state above

room temperature. The core material is found to have a profound effect on ODV, with more volatile PFC droplets vaporizing at a lower laser fluence. The effects of droplet size on vaporization threshold are discussed, as well as a proposed mechanism for the relatively broad distribution of vaporization thresholds observed within a droplet population with the same core material.

5.3. Materials & Methods

5.3.1. Microbubble Fabrication

Microbubbles were fabricated with 1,2-diarachidoyl-*sn*-glycero-3-phosphocholine (DAPC), 1,2-distearoyl-sn-glycero-3-phosphorethanolamine-N-[methoxy (polyethylene glycol) 2000] (DSPE-PEG2K), and 1,2-distearoyl-sn-glycero-3-phospho-ethanolamine-N [biotinyl (polyethylene glycol)-2000] (DSPE-PEG2K-B) purchased from Avanti Polar Lipids (Alabaster, AL, USA). Three different PFC gas cores were used during fabrication: octafluoropropane (C_3F_8), decafluorobutane (C_4F_{10}) and dodecafluoropentane (C_5F_{12}) purchased from FlourMed (Round Rock, TX, USA) at 99% wt. purity. The boiling temperatures at ambient pressure are 236.45 K for C_3F_8, 271.19 K for C_4F_{10} and 302.39 K for C_5F_{12} [17].

The sonication method was used to fabricate bubbles with gas cores of C_3F_8 and C_4F_{10}. First a lipid solution containing DSPE-PEG2K-B, DSPE-PEG2K, and DAPC at molar ratios of 1:9:90 was heated above the phase transition temperature of DAPC (66^0 C). The lipid solution was then sonicated with a Branson 450 Sonifier (Branson, Dandurt, CT) on low power (2/10) with the tip submersed in the solution for 30 seconds to ensure the lipids were fully dispersed. The sonicator tip was moved to the gas-liquid interface and the headspace was flooded with C_3F_8 or C_4F_{10} for 10 seconds. The interface was then sonicated at full power (10/10) for 10 seconds, creating a bubbly mixture. Microbubbles were extracted with a syringe and washed three times at 100 RCF for 1

minute with a centrifuge (Eppendorf 5804 Centrifuge, Hauppauge, NY, USA) to concentrate bubbles with diameter of 4 μm and greater. The supernatant was collected and stored for nanoparticle conjugation.

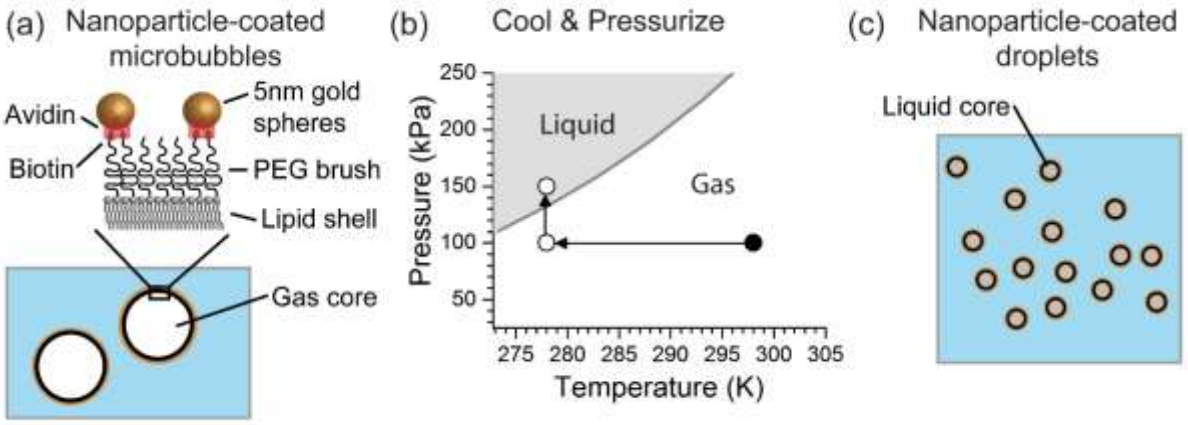

Figure 5.1 Fabrication procedure to produce nanoparticle-loaded microbubble condensed droplets. (a) Nanoparticle-loaded microbubbles are (b) cooled and pressurized to create (c) optically active droplets.

Microbubbles with a C_5F_{12} core were made using amalgamation. C_5F_{12} is a liquid at room temperature and C_5F_{12} gas was produced by heating 100 mL of liquid C_5F_{12} to 323 K in an air tight container on a hot plate. The headspace was removed by vacuum and gaseous C_5F_{12} was allowed to fill the headspace. The lipid solution was prepared in a similar fashion and identical mole fractions as described above. However, 2 mL of the heated lipid solution was extracted, placed in a 3 mL vial, and capped creating an air-tight seal. The headspace of the 3 mL vial was removed via vacuum and refilled with C_5F_{12} gas. The gas exchange process was repeated 3 times. The vial was amalgamated for 45 seconds producing a bubbly mixture. The bubbles were extracted with a syringe and removed from the 50^0 C environment for washing at 100 RCF for 1 minute to concentrate bubbles with diameter of 4 μm and greater. The supernatant was collected and placed in the heated environment for nanoparticle conjugation.

Nanoparticles were attached to the microbubble shell following a previously described avidin-biotin conjugation scheme [1]. First, the bubbles were sized to estimate the number of binding sites. Gold spheres, 5 nm in diameter with one avidin molecule per nanoparticle, were purchased from Nanopartz (Loveland, CO, USA). The nanoparticles were added to the bubble mixture at a 1:1, nanoparticle:biotin (avidin:biotin) ratio. The nanoparticle and microbubble mixture was continuously mixed with an end-over-end rotator for 2 hours. Note that the bubbles with a gas core of C_5F_{12} were mixed at an elevated temperature of 50^0 C. After 2 hours, the nanoparticle-coated microbubbles were allowed to separate from the unconjugated nanoparticles through gravitational floatation, producing nanoparticle-templated microbubbles as depicted in Fig. 5.1(a).

5.3.2. Condensation of nanoparticle-coated microbubbles

Droplets were fabricated following the condensation procedure previously described in the literature [20,32]. In brief, a two-step process (Fig. 5.1 (b)) was used to condense the microbubbles. First the nanoparticle-loaded microbubbles were placed in a syringe and cooled down in an ice bath for 30 seconds. This process lowers the required pressure for condensation. Second, a manual step in pressure (~50 psi) was applied to the syringe. The increase in pressure caused the microbubbles to condense, producing droplets with a liquid core. Before the application of pressure, the bubble mixture was pink and opaque. After pressurizing, the bubbles condensed and the mixture became transparent while remaining pink in color.

5.3.3. Droplet characterization

Microbubbles were sized via electro-impedance volumetric zone sensing using a Beckman-Coulter Multisizer III. The aperture tube was 30 μm in diameter. The microbubbles were diluted in 10 mL

of Isoton and measured to produce a size distribution. This was repeated three times and the size distributions were averaged.

The size distribution of the microbubble condensed droplets was measured by dynamic light scattering with a Malvern Nano-S90 (Worcestershire, UK). The refractive index for liquid C_4F_{10} was assumed to be 1.276 and the surrounding water was 1.348 [20]. The nanoparticle-loaded droplets were diluted in water and placed in a micro-cuvette (Zen 2112, Mavern, Worcestehshire, UK) with a total volume of 12 µL for sizing. This process was repeated 3 times and the size distributions were averaged together.

The spectra of nanoparticle-loaded droplets, nanoparticle-free droplets and nanoparticles were measured with a spectrophotometer UV-3101 (Shimadzu, Kyoto, Japan). Samples were diluted in a 1.5 mL cuvette and the absorption spectrum was measured.

5.3.4. Optical Vaporization

Optical droplet vaporization was studied using the experimental set-up shown in Fig. 5.2. The set-up consists of a dark field microscope incorporating two additional light sources; a continuous wave (CW) laser operating at 488 nm and a pulsed laser operating at 532 nm. A variable Q-switched pulsed laser with a 0.5 ns pulse width was used to induce droplet vaporization. The beam diameters of the CW and pulsed laser incident on the back of the objective were controlled to achieve 1/e beam waists of 20 µm and 15 µm, respectively, at the focal plane. The pulsed laser repetition rate was controlled with a function generator. A computer actuated attenuator was used to adjust the pulse energy such that the fluence at the sample ranged from 5 - 150 mJ/cm^2. The dynamic response of the droplets during vaporization was monitored using forward light scattering of the CW laser probe. This probe was also used to detect the dynamic response of microbubbles

to pulsed laser illumination post-vaporization. The transmitted light was collected with a lens (focal length = 20 mm) and sent through an optical bandpass filter (488 nm +/- 10 nm) to a broadband photodiode. The photodiode output was sent through a 40 dB pre-amplifier and recorded on an oscilloscope.

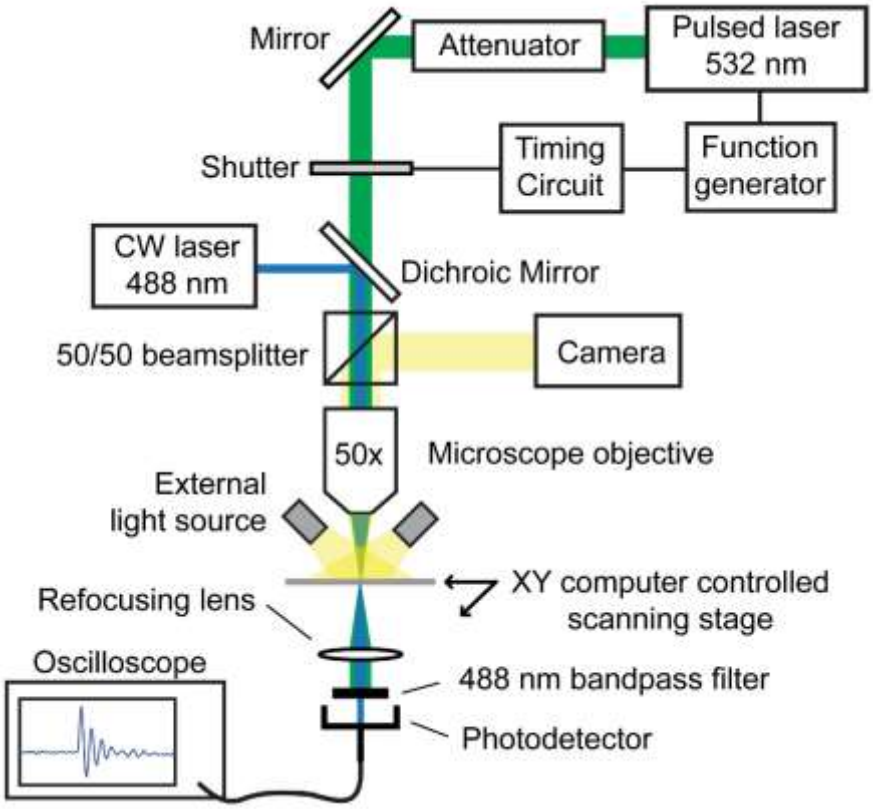

Figure 5.2 Experimental setup used to study optical droplet vaporization.

In order to measure single droplet vaporization events, the laser was operated at a 10 Hz and individual pulses selected using a computer controlled shutter. In all other experiments, the shutter remained open and the laser repetition rate was set to 1 kHz. The droplets were housed between a microscope slide and coverslip, and the edges of the coverslip sealed with vacuum grease. This arrangement was then placed on an x-y computer controlled scanning stage at the focal plane of the microscope.

5.4. Results and discussion

A histogram of the size distribution of nanoparticle-templated C_4F_{10} microbubbles before condensation and the droplets produced after condensation is shown in Fig. 5.3 (a). The median diameter of the microbubbles (shown as the dark, dashed vertical line) was 4.45 µm. Assuming conservation of mass, microbubbles with a core of C_4F_{10} would condense to droplets with a diameter 5.3 times smaller than the initial microbubble. The lighter, dashed vertical line depicts the theoretical median diameter of the droplets assuming a 5.3 fold change (0.84 µm). The measured median diameter of the droplets was 0.88 µm, close to the expected value. The absorption spectra of nanoparticle-loaded C_4F_{10} droplets, nanoparticles alone, and nanoparticle-free C_4F_{10} droplets are shown in Fig. 5.3(b). The nanoparticles show the expected absorption peak associated with the plasmon resonance wavelength around 535 nm. The spectrum for the nanoparticle loaded droplets is similar to that observed for the nanoparticles alone, indicating that the nanoparticle loading is preserved in the condensation process. In addition, the absence of a spectral shift provides evidence that there is little nanoparticle clumping or aggregation subsequent to condensation.

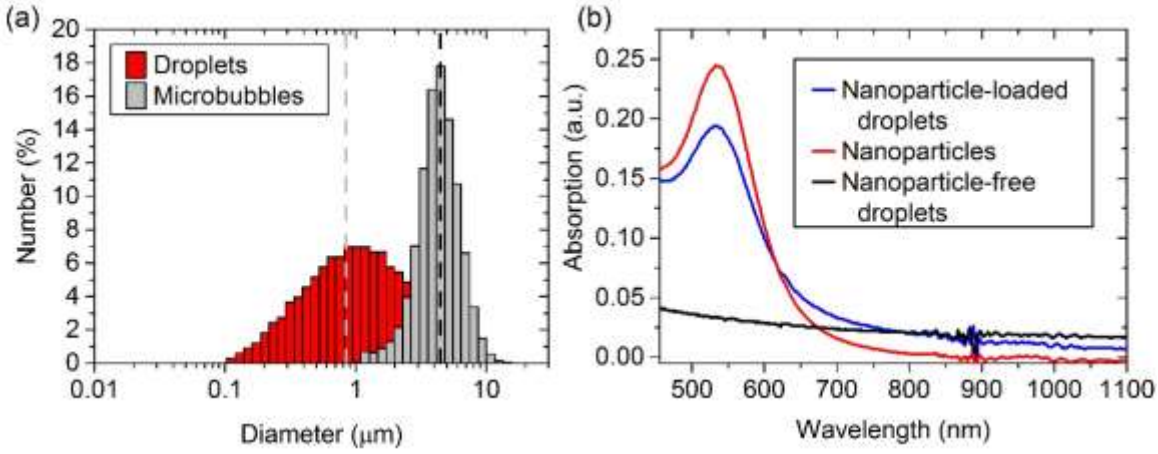

Figure 5.3 (a) Size distribution of nanoparticle-coated microbubbles and the droplets produced after condensation of the microbubbles. (b) Absorption spectra comparing nanoparticles, nanoparticle-coated droplets and nanoparticle-free droplets.

In order to investigate the dynamic response of C_4F_{10} droplets, a droplet was located within the field of view of the microscope and positioned at the center of the pulsed laser pump beam and CW probe laser. We note that due to the relatively close index of refraction match between liquid C_4F_{10} and water, droplets are generally quite difficult to locate. Nevertheless, some of the larger droplets could be identified. For this experiment, the pump laser fluence was increased in steps of 2 mJ/cm^2 and at each fluence the response from the scattered probe beam was recorded. This process was then repeated until a vaporization event was observed. Fig. 5.4(a) shows a representative result of such an experiment, where vaporization was observed at a laser fluence of 22 mJ/cm^2. The signal observed at one fluence step before vaporization (20 mJ/cm^2) is also shown in the figure. Below the optical threshold for vaporization the light level on the photodetector remained at a constant level, with any optical scattering from, for example, photothermal droplet heating below the noise level of the system. Above the vaporization threshold, the core rapidly expands and reaches a maximum diameter in approximately 1 μs. The resulting microbubble then undergoes several oscillations before reaching a steady state diameter of 7 μm. We note that the forward light scattering signal is not directly proportional to the bubble size as a vapor nuclei forms and grows into a bubble and one must take this into account when interpreting the dynamic response. Previous experiments have shown that over the limited radius range (1-6 μm), the light scattering signal reduction at the photodetector scales with the square of bubble size. We do note that a small amount of bubble growth was observed at later times (several seconds) most likely due to gas efflux and influx of the core[21,22].

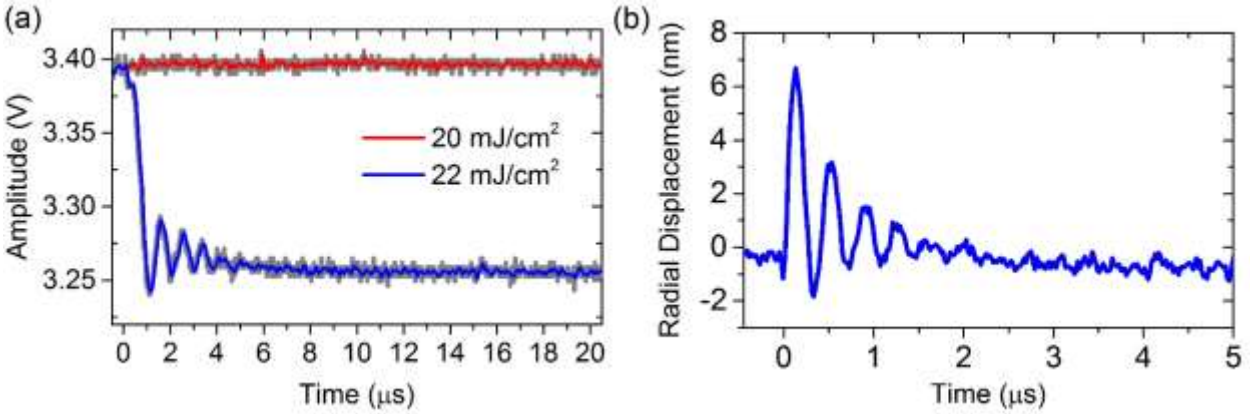

Figure 5.4 (a) The response of a droplet to a single optical pulse before vaporization at 20 mJ/cm^2 and during vaporization when the pulsed laser was increased to 22 mJ/cm^2. The unfiltered response is shown as the gray line where the solid blue and red lines have been digitally filtered with a 10 MHz low-pass filter. (b) The photoacoustic response of a microbubble produced from droplet vaporization illuminated with a fluence of 15 mJ/cm^2.

We have previously shown that nanoparticle-loaded microbubble oscillations can be induced by a pulsed laser source, and that the photoacoustic response from such microbubble populations exceeds that from free nanoparticles at the same nanoparticle concentration [1,2]. The microbubbles produced post vaporization remain optically active, indicating that the nanoparticles are not purged during the explosive vaporization of the droplet core. An example of the dynamic response of a microbubble, post C_4F_{10} droplet vaporization, is shown in Fig 4(b). Here, the vaporized bubble is positioned at the center of the pump and probe beams illuminated with a laser fluence of 15 mJ/cm^2. The fluctuation in optical power at the photodetector, averaged over 6,000 measurements, was converted to radial displacements using the previously determined conversion curve[2]. The shell elasticity can be extracted from the bubble response. Here, the bubble diameter was 3.56 μm and the measured resonant frequency was 2.67 MHz, giving a shell elasticity of 0.41 N/m. The shell elasticity is within the range, but on the lower side, of previously reported values [2]. Based on the measured bubble response one can conclude that the vaporized droplet retains a lipid shell with attached nanoparticles.

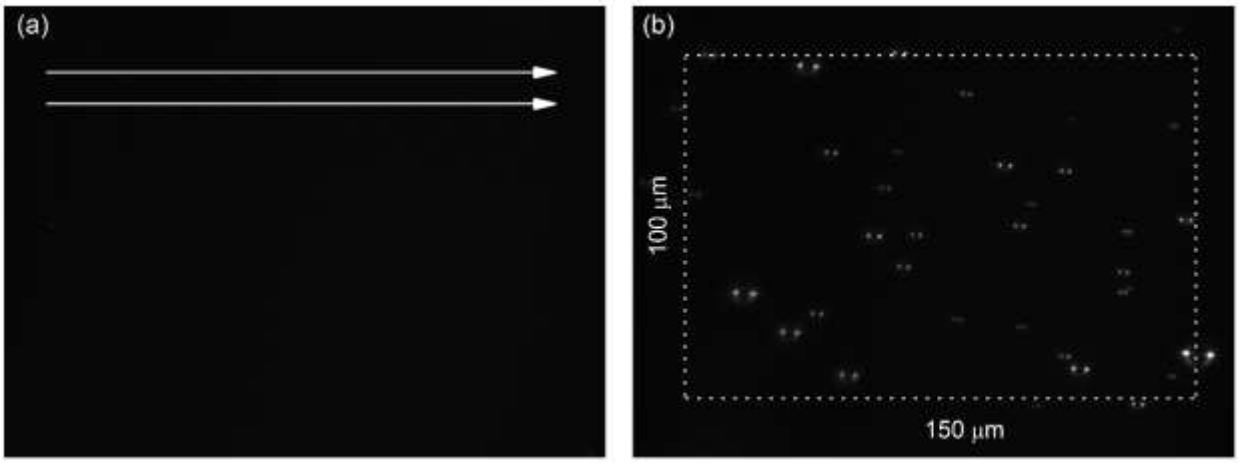

Figure 5.5 (a) The dark field microscopy image captured after scanning the pulsed laser at a fluence of 10 mJ/cm^2, the white lines with arrows indicate the scanning direction. (b) The resulting vaporized bubbles with dashed lines outlining the scanned area which is 100 μm in the vertical direction and 150 μm in the horizontal direction. The pulsed laser fluence was 50mJ/cm^2.

As mentioned earlier, it is somewhat difficult to identify droplets (particularly sub-micron droplets) within the field of view of the microscope. Rather than identify droplet position *a priori*, threshold fluence measurements were made by illuminating an area of the sample and determining the number of vaporization events that occurred at a given fluence. Here the pump laser repetition rate was set at 1 kHz, and the sample was first raster scanned over a fixed area at a low (sub threshold) laser fluence. The laser fluence was then increased and the process repeated. At each laser fluence, the number of new bubbles appearing in the scan area was determined based on the acquired dark field microscopy image. The process is illustrated in Fig. 5.5, where Fig. 5.5(a) shows the optical image after raster scanning a sample of C_4F_{10} droplets at a laser fluence of 10 mJ/cm^2, where no vaporization events (microbubbles) are observed. Fig. 5.5(b) shows the same area after a scanning with a laser fluence of 50 mJ/cm^2. Here, the majority of the droplets within the scan area have been vaporized to produce the observed microbubbles. The image also provides a means of sizing the microbubbles. This process is repeated over multiple scan areas in order to

determine the variation in the threshold fluence for droplet vaporization within droplets with a given PFC core.

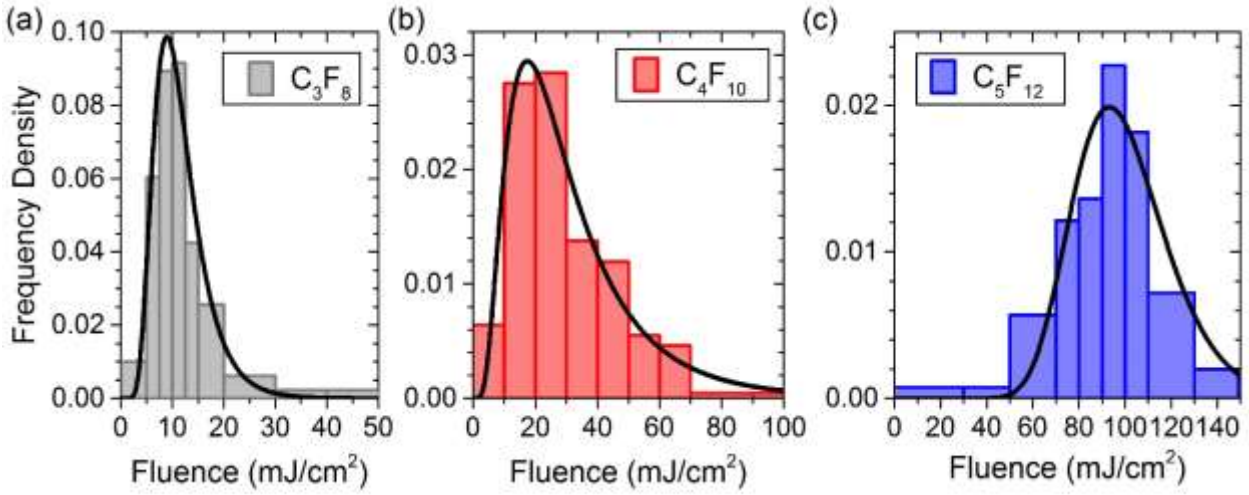

Figure 5.6 Frequency density histograms of droplet vaporization with increasing fluence for three different cores (a) C_3F_8, (b) C_4F_{10} and (c) C_5F_{12}.

The threshold fluences for vaporization of C_3F_8, C_4F_{10} and C_5F_{12} droplets was determined using the raster scan approach. Scans were performed at a given fluence step (ΔF) and the number of new vaporization events (N_f) was found. Frequency density histograms were then constructed by dividing N_f by the total number of observed vaporization events and normalizing this by ΔF, and the results are shown in Fig. 5.6 (a-c). The solid lines show the fit to a log-normal probability density function, from which a 50% threshold for droplet vaporization can be determined. C_3F_8 droplets had a 50% threshold fluence of 10.6 ± 5.1 mJ/cm^2 (mean ± standard deviation), C_4F_{10} droplets had a threshold of 26.1 ± 21.7 mJ/cm^2, and C_5F_{12} droplets at 97.4 mJ/cm^2 ± 20 mJ/cm^2. As might be expected, the lower boiling point PFCs have lower threshold fluences required for vaporization. Perhaps more relevant when considering homogeneous bubble nucleation within the droplet core, are the core material critical temperatures: 345.1 K for C_3F_8, 386.4 K for C_4F_{10} and 422 K for C_5F_{12}. Again the vaporization scales with critical temperature, with a change in droplet core from C_5F_{12} to C_3F_8 giving more than a nine fold decrease in threshold fluence. While the

results here are for gold nanospheres illuminated at a wavelength of 532 nm, we expect the same trend for any nanoparticle type and illumination wavelength so long as the droplet vaporization is triggered by linear photothermal heating processes. In particular, a low boiling point droplet arrayed with NIR absorbing nanorods may allow for droplet vaporization at significant depth in biological tissue. We also note that after optical vaporization of droplets with a C_3F_8 core the size distribution of vaporized bubbles was shifted to smaller diameters with respect to the initial microbubbles used for condensation. We hypothesize that this is due to increased dissolution of the gas core during condensation due to the increased solubility of the gas.

Droplet vaporization is initiated when a nucleus of critical size is formed within the droplet and subsequently expands into a bubble. While the spatial distribution of nanoparticles on the droplet after microbubble condensation is unkown, it is expected that they are concentrated on the periphery and lead to rapid preferential heating near the PFC/water interface. Here we assume homogeneous nucleation occurs in the PFC core at the superheat limit of approximately 90% of the critical temperature. The 50% threshold fluence plotted against 90% of the critical temperature for the three core materials is shown in Fig. 5.7(a). The dotted line shows a linear fit to the data with the intercept fixed at ambient temperature (298 K). The slope of this line (0.91 K/(mJ/cm^2)) gives a measure of the heating efficiency of the nanoparticle construct. This allows one to quantify the effectiveness of the light absorbing species in converting incident light into droplet core heating. The heating efficieny may be increased, and fluence threshold reduced, by using nanoparticles with larger absorption cross section or incorporating a different loading scheme.

The heating of a 5 nm gold nanoparticle immersed in water subject to a 0.5 ns laser pulse at wavelength of 532 nm was calculated [23]. The absorption efficiency of the nanoparticle, determined from Mie theory, is 0.29. Figure 5.7 (b) shows the heating efficiency (maximum

temperature rise normalized by the excitation laser fluence) as a function of distance from the gold-liquid interface. The horizontal dashed line shows the heating efficiency found from the linear fit of the data in Fig. 5.7(a), and the two curves intersect at a distance of 4.32 nm from the gold-water interface. The nanoparticles are attached to the droplet shell on the distal end of the PEG which is in a brush configuration. The length of the PEG brush layer can be estimated from self-consistent field theory [24,25]. First the Flory radius in a good solvent needs to be compared to the packing density to ensure the PEG is in the brush configuration. The Flory radius can be expressed as:

$$R_F \cong N^{3/5} a \tag{5.1}$$

Where, N is the number of monomers for PEG2K this is equal to 45, a is monomer size and is equal to 0.35 nm for PEG. Hence, the Flory radius for PEG2K is 3.44 nm. The distance between PEGs can be estimated from the mole fractions of the shell and the area per lipid headgroup. PEG was incorporated into the shell at a 10% mole fraction, so there are 10 lipid molecules for every one PEG. If the lipid head group area is assumed to be 0.44 nm^2, that gives a total area per PEG of 4.4 nm^2. If the PEGs are assumed to pack with a circular projection on the bubble shell the distance between PEGs is equal to the diameter of a circle with an area of 4.4 nm^2. This gives a distance between between PEGs of 2.37 nm. This confirms that the PEG packing is less than the Flory radius indicating a brush layer is formed on the microbubble surface. The time-averaged length, *L*, of the polymer brush layer can be expressed as:

$$L \cong Na\sigma^{1/3} \tag{5.2}$$

Where, σ is the normalized density of the PEG and is described as:

$$\sigma = \sqrt{\frac{a}{D}} \tag{5.3}$$

Where, D is the distance between PEGs. For a mole fraction of 10% and a lipid head group area of 0.44 nm^2 the distance between PEGs is 2.37 nm. This gives a normalized density of 0.02 and a length of the PEG brush layer of 4.40 nm. This is close the thermal length predicted from the heating efficiency estimate.

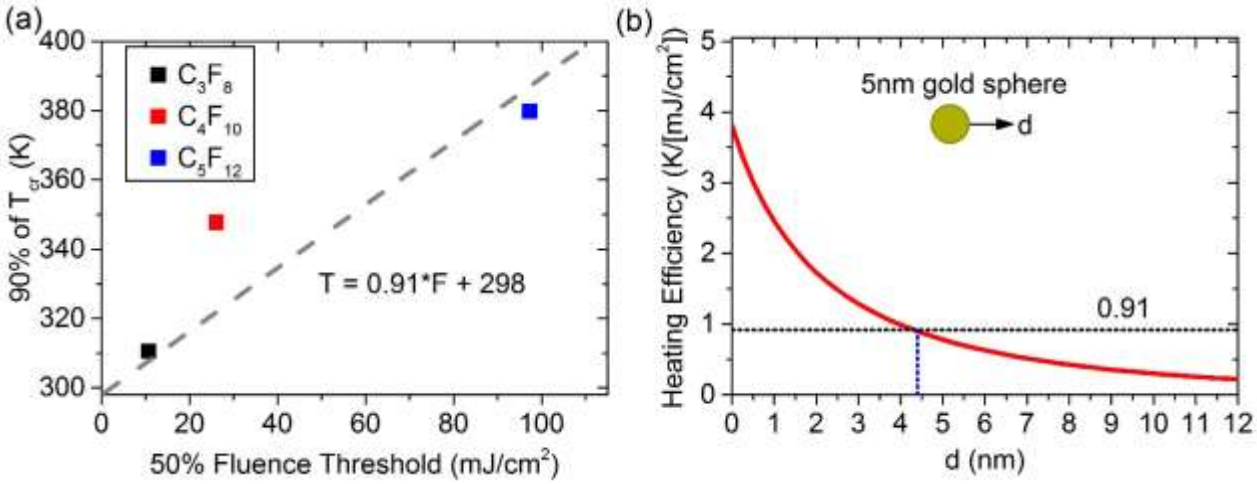

Figure 5.7 (a) The fluence to vaporize 50% of the droplets plotted against 90% of critical temperature. The gray dashed line is a linear fit to the data with a y-intercept set to 298 K. (b) The heating efficiency of a 5nm gold sphere surrounded by water is plotted as a function of the distance from gold-liquid interface. The black dotted line is the estimated heating efficiency from the experiments and the blue dotted line is the estimated length of the PEG brush layer.

This simple model also provides some insight to the broad range of threshold fluences within the droplet population observed for all three PFCs. The maximum temperature rise produced by pulsed laser heating is highly dependent on distance from the nanoparticle surface. For example, a 25% higher peak temperature occurs at a distance of 3.5 nm compared to 4.5 nm. The fluence at which the core temperature reaches the nucleation threshold is thus a strong function of the spatial configuration of the nanoparticles with respect to the core and variations in PEG coverage and nanoparticle loading between droplets may be responsible for the distribution in threshold fluences. We also note that overlapping thermal fields between closely spaced nanoparticles as

well as nanoparticle clustering also can have a strong influence on the local temperature rise [26,27].

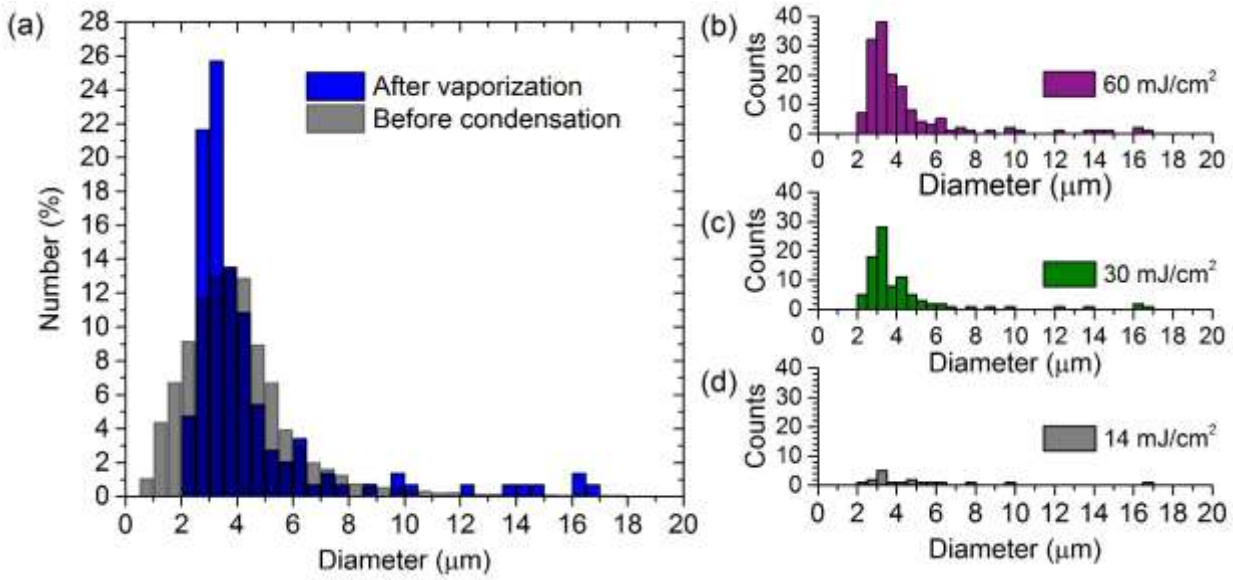

Figure 5.8 (a) Comparison of the size distribution of C_4F_{10} bubbles prior to condensation and the bubbles produced form droplet vaporization. (b-d) Size distributions of vaporized C_4F_{10} bubbles at fluences of (b) 14, (c) 30, and (d) 60 mJ/cm2.

Bubble size distributions have also been determined after laser vaporization and compared to those prior to condensation. A histogram of the size distributions for C_4F_{10} bubbles is shown in Fig. 5.8(a). The median diameters of the bubbles before condensation and after vaporization were 3.6 μm and 3.4 μm, respectively. In previous work, a small amount of gas dissolution from the microbubble was observed during the condensation process [18]. This would result in a loss of core mass leading to a slightly smaller vaporized bubble. Nevertheless, the size distribution is well-maintained through the condensation and laser induced vaporization process; an important feature of the agents for dual mode imaging applications where strong scattering from the vaporized droplet population is desired [28,29].

Figure 5.8(b-d) shows the size distributions of microbubbles produced by C_4F_{10} droplet vaporization at laser fluences of 14 mJ/cm2 (Fig. 5.8(b)), 30 mJ/cm2 (Fig. 5.8(c)), and 60 mJ/cm2 (Fig. 5.8(d)). Fitting the size histograms to a log-normal distribution, the mean diameters all found to be within 0.1 μm of 3.4 μm. We note that the vaporized droplet size distribution can be inferred from the microbubble distribution by dividing by a factor of 5.3. Interestingly, a marked shift in the size distribution of the microbubbles at different fluences is not observed.

It is expected that the primary influence of size on vaporization may stem from the surface tension at the liquid-liquid interface, causing the pressure in the droplet core to increase with decreasing droplet radius. The increased pressure in the droplet core may require a larger vapor embryo (critical nucleus) to trigger droplet vaporization and thus higher laser fluence. A critical radius, r_{cr}, of the vapor embryo can be estimated from the expression below.

$$r_{cr} = \frac{2\sigma_{core}}{10^{A-B/C+T_{vap}} - P_{core}} \tag{5.4}$$

Where σ_{core} is the surface tension of the liquid core which is 10.2mN/m for C_4F_{10}, P_{core} is the pressure of droplet core, T_{vap} is the vaporization temperature. The constants *A, B, & C* were found for the nearest temperature range from the National Institute of Standards and Technology Chemistry WebBook. The vaporization temperature was assumed to be 90% of the critical temperature, which gave a calculated vapor pressure of 1.03 MPa. Assuming a C_4F_{10} droplet with neglibible surface tension P_{core} is equal to atmospheric pressure (0.83 bar at Boulder, CO) and the estimated critical radius is 21.5 nm.

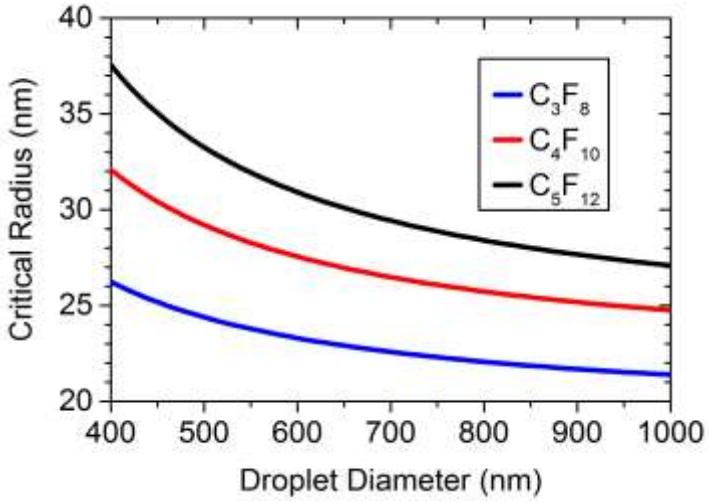

Figure 5.9 The effect of tension of liquid-liquid interface on the critical radius of the vapor bubble.

To examine the effects of surface tension, an intermediate level of compression ($\sigma_{fw}/2$) was assumed. Critical radius is plotted as a function of droplet diameter in Fig. 5.9. Here, Eqn. (5.4) was used with $P_{core} = 2\sigma_{drop}/R_{drop}$, and σ_{drop} was 31.1, 31.4, 31.8 mN/m for C_4F_8, C_4F_{10}, and C_5F_{12}, respectively. The larger the critical radius, the more energy required for vaporization. Hence, larger droplets would have a lower vaporization threshold compared to smaller droplets in Fig. 5.9. For example, a C_4F_{10} droplet with an 800nm diameter has a critical radius of 25.7 nm compared to a droplet with a 600 nm diameter the critical radius increases by 7% to 27.6 nm. It should be noted that if the surface tension at the liquid-liquid interface is increased the critical radius increases.

The droplets used in these experiments are encapsulated with a lipid monolayer, and the surface tension is influenced by the level of compression. Prediction of droplet size effects on threshold fluence is complicated by the fact that the surface tension at the PFC- water interface is not known. Referring back to Fig. 5.8, if the effects of surface tension are large, one would expect the lower fluences to primarily trigger vaporization events in larger droplets producing, in turn, larger microbubbles. The fact that this is no observed leads us to believe that the broad distribution in

threshold fluences (Fig. 5.6) is not governed by droplet size and surface tension, but rather by the distribution of nanoparticles around the droplet core.

5.5. Conclusions

In conclusion, we have demonstrated the ability to control the optical vaporization threshold through manipulation of the core material. We utilized a condensation technique for droplet fabrication and were able to produce droplets in a metastable, superheated state. The lowest threshold fluence for vaporization was 10.6 mJ/cm^2 for a C_3F_8 core. This was 9 times lower than C_5F_{12}, a commonly used core material for optical and acoustic droplet vaporizaiton. The vaporization threshold fluence could be lowered further by utilizing, for example, a nanoparticle shell that offers more efficient heating, such as nanorods which have additional benefits of absorbing in the NIR. In addition, application of ultrasound in combination with pulsed laser illumination could further reduce the optical vaporization threshold [30]. The threshold fluence for droplet vaporization was found to scale with critical temperature of the core material. Previous research has demonstrated that a range of vaporization thresholds can be achieved by utilizing a mixture of two different core materials [14,31]. This would provide an additional avenue to fine tune PFC droplets as optical probes with powerful applications in imaging or therapy.

References

[1] Dove, J. D., Murray, T. W., and Borden, M. A., 2013, "Enhanced photoacoustic response with plasmonic nanoparticle-templated microbubbles," Soft Matter, 9(32), pp. 7743–7750.

[2] Dove, J. D., Borden, M. A., and Murray, T. W., 2014, "Optically induced resonance of nanoparticle-loaded microbubbles," Opt. Lett., 39(13), pp. 3732–3735.

[3] Hannah, A., Luke, G., Wilson, K., Homan, K., and Emelianov, S., 2014, "Indocyanine Green-Loaded Photoacoustic Nanodroplets: Dual Contrast Nanoconstructs for Enhanced Photoacoustic and Ultrasound Imaging," ACS Nano, 8(1), pp. 250–259.

[4] Hannah, A. S., VanderLaan, D., Chen, Y.-S., and Emelianov, S. Y., 2014, "Photoacoustic and ultrasound imaging using dual contrast perfluorocarbon nanodroplets triggered by laser pulses at 1064 nm," Biomed. Opt. Express, 5(9), pp. 3042–3052.

[5] Wilson, K., Homan, K., and Emelianov, S., 2012, "Biomedical photoacoustics beyond thermal expansion using triggered nanodroplet vaporization for contrast-enhanced imaging," Nat Commun, 3, p. 618.

[6] Wei, C., Xia, J., Lombardo, M., Perez, C., Arnal, B., Larson-Smith, K., Pelivanov, I., Matula, T., Pozzo, L., and O'Donnell, M., 2014, "Laser-induced cavitation in nanoemulsion with gold nanospheres for blood clot disruption: in vitro results," Opt. Lett., 39(9), pp. 2599–2602.

[7] Wei, C., Lombardo, M., Larson-Smith, K., Pelivanov, I., Perez, C., Xia, J., Matula, T., Pozzo, D., and O'Donnell, M., 2014, "Nonlinear contrast enhancement in photoacoustic molecular imaging with gold nanosphere encapsulated nanoemulsions," Appl. Phys. Lett., 104(3), p. 033701.

[8] Jian, J., Liu, C., Gong, Y., Su, L., Zhang, B., Wang, Z., wang, D., Zhou, Y., Xu, F., Li, P., Zheng, Y., Song, L., and Zhou, X., 2014, "India Ink Incorporated Multifunctional Phase-transition Nanodroplets for Photoacoustic/Ultrasound Dual-modality Imaging and Photoacoustic Effect Based Tumor Therapy," Theranostics, 4(10), pp. 1026–1038.

[9] Strohm, E., Rui, M., Gorelikov, I., Matsuura, N., and Kolios, M., 2011, "Vaporization of perfluorocarbon droplets using optical irradiation," Biomed. Opt. Express, 2(6), pp. 1432–1442.

[10] Avedisian, C. T., 1985, "The Homogeneous Nucleation Limits of Liquids," J. Phys. Chem. Ref. Data, 14(3), pp. 695–729.

[11] Shepherd, J. E., and Sturtevant, B., 1982, "Rapid evaporation at the superheat limit," J. Fluid Mech., 121, pp. 379–402.

[12] Kwak, H.-Y., and Lee, S., 1991, "Homogeneous Bubble Nucleation Predicted by a Molecular Interaction Model," J. Heat Transf., 113(3), pp. 714–721.

[13] Jarvis, T. J., Donohue, M. D., and Katz, J. L., 1975, "Bubble nucleation mechanisms of liquid droplets superheated in other liquids," J. Colloid Interface Sci., 50(2), pp. 359–368.

[14] Eberhart, J. G., Kremsner, W., and Blander, M., 1975, "Metastability limits of superheated liquids: Bubble nucleation temperatures of hydrocarbons and their mixtures," J. Colloid Interface Sci., 50(2), pp. 369–378.

[15] Caupin, F., and Herbert, E., 2006, "Cavitation in water: a review," Comptes Rendus Phys., 7(9–10), pp. 1000–1017.

[16] Sheeran, P. S., Wong, V. P., Luois, S., McFarland, R. J., Ross, W. D., Feingold, S., Matsunaga, T. O., and Dayton, P. A., 2011, "Decafluorobutane as a Phase-Change Contrast Agent for Low-Energy Extravascular Ultrasonic Imaging," Ultrasound Med. Biol., 37(9), pp. 1518–1530.

[17] 1985, TRC thermodynamic tables. Non-hydrocarbons, College Station, Tex : Thermodynamics Research Center.

[18] Mountford, P. A., Sirsi, S. R., and Borden, M. A., 2014, "Condensation Phase Diagrams for Lipid-Coated Perfluorobutane Microbubbles," Langmuir, 30(21), pp. 6209–6218.

[19] Sheeran, P. S., Luois, S., Dayton, P. A., and Matsunaga, T. O., 2011, "Formulation and Acoustic Studies of a New Phase-Shift Agent for Diagnostic and Therapeutic Ultrasound," Langmuir, 27(17), pp. 10412–10420.

[20] L'Annunziata, M. F., 2012, Handbook of Radioactivity Analysis, Elsevier, Amsterdame.

[21] Kwan, J. J., and Borden, M. A., 2010, "Microbubble Dissolution in a Multigas Environment," Langmuir, 26(9), pp. 6542–6548.

[22] Sarkar, K., Katiyar, A., and Jain, P., 2009, "Growth and dissolution of an encapsulated contrast microbubble: Effects of encapsulation permeability," Ultrasound Med Biol, 35(8), pp. 1385–1396.

[23] Goldenberg, H., and Tranter, C. J., 1952, "Heat flow in an infinite medium heated by a sphere," Br. J. Appl. Phys., 3(9), pp. 296–298.

[24] De Gennes, P. G., 1980, "Conformations of Polymers Attached to an Interface," Macromolecules, 13(5), pp. 1069–1075.

[25] Borden, M. A., Zhang, H., Gillies, R. J., Dayton, P. A., and Ferrara, K. W., 2008, "A stimulus-responsive contrast agent for ultrasound molecular imaging," Biomaterials, 29(5), pp. 597–606.

[26] Khlebtsov, B., Zharov, V., Melnikov, A., Tuchin, V., and Khlebtsov, N., 2006, "Optical amplification of photothermal therapy with gold nanoparticles and nanoclusters," Nanotechnology, 17(20), p. 5167.

[27] Govorov, A. O., Zhang, W., Skeini, T., Richardson, H., Lee, J., and Kotov, N. A., 2006, "Gold nanoparticle ensembles as heaters and actuators: melting and collective plasmon resonances," Nanoscale Res. Lett., 1(1), pp. 84–90.

[28] Sirsi, S., Feshitan, J., Kwan, J., Homma, S., and Borden, M., 2010, "Effect of microbubble size on fundamental mode high frequency ultrasound imaging in mice," Ultrasound Med. Biol., 36(6), pp. 935–948.

[29] Streeter, J. E., Gessner, R., Miles, I., and Dayton, P. A., 2010, "Improving Sensitivity in Ultrasound Molecular Imaging by Tailoring Contrast Agent Size Distribution: In Vivo Studies," Mol. Imaging, 9(2), pp. 87–95.

[30] Ju, H., Roy, R. A., and Murray, T. W., 2012, "Gold nanoparticle targeted photoacoustic cavitation for potential deep tissue imaging and therapy," Biomed. Opt. Express, 4(1), pp. 66–76.

[31] Sheeran, P. S., Luois, S. H., Mullin, L. B., Matsunaga, T. O., and Dayton, P. A., 2012, "Design of ultrasonically-activatable nanoparticles using low boiling point perfluorocarbons," Biomaterials, 33(11), pp. 3262–3269.

Chapter 6

Lipid-encapsulated microbubble shell elasticity

6.1. Introduction

This chapter will cover preliminary results developing and validating a model based on simple molecular force fields that describes the shell elasticity from a lipid encapsulated microbubble. The model is based on intermolecular interactions of the hydrophobic acyl chains. Starting from the Lennard-Jones potential a theory is developed and an analytical solution for the shell elasticity is given. The model is validated by constructing plasmonic microbubbles with lipids shells of different chain lengths and measuring the shell elasticity.

6.2. Motivation

The microbubble shell elasticity has a profound impact on the dynamics of a microbubble. Most notably, the resonant frequency is shifted higher. Understanding the resonant frequency for a microbubble is extremely important for contrast enhanced imaging, drug delivery, and molecular imaging. For example, to enhance the contrast-to-tissue ratio nonlinear techniques such as sub-harmonic imaging are used. Sub-harmonic imaging is most efficient when ultrasound pulses at

twice the resonant frequency are emitted into the tissue and imaging is performed at the microbubble resonance. To date, all the information regarding microbubble shell elasticity is empirical. This work aims to provide a theoretical description of the shell elasticity based on simple molecular force fields. A theoretical understanding of shell elasticity would provide a valuable engineering tool to optimize microbubble design. In this chapter, preliminary results are given to estimate the shell elasticity based on a theoretical model that is validated through experimental results.

6.3. Derivation of the shell elasticity for a lipid-coated microbubble

This section describes the derivation of a mathematical expression for the compressibility modulus (elasticity) of a lipid monolayer coating a microbubble. The model is based on elementary force fields between lipid molecules taken from previously published data [1-4]. As derived here, the model provides *a priori* prediction of the potential energy, force, surface pressure, and elasticity as a function of lipid surface density. The model can be extended to determine other mechanical and transport properties of the lipid monolayer shell, such as surface shear viscosity, solute permeability and lateral diffusivity.

First, it is assumed that the microbubble is at rest and the lipid molecules are in mechanical equilibrium, as they would be in the leaflet of a bilayer membrane. The microbubble is neither dissolving nor growing, even as the gas core is in diffusive exchange with the surrounding medium. In this state, the lipids form a complete monolayer shell, and essentially zero gas/water interface is exposed. The lipids are close-packed and their interactions are governed by the Lennard-Jones potential:

$$w(r) = 4\varepsilon\left[\left(\frac{\sigma}{r}\right)^{12} - \left(\frac{\sigma}{r}\right)^{6}\right] \tag{6.1}$$

where ε is the depth of the potential energy well, σ is the van der Waals diameter, and r is the distance between the acyl chains. The problem is first approached by considering the interactions of the methylene (-CH_2-) groups and their nearest neighbors. The lipid head group is not included in this derivation as water molecules will act to screen the electrostatic forces, and surround the head group. Assuming hexagonal close packing, there are five in-plane neighbors (out-of-plane interactions are ignored). Summing all the nearest neighbor interactions over all the methylene groups gives:

$$W(r) = 20n\varepsilon\left[\left(\frac{\sigma}{r}\right)^{12} - \left(\frac{\sigma}{r}\right)^{6}\right] \tag{6.2}$$

where *n* is the number of methylene groups per acyl chain not counting the three that make up the ester group. The ester group is polar and is expected to interact with the surrounding water molecules which will have a screening effect on the electrostatic forces. The intermolecular force between chains is given by:

$$F(r) = -\frac{dW}{dr} = \frac{120n\varepsilon\sigma^{6}\left(2\sigma^{6} - r^{6}\right)}{r^{13}} \tag{6.3}$$

Assuming the lipid monolayer is in mechanical equilibrium (*F=0*), the packing distance, r_o, can be calculated from Eqn. (6.3). For hexagonally close-packed lipids, the area per chain (there are two chains per lipid) is related to *r* by:

$$a = \frac{\sqrt{3}}{2}r^{2} \tag{6.4}$$

The surface pressure is given by:

$$\Pi = \frac{F}{r} \tag{6.5}$$

and is related to the surface tension of a clean gas/water interface (γ_0) and the surface tension of the monolayer (γ) by the standard definition:

$$\pi = \gamma_0 - \gamma \tag{6.6}$$

The surface elasticity (equivalent to the surface compressibility modulus) is defined as:

$$\chi(r) = -a\frac{\partial \Pi}{\partial a} \tag{6.7}$$

Making the substitution for *r*:

$$\chi(r) = -\frac{r}{2}\frac{\partial \Pi}{\partial r} = \frac{240n\varepsilon\sigma^6\left(7\sigma^6 - 2r^6\right)}{r^{14}} \tag{6.8}$$

For saturated hydrocarbon chains, reported values for ε were found to vary from $6.35\text{x}10^{-22}$ J [1] to $8.20\text{x}10^{-22}$ [2]. The van der Waals diameter of the acyl chain can be found from the equilibrium packing area of the lipid in a bilayer, which is 0.471 nm^2 [3,4] and corresponds to $\sigma = 0.657\text{nm}$. Note that the van der Waals diameter of the acyl chain is larger than a single acyl chain due to the lipid head group. The calculated elasticity for *n = 16, 18, 20,* and *22* is shown in table 6.1.

Table 6.1. Calculated elasticity at the equilibrium area per lipid.

Chain Length	Elasticity (N/m) $\varepsilon = 6.35 \times 10^{-22}$	Elasticity (N/m) $\varepsilon = 8.20 \times 10^{-22}$
C16	2.73	3.53
C18	3.15	4.07
C20	3.57	4.61
C22	3.99	5.16

6.4. Experimental validation of molecular force field model

This section describes experimental measurements of the effect of lipid chain length on the shell elasticity for a lipid-encapsulated microbubble. The microbubbles were coated with gold nanoparticles, such that an optical pulse excited resonant oscillations. Microbubble oscillations were tracked with a modified microscope using a forward light scattering approach, as outlined in Chapter 4. The resonance frequency was converted to the eigenfrequency (by accounting for damping) and the shell elasticity was determined.

Experimental results measuring the shell elasticity for plasmonic microbubbles constructed from 1,2-dipalmitoyl-sn-glycero-3-phosphocholine (DPPC), 1,2-distearoyl-sn-glycero-3-phosphocholine (DSPC), 1,2-diarachidoyl-sn-glycero-3-phosphocholine (DAPC), and 1,2-dibehenoyl-sn-glycero-3-phosphocholine (DBPC) are shown in Fig 6.1. The shell elasticity was determined following the same method outlined in Chapter 4. In this experiment, only the number of methylene groups (-CH_2-) on the hydrophobic tail of the lipid was altered. DPPC had the least number of methylene groups with a chain length of 16, DSPC had a chain length of 18, DAPC had a chain length of 20, and DBPC had a chain length of 22. Molecular structures of each lipid used are included as an inset to the plots in Fig. 6.1.

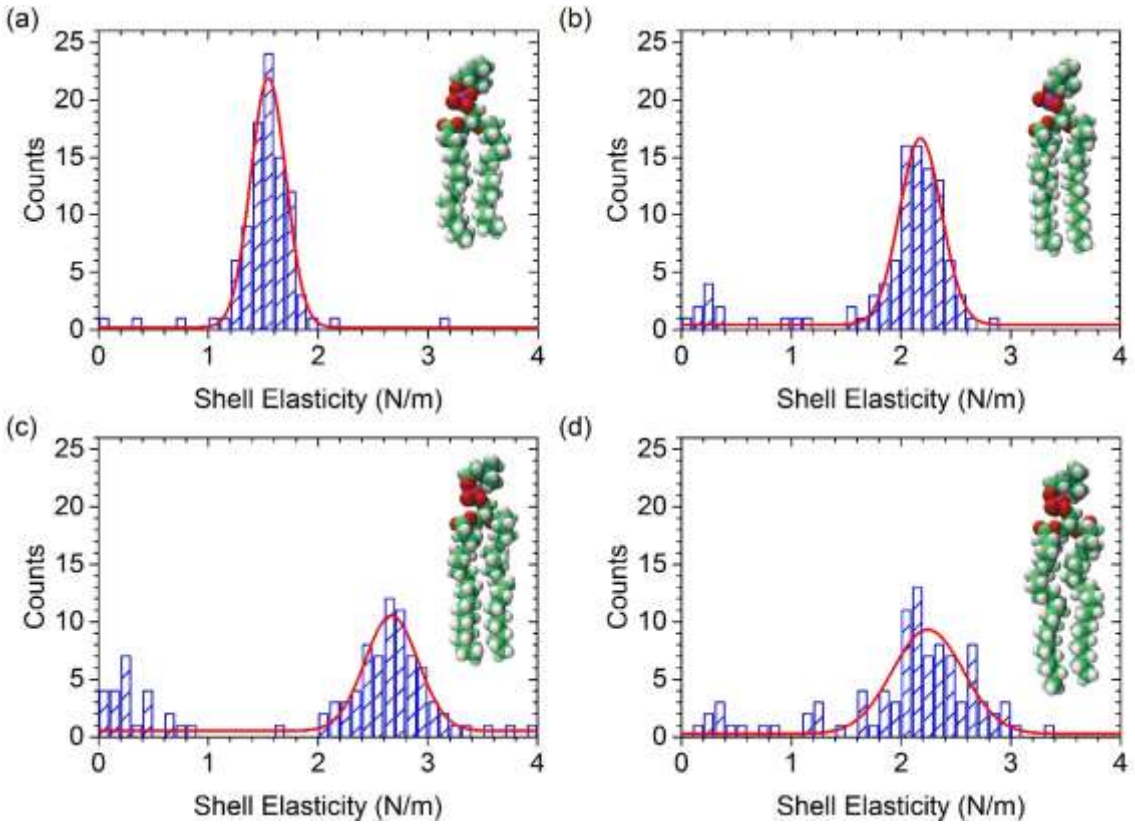

Figure 6.1 Histograms of the measured shell elasticity for plasmonic microbubbles constructed from (a) DPPC (b) DSPC (c) DAPC (d) DBPC, with the 3-dimension chemical structure of the lipid in upper-right. The red solid line is a Gaussian fit to the shell elasticities that are greater than 0.5 N/m.

For each lipid shell, a distribution of shell elasticities was measured. For DPPC, the shell elasticities took on a single distribution. However, for DSPC, DAPC, and DBPC, there were two distributions with one taking on a mean around 0 N/m. This could be due to diffusion-induced expansion of the microbubble or a buckled shell and is excluded from the following analysis. The mean shell elasticity was determined by fitting the histograms in Fig. 6.1 to a Gaussian distribution. The width of each distribution was also determined.

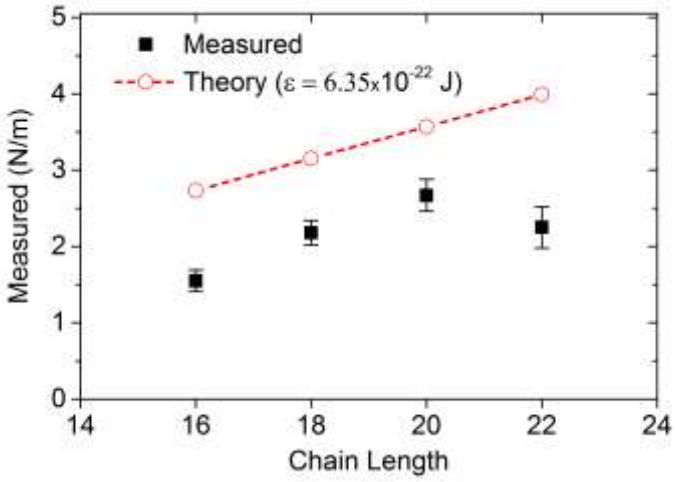

Figure 6.2 The measured mean shell elasticities for the different lipid shell compositions, where the depth of energy potential well for a single methylene group was 6.35×10^{-22} J.

The mean shell elasticity is plotted as a function of acyl chain length in Fig. 6.2. The results show that the measured shell elasticity depends on the lipid used to construct the shell, with a general trend of increasing elasticity with increasing chain length. This trend follows the theoretical prediction as the increasing number of methylene groups results in greater intermolecular forces.

6.5. Conclusions

The theoretical and experimental results are off by approximately a factor of two, with the theoretical estimates greater than the experimental measurements. The lipid shell for microbubbles used in the experiment is, of course, different than the simplified lipid shell in the theoretical model. For the model, assumptions were made that the shell is completely defect free and comprises a single lipid species. The lipid shell used in the experiments contains two lipid species with a PEG brush layer, which could affect the results. Defects present in the shell, such as folds [5], buckling [6], or grain boundaries [7], would be expected to lower the elasticity. The theoretical

model did allow for a reasonable prediction *a priori* of the shell elasticity for lipid shells with different acyl chain lengths.

References

[1] Martin, M. G., and Siepmann, J. I., 1998, "Transferable Potentials for Phase Equilibria. 1. United-Atom Description of n-Alkanes," J. Phys. Chem. B, 102(14), pp. 2569–2577.

[2] Jorgensen, W. L., and Tirado-Rives, J., 1988, "The OPLS [optimized potentials for liquid simulations] potential functions for proteins, energy minimizations for crystals of cyclic peptides and crambin," J. Am. Chem. Soc., 110(6), pp. 1657–1666.

[3] Orsi, M., and Essex, J. W., 2011, "The ELBA Force Field for Coarse-Grain Modeling of Lipid Membranes," PLoS ONE, 6(12), p. e28637.

[4] Tristram-Nagle, S., Zhang, R., Suter, R. M., Worthington, C. R., Sun, W. J., and Nagle, J. F., 1993, "Measurement of chain tilt angle in fully hydrated bilayers of gel phase lecithins," Biophysical Journal, 64(4), pp. 1097–1109.

[5] Chen, C. C., and Borden, M. A., 2010, "Ligand Conjugation to Bimodal Poly(ethylene glycol) Brush Layers on Microbubbles," Langmuir, 26(16), pp. 13183–13194.

[6] Borden, M. A., and Longo, M. L., 2002, "Dissolution Behavior of Lipid Monolayer-Coated, Air-Filled Microbubbles: Effect of Lipid Hydrophobic Chain Length," Langmuir, 18(24), pp. 9225–9233.

[7] Borden, M. A., Martinez, G. V., Ricker, J., Tsvetkova, N., Longo, M., Gillies, R. J., Dayton, P. A., and Ferrara, K. W., 2006, "Lateral Phase Separation in Lipid-Coated Microbubbles," Langmuir, 22(9), pp. 4291–4297.

Chapter 7

Conclusions

7.1. Summary of the work

Dual mode contrast agents offer improvements in contrast enhanced imaging, drug delivery and molecular imaging. In this work, a plasmonic nanoparticle-coated microbubble was studied in detail. In Chapter 2, a model describing pulsed laser heating was covered. The maximum temperature rise was found to increase with nanoparticle diameter. Depending on the heat dissipation rate of the nanoparticle, the most efficient size was found to vary from 45 nm to 80 nm in diameter. In addition, the shorter the optical pulse the higher the maximum temperature rise. The heating model was extended to a bubble with a gold shell to mimic a nanoparticle-coated microbubble. The heat flux into the gas core was determined and used to estimate an average temperature rise of the gas core. The maximum temperature within the gas core was found to be inversely related to microbubble size, with the smallest microbubble experiencing the largest temperature rise. The ideal gas law was used to couple the heated gas core into a modified Rayleigh-Plesset equation to model the dynamics of a pulsed laser heated microbubble. The maximum radial displacement and resonant frequency were examined for microbubbles with diameters from 1 to 4 μm. The maximum radial

displacement was found to increase with microbubble size. However, if a short heating pulse was used (a temporal width less than any of the bubble oscillations) the maximum radial displacement was found to decrease with microbubble size. The resonant frequency increased as microbubble size decreased and was closely related to the eigenfrequency found from the linearized Rayleigh-Plesset model. Lastly, the effect of the shell properties, specifically the elasticity and viscosity, were examined. The shell elasticity was found to increase with the resonant frequency and decrease with the radial displacement. The shell viscosity only altered the quality factor of the bubble oscillations.

In Chapter 3, the fabrication and characterization of plasmonic microbubbles was covered. An avidin-biotin conjugation scheme was presented to coat a lipid-encapsulated microbubble with gold nanospheres (5 nm in diameter). Control over nanoparticle loading density was verified with mass spectroscopy. The nanoparticle-coated microbubbles were found to enhance the photoacoustic signal from free suspensions of nanoparticles with an equivalent concentration. The synergistic enhancement was observed to remain stable over several thousand laser pulses at a fluence of 5 mJ/cm^2. However, a slight decrease in the signal over time was observed when the fluence was increased to 10 mJ/cm^2. In addition, the enhancement was diminished when the plasmonic microbubbles were destroyed using a high intensity ultrasound field which altered the spatial distribution of nanoparticles with respect to the gas core but not the overall nanoparticle concentration. Lastly, the utility of the plasmonic microbubbles as dual mode contrast agents was demonstrated. Here, the nanoparticle-coated microbubbles were flowed into a gel tissue phantom where ultrasound and photoacoustic images were reconstructed. Control images from uncoated microbubbles and free nanoparticles were also captured. The only contrast agent capable of enhancing both modalities was the plasmonic microbubble yielding a significant enhancement in the photoacoustic image.

In Chapter 4, the photoacoustic response from individual nanoparticle-coated microbubbles was examined and compared to theory. A dark field microscope was modified to incorporate a pulsed and a continuous wave laser. The pulsed laser was used to induce photothermal oscillations of the plasmonic microbubble and the continuous wave laser was used to track the bubble wall radius as a function of time using light scattering. The eigenfrequency, vibrational amplitude and quality factor were determined from the microbubble oscillations. The eigenfrequency decreased with increasing microbubble diameter, as expected from theory. The measured eigenfrequency was used to determine the shell elasticity. The quality factor from the measured bubble response was lower than that of an unshelled bubble due to a shell viscosity. The shell viscosity was determined from the quality factor of the oscillations. A shear thinning behavior was observed, where the shell viscosity was found to decrease with dilatational rate.

In Chapter 5, a high pressure was applied to the plasmonic microbubbles, condensing the gas core into a metastable liquid. The optical vaporization of the condensed plasmonic microbubble was studied. Using a forward light scattering approach, the evolution of the droplet vaporization into a microbubble was measured. Microbubbles, post-vaporization, were found to remain photoacoustically active. The effect of three different perfluorocarbon cores on the vaporization threshold fluence was studied. Core material was found to have a strong influence on the threshold fluence for vaporization, with lower boiling point cores vaporizing at a lower fluence. For each of the three core materials examined, a relativity wide distribution of threshold fluences was measured. Nanoparticle loading and geometry was proposed to cause the wide distribution in threshold fluence. In addition, the effect of size on threshold fluence was discussed. However, there was no measurable size dependence on threshold fluence for the condensed plasmonic microbubbles a

In Chapter 6, a theoretical model for the elasticity of a lipid-encapsulated microbubble was developed and compared to experimental results. The theoretical model was based on the molecular force fields from the lipid acyl chains. The potential energy, force, surface pressure, and elasticity as a function of lipid surface density was modeled. Experiments were performed on plasmonic microbubbles to validate the theoretical model. Four different shell compositions were studied and compared to theory. The experimentally measured elasticites were within a factor of two from the theoretical predictions, with the experimental measurement always lower than the theory.

7.2. Future Work

Having covered a brief summary of the accomplishments made in this work, a few suggestions to continue the work are provided.

First, the attempts to attach different nanoparticles, for example, larger gold spheres or nanorods should be explored. Currently, 5 nm gold spheres are attached to the microbubble. The absorption efficiency, calculated from Mie theory, is 0.29 when illuminated at 532 nm and is 11.9 times less than a 50 nm gold sphere which has an absorption efficiency of 3.46. In addition, the optical absorption band of nanorods can be tuned to wavelength in the near-infrared where human tissue is most transparent. Alterations of the nanoparticle shell would offer benefits in enhanced photothermal effects and improved optical penetration into tissue.

Secondly, the detection of optically activated microbubble oscillations can be improved. To use the plasmonic microbubble as a resonant-based sensor the time required to make a measurement needs to be decreased. Currently, a pulsed laser is used to drive bubble oscillations, as outlined in Chapter 4. To achieve a good signal-to-noise ratio (SNR), over 100,000 signal averages had to be

performed, dramatically increasing the time required to acquire a measurement. Considering the optical pulse is on the order of 1 ns and the bubble oscillations are 1 μs, only a small fraction of the excitation energy goes into driving the resonant oscillations. A more efficient means of driving plasmonic microbubble would be matching the drive frequency to the bubble resonance. Instead of using a pulsed laser to excite the bubble a continuous wave laser could be modulated with frequencies around the bubble resonance. Detection of the scattered light with a photodetector and lock-in amplifier could offer dramatic improvements in the SNR and lower the time required to measure the microbubble resonance.

Thirdly, the vaporization threshold for condensed plasmonic microbubbles could be further lowered. The current design places the nanoparticles approximately 4.4 nm from the perfluorocarbon core. The maximum temperature rise scales with the inverse distance from the nanoparticle core, with the largest temperature rise at the nanoparticle surface. To continue to lower the threshold fluence, the nanoparticle location with respect to the core needs to be studied. Here, nanoparticles could be attached to a PEG brush layer of varying thicknesses. For example, PEG2K contains 45 monomers while PEG5K has 90. In addition, the nanoparticle could be attached directly to lipid. As the maximum temperature rise occurs at the nanoparticle-liquid interface, it is hypothesized that attaching the nanoparticle directly to the lipid would result in the lowest fluence threshold for vaporization.

A fourth suggestion is to improve the shell elasticity model. The fact that the lipid head group is surrounded by water significantly complicates the calculations. The Lennard-Jones potential does not capture the complex interactions that occur as the water molecules interact with the head group. Currently, the model accounts for the lipid head group by finding an effective van der Waals diameter of the methylene group from previously reported values for the equilibrium packing area

of a lipid. A better model may be constructed that accounts for the head group components and uses only the Lennard-Jones parameters while still arriving at the correct equilibrium packing area. Here, changes in the head group and tails could be made in the same analytical expression. In addition, the effect of the microbubble shell microstructure on the shell elasticity needs to be understood. Adding an optical probe, such as a fluorescent dye, to the shell would allow for defects such as folds to be quantified. Experiments on microbubbles with and without shell defects would be beneficial in comparing the theoretical model to experimental measurements.

Finally, experiments need to be performed that demonstrate the benefits of the plasmonic microbubbles *in vitro* and *in vivo*. The unique ability of the plasmonic microbubbles to be tracked before and after microbubble destruction may allow for monitoring of drug delivery and feedback to control the delivery process. Here a drug would be loaded onto the plasmonic microbubble shell. Low intensity ultrasound imaging could image the plasmonic microbubbles to the targeted region. High intensity ultrasound would destroy the plasmonic microbubble and release the drug (and nanoparticles). Continued photoacoustic imaging would provide a measure of the amount of drug delivered to the targeted region. This technique could be demonstrated first *in vitro*, using a tissue phantom, and eventually move to *in vivo* experiments.

Bibliography

Agarwal, A., Huang, S.W., O'Donnell, M., Day, K.C., Day, M., Kotov, N., Ashkenazi, S., 2007. Targeted gold nanorod contrast agent for prostate cancer detection by photoacoustic imaging. J. Appl. Phys. 102, 064701–064701–4.

Ainslie, A, M., Leighton, G, T., 2011. Review of scattering and extinction cross-sections, damping factors, and resonance frequencies of a spherical gas bubble. J. Acoust. Soc. Am. 130, 3184–3208.

Avedisian, C.T., 1985. The Homogeneous Nucleation Limits of Liquids. J. Phys. Chem. Ref. Data 14, 695–729.

Baish, J.W., Stylianopoulos, T., Lanning, R.M., Kamoun, W.S., Fukumura, D., Munn, L.L., Jain, R.K., 2011. Scaling rules for diffusive drug delivery in tumor and normal tissues. Proc. Natl. Acad. Sci. 108, 1799–1803.

Beard, P., 2011. Biomedical photoacoustic imaging. Interface Focus 1, 602 –631.

Benchimol, M.J., Hsu, M.J., Schutt, C.E., Hall, D.J., Mattrey, R.F., Esener, S.C., 2013. Phospholipid/carbocyanine dye-shelled microbubbles as ultrasound-modulated fluorescent contrast agents. Soft Matter 9, 2384–2388.

Biagi, E., Breschi, L., Vannacci, E., Masotti, L., 2007. Stable and transient subharmonic emissions from isolated contrast agent microbubbles. IEEE Trans. Ultrason. Ferroelectr. Freq. Control 54, 480–497.

Bloch, S.H., Wan, M., Dayton, P.A., Ferrara, K.W., 2004. Optical observation of lipid- and polymer-shelled ultrasound microbubble contrast agents. Appl. Phys. Lett. 84, 631.

Bohren, C.F., Clothiaux, E., Huffman, D.R., 2010. Absorption and Scattering of Light by Small Particles. Wiley-VCH.

Borden, M. A., and Longo, M. L., 2002. Dissolution Behavior of Lipid Monolayer-Coated, Air-Filled Microbubbles: Effect of Lipid Hydrophobic Chain Length. Langmuir, 18, 9225–9233.

Borden, M. A., Martinez, G. V., Ricker, J., Tsvetkova, N., Longo, M., Gillies, R. J., Dayton, P. A., and Ferrara, K. W., 2006. Lateral Phase Separation in Lipid-Coated Microbubbles. Langmuir, 22, 4291–4297.

Borden, M.A., Streeter, J.E., Sirsi, S., Dayton, P.A., 2012. In Vivo Demonstration of Cancer Molecular Imaging with Ultrasound Radiation Force and Buried-ligand Microbubbles. Mol. Imaging 12, 1–8.

Borden, M.A., Zhang, H., Gillies, R.J., Dayton, P.A., Ferrara, K.W., 2008. A stimulus-responsive contrast agent for ultrasound molecular imaging. Biomaterials 29, 597–606.

Brown, J.M., Giaccia, A.J., 1998. The Unique Physiology of Solid Tumors: Opportunities (and Problems) for Cancer Therapy. Cancer Res. 58, 1408–1416.

Caskey, C.F., Hu, X., Ferrara, K.W., 2011. Leveraging the power of ultrasound for therapeutic design and optimization. J. Controlled Release 156, 297–306.

Caupin, F., Herbert, E., 2006. Cavitation in water: a review. Comptes Rendus Phys., Nucleation Nucléation 7, 1000–1017.

Chadderdon, S.M., Kaul, S., 2010. Molecular imaging with contrast enhanced ultrasound. J. Nucl. Cardiol. Off. Publ. Am. Soc. Nucl. Cardiol. 17, 667–677.

Chen, C.C., Borden, M.A., 2010. Ligand Conjugation to Bimodal Poly(ethylene glycol) Brush Layers on Microbubbles. Langmuir 26, 13183–13194.

Chen, C.C., Sirsi, S.R., Homma, S., Borden, M.A., 2012. Effect of Surface Architecture on In Vivo Ultrasound Contrast Persistence of Targeted Size-Selected Microbubbles. Ultrasound Med. Biol. 38, 492–503.

Chen, H., Kreider, W., Brayman, A.A., Bailey, M.R., Matula, T.J., 2011. Blood Vessel Deformations on Microsecond Time Scales by Ultrasonic Cavitation. Phys. Rev. Lett. 106, 034301.

Chen, W.-S., Matula, T.J., Brayman, A.A., Crum, L.A., 2003. A comparison of the fragmentation thresholds and inertial cavitation doses of different ultrasound contrast agents. J. Acoust. Soc. Am. 113, 643–651.

Chen, X., Wang, J., Versluis, M., Jong, N. de, Villanueva, F.S., 2013. Ultra-fast bright field and fluorescence imaging of the dynamics of micrometer-sized objects. Rev. Sci. Instrum. 84, 063701.

Chomas, J.E., Dayton, P.A., May, D., Allen, J., Klibanov, A., Ferrara, K., 2000. Optical observation of contrast agent destruction. Appl. Phys. Lett. 77, 1056.

Dayton, P.A., Morgan, K.E., Klibanov, A.L., Brandenburger, G.H., Ferrara, K.W., 1999. Optical and acoustical observations of the effects of ultrasound on contrast agents. IEEE Trans. Ultrason. Ferroelectr. Freq. Control 46, 220–232.

De Gennes, P.G., 1980. Conformations of Polymers Attached to an Interface. Macromolecules 13, 1069–1075.

De Jong, N., Emmer, M., Chin, C.T., Bouakaz, A., Mastik, F., Lohse, D., Versluis, M., 2007. "Compression-Only" Behavior of Phospholipid-Coated Contrast Bubbles. Ultrasound Med. Biol. 33, 653–656.

Dicker, S., Mleczko, M., Siepmann, M., Wallace, N., Sunny, Y., Bawiec, C.R., Schmitz, G., Lewin, P., Wrenn, S.P., 2013. Influence of Shell Composition on the Resonance Frequency of Microbubble Contrast Agents. Ultrasound Med. Biol. 39, 1292–1302.

Doinikov, A.A., Bouakaz, A., 2011. Review of shell models for contrast agent microbubbles. IEEE Trans. Ultrason. Ferroelectr. Freq. Control 58, 981–993.

Dove, J.D., Borden, M.A., Murray, T.W., 2014. Optically induced resonance of nanoparticle-loaded microbubbles. Opt. Lett. 39, 3732–3735.

Dove, J.D., Murray, T.W., Borden, M.A., 2013. Enhanced photoacoustic response with plasmonic nanoparticle-templated microbubbles. Soft Matter 9, 7743–7750.

Eberhart, J.G., Kremsner, W., Blander, M., 1975. Metastability limits of superheated liquids: Bubble nucleation temperatures of hydrocarbons and their mixtures. J. Colloid Interface Sci. 50, 369–378.

Eckersley, R.J., Chin, C.T., Burns, P.N., 2005. Optimising phase and amplitude modulation schemes for imaging microbubble contrast agents at low acoustic power. Ultrasound Med. Biol. 31, 213–219.

Eghtedari, M., Oraevsky, A., Copland, J.A., Kotov, N.A., Conjusteau, A., Motamedi, M., 2007. High Sensitivity of In Vivo Detection of Gold Nanorods Using a Laser Optoacoustic Imaging System. Nano Lett 7, 1914–1918.

Emelianov, S.Y., Li, P.-C., O'Donnell, M., 2009. Photoacoustics for molecular imaging and therapy. Phys. Today 62, 34–39.

Espinosa, G., López-Montero, I., Monroy, F., Langevin, D., 2011. Shear rheology of lipid monolayers and insights on membrane fluidity. Proc. Natl. Acad. Sci. 108, 6008–6013.

Farrer, R.A., Butterfield, F.L., Chen, V.W., Fourkas, J.T., 2005. Highly Efficient Multiphoton-Absorption-Induced Luminescence from Gold Nanoparticles. Nano Lett. 5, 1139–1142.

Ferrara, K., Pollard, R., Borden, M., 2007. Ultrasound Microbubble Contrast Agents: Fundamentals and Application to Gene and Drug Delivery. Annu. Rev. Biomed. Eng. 9, 415–447.

Feshitan, J.A., Chen, C.C., Kwan, J.J., Borden, M.A., 2009. Microbubble size isolation by differential centrifugation. J. Colloid Interface Sci. 329, 316–324.

Feshitan, J.A., Vlachos, F., Sirsi, S.R., Konofagou, E.E., Borden, M.A., 2012. Theranostic Gd(III)-lipid microbubbles for MRI-guided focused ultrasound surgery. Biomaterials 33, 247–255.

Frinking, P.J.., Bouakaz, A., Kirkhorn, J., Ten Cate, F.J., de Jong, N., 2000. Ultrasound contrast imaging: current and new potential methods. Ultrasound Med. Biol. 26, 965–975.

Garg, S., Thomas, A.A., Borden, M.A., 2013. The effect of lipid monolayer in-plane rigidity on in vivo microbubble circulation persistence. Biomaterials 34, 6862–6870.

Gelderblom, E.C., Vos, H.J., Mastik, F., Faez, T., Luan, Y., Kokhuis, T.J.A., van der Steen, A.F.W., Lohse, D., De Jong, N., Versluis, M., 2012. Brandaris 128 ultra-high-speed imaging facility: 10 years of operation, updates, and enhanced features. Rev. Sci. Instrum. 83, 103706–103706–11.

Gessner, R.C., Streeter, J.E., Kothadia, R., Feingold, S., Dayton, P.A., 2012. An In Vivo Validation of the Application of Acoustic Radiation Force to Enhance the Diagnostic Utility of Molecular Imaging Using 3-D Ultrasound. Ultrasound Med. Biol. 38, 651–660.

Gessner, R., Dayton, P.A., 2010. Advances in Molecular Imaging with Ultrasound. Mol. Imaging 9, 117–127.

Goertz, D.E., Frijlink, M.E., Tempel, D., Bhagwandas, V., Gisolf, A., Krams, R., de Jong, N., van der Steen, A.F.W., 2007. Subharmonic Contrast Intravascular Ultrasound for Vasa Vasorum Imaging. Ultrasound Med. Biol. 33, 1859–1872.

Goldberg, B.B., Liu, J.-B., Forsberg, F., 1994. Ultrasound contrast agents: A review. Ultrasound Med. Biol. 20, 319–333.

Goldenberg, H., Tranter, C.J., 1952. Heat flow in an infinite medium heated by a sphere. Br. J. Appl. Phys. 3, 296–298.

Govorov, A.O., Zhang, W., Skeini, T., Richardson, H., Lee, J., Kotov, N.A., 2006. Gold nanoparticle ensembles as heaters and actuators: melting and collective plasmon resonances. Nanoscale Res. Lett. 1, 84–90.

Gramiak, R., Shah, P.M., 1968. Echocardiography of the aortic root. Invest. Radiol. 3, 356–366.

Guan, J., Matula, T.J., 2004. Using light scattering to measure the response of individual ultrasound contrast microbubbles subjected to pulsed ultrasound in vitro. J. Acoust. Soc. Am. 116, 2832.

Hannah, A., Luke, G., Wilson, K., Homan, K., Emelianov, S., 2014. Indocyanine Green-Loaded Photoacoustic Nanodroplets: Dual Contrast Nanoconstructs for Enhanced Photoacoustic and Ultrasound Imaging. ACS Nano 8, 250–259.

Hannah, A.S., VanderLaan, D., Chen, Y.-S., Emelianov, S.Y., 2014. Photoacoustic and ultrasound imaging using dual contrast perfluorocarbon nanodroplets triggered by laser pulses at 1064 nm. Biomed. Opt. Express 5, 3042–3052.

Helfield, B.L., Cherin, E., Foster, F.S., Goertz, D.E., 2012. Investigating the Subharmonic Response of Individual Phospholipid Encapsulated Microbubbles at High Frequencies: A Comparative Study of Five Agents. Ultrasound Med. Biol. 38, 846–863.

Helfield, B.L., Goertz, D.E., 2013. Nonlinear resonance behavior and linear shell estimates for Definity[trademark sign] and MicroMarker[trademark sign] assessed with acoustic microbubble spectroscopy. J. Acoust. Soc. Am. 133, 1158–1168.

Hernot, S., Klibanov, A.L., 2008. Microbubbles in ultrasound-triggered drug and gene delivery. Adv. Drug Deliv. Rev. 60, 1153–1166.

Hoff, L., 2001. Acoustic Characterization of Contrast Agents for Medical Ultrasound IMaging, 1st ed. Springer.

Holt, R.G., Crum, L.A., 1990. Mie scattering used to determine spherical bubble oscillations. Appl. Opt. 29, 4182–4191.

Hsu, M.J., Eghtedari, M., Goodwin, A.P., Hall, D.J., Mattrey, R.F., Esener, S.C., 2011. Characterization of individual ultrasound microbubble dynamics with a light-scattering system. J. Biomed. Opt. 16, 067002.

Huang, X., Qian, W., El-Sayed, I.H., El-Sayed, M.A., 2007. The potential use of the enhanced nonlinear properties of gold nanospheres in photothermal cancer therapy. Lasers Surg. Med. 39, 747–753.

Huynh, E., Lovell, J.F., Helfield, B.L., Jeon, M., Kim, C., Goertz, D.E., Wilson, B.C., Zheng, G., 2012. Porphyrin Shell Microbubbles with Intrinsic Ultrasound and Photoacoustic Properties. J. Am. Chem. Soc.

Inaba, Y., Lindner, J.R., 2012. Molecular imaging of disease with targeted contrast ultrasound imaging. Transl. Res. 159, 140–148.

Israelachvili, J.N., 1992, Intermolecular and Surface Forces, Second Edition: With Applications to Colloidal and Biological Systems, Academic Press.

Iyer, A.K., Khaled, G., Fang, J., Maeda, H., 2006. Exploiting the enhanced permeability and retention effect for tumor targeting. Drug Discov. Today 11, 812–818.

Jain, P.K., Huang, X., El-Sayed, I.H., El-Sayed, M.A., 2008. Noble Metals on the Nanoscale: Optical and Photothermal Properties and Some Applications in Imaging, Sensing, Biology, and Medicine. Acc. Chem. Res. 41, 1578–1586.

Jain, P.K., Lee, K.S., El-Sayed, I.H., El-Sayed, M.A., 2006. Calculated Absorption and Scattering Properties of Gold Nanoparticles of Different Size, Shape, and Composition: Applications in Biological Imaging and Biomedicine. J. Phys. Chem. B 110, 7238–7248.

Jarvis, T.J., Donohue, M.D., Katz, J.L., 1975. Bubble nucleation mechanisms of liquid droplets superheated in other liquids. J. Colloid Interface Sci. 50, 359–368.

Jeon, M., Song, W., Huynh, E., Kim, J., Kim, J., Helfield, B.L., Leung, B.Y.C., Goertz, D.E., Zheng, G., Oh, J., Lovell, J.F., Kim, C., 2014. Methylene blue microbubbles as a model dual-modality contrast agent for ultrasound and activatable photoacoustic imaging. J. Biomed. Opt. 19, 016005–016005.

Jian, J., Liu, C., Gong, Y., Su, L., Zhang, B., Wang, Z., wang, D., Zhou, Y., Xu, F., Li, P., Zheng, Y., Song, L., Zhou, X., 2014. India Ink Incorporated Multifunctional Phase-transition Nanodroplets for Photoacoustic/Ultrasound Dual-modality Imaging and Photoacoustic Effect Based Tumor Therapy. Theranostics 4, 1026–1038.

Jorgensen, W. L., and Tirado-Rives, J., 1988. The OPLS [optimized potentials for liquid simulations] potential functions for proteins, energy minimizations for crystals of cyclic peptides and crambin, J. Am. Chem. Soc., 11, 1657–1666.

Ju, H., Roy, R.A., Murray, T.W., 2012. Gold nanoparticle targeted photoacoustic cavitation for potential deep tissue imaging and therapy. Biomed. Opt. Express 4, 66–76.

Katiyar, A., Sarkar, K., Jain, P., 2009. Effects of encapsulation elasticity on the stability of an encapsulated microbubble. J. Colloid Interface Sci. 519–525.

Kaul, S., 2008. Myocardial Contrast Echocardiography A 25-Year Retrospective. Circulation 118, 291–308.

Ke, H., Xing, Z., Zhao, B., Wang, J., Liu, J., Guo, C., Yue, X., Liu, S., Tang, Z., Dai, Z., 2009. Quantum-dot-modified microbubbles with bi-mode imaging capabilities. Nanotechnology 20, 425105.

Kerker, M., 1969. The scattering of light, and other electromagnetic radiation. Academic Press.

Kheirolomoom, A., Dayton, P.A., Lum, A.F.H., Little, E., Paoli, E.E., Zheng, H., Ferrara, K.W., 2007. Acoustically-active microbubbles conjugated to liposomes: Characterization of a proposed drug delivery vehicle. J. Controlled Release 118, 275–284.

Khlebtsov, B., Zharov, V., Melnikov, A., Tuchin, V., Khlebtsov, N., 2006. Optical amplification of photothermal therapy with gold nanoparticles and nanoclusters. Nanotechnology 17, 5167.

Kim, C., Cho, E.C., Chen, J., Song, K.H., Au, L., Favazza, C., Zhang, Q., Cobley, C.M., Gao, F., Xia, Y., Wang, L.V., 2010a. In Vivo Molecular Photoacoustic Tomography of Melanomas Targeted by Bioconjugated Gold Nanocages. ACS Nano 4, 4559–4564.

Kim, C., Erpelding, T.N., Jankovic, L., Pashley, M.D., Wang, L.V., 2010b. Deeply penetrating in vivo photoacoustic imaging using a clinical ultrasound array system. Biomed. Opt. Express 1, 278–284.

Kim, C., Qin, R., Xu, J.S., Wang, L.V., Xu, R., 2010c. Multifunctional microbubbles and nanobubbles for photoacoustic and ultrasound imaging. J. Biomed. Opt. 15, 010510.

Klibanov, A.L., Rychak, J.J., Yang, W.C., Alikhani, S., Li, B., Acton, S., Lindner, J.R., Ley, K., Kaul, S., 2006. Targeted ultrasound contrast agent for molecular imaging of inflammation in high-shear flow. Contrast Media Mol. Imaging 1, 259–266.

Kruger, R.A., Lam, R.B., Reinecke, D.R., Rio, S.P.D., Doyle, R.P., 2010. Photoacoustic angiography of the breast. Med. Phys. 37, 6096–6100.

Kruse, D.E., Ferrara, K.W., 2005. A new imaging strategy using wideband transient response of ultrasound contrast agents. IEEE Trans. Ultrason. Ferroelectr. Freq. Control 52, 1320–1329.

Kwak, H.-Y., Lee, S., 1991. Homogeneous Bubble Nucleation Predicted by a Molecular Interaction Model. J. Heat Transf. 113, 714–721.

Kwan, J.J., Borden, M.A., 2010. Microbubble Dissolution in a Multigas Environment. Langmuir 26, 6542–6548.

Kwan, J.J., Borden, M.A., 2012. Lipid monolayer dilatational mechanics during microbubble gas exchange. Soft Matter 8, 4756–4766.

L'Annunziata, M.F., 2012. Handbook of Radioactivity Analysis. Elsevier, Amsterdame.

Lapotko, D., 2009. Optical excitation and detection of vapor bubbles around plasmonic nanoparticles. Opt. Express 17, 2538–2556.

Lauterborn, W., Kurz, T., 2010. Physics of bubble oscillations. Rep. Prog. Phys. 73, 106501.

Leckband, D.E., Schmitt, F.-J., Israelachvili, J.N., Knoll, W., 1994. Direct Force Measurements of Specific and Nonspecific Protein Interactions. Biochemistry (Mosc.) 33, 4611–4624.

Leighton, T., 1994. The Acoustic Bubble. Academic Press.

Lentacker, I., De Smedt, S.C., Demeester, J., Van Marck, V., Bracke, M., Sanders, N.N., 2007. Lipoplex-Loaded Microbubbles for Gene Delivery: A Trojan Horse Controlled by Ultrasound. Adv. Funct. Mater. 17, 1910–1916.

Lentacker, I., Wang, N., Vandenbroucke, R.E., Demeester, J., De Smedt, S.C., Sanders, N.N., 2009. Ultrasound Exposure of Lipoplex Loaded Microbubbles Facilitates Direct Cytoplasmic Entry of the Lipoplexes. Mol. Pharm. 6, 457–467.

Lewinski, N., Colvin, V., Drezek, R., 2008. Cytotoxicity of Nanoparticles. Small 4, 26–49.

Li, C., Wang, L.V., 2009. Photoacoustic tomography and sensing in biomedicine. Phys. Med. Biol. 54, R59–R97.

Li, D.S., Kripfgans, O.D., Fabiilli, M.L., Fowlkes, J.B., Bull, J.L., 2014. Initial nucleation site formation due to acoustic droplet vaporization. Appl. Phys. Lett. 104, 063703.

Lindner, J.R., Coggins, M.P., Kaul, S., Klibanov, A.L., Brandenburger, G.H., Ley, K., 2000. Microbubble Persistence in the Microcirculation During Ischemia/Reperfusion and Inflammation Is Caused by Integrin- and Complement-Mediated Adherence to Activated Leukocytes. Circulation 101, 668–675.

Luan, Y., Lajoinie, G., Gelderblom, E., Skachkov, I., van der Steen, A.F.W., Vos, H.J., Versluis, M., De Jong, N., n.d. Lipid Shedding from Single Oscillating Microbubbles. Ultrasound Med. Biol.

Luke, G.P., Yeager, D., Emelianov, S.Y., 2012. Biomedical Applications of Photoacoustic Imaging with Exogenous Contrast Agents. Ann. Biomed. Eng. 40, 422–437.

Lum, A.F.H., Borden, M.A., Dayton, P.A., Kruse, D.E., Simon, S.I., Ferrara, K.W., 2006. Ultrasound radiation force enables targeted deposition of model drug carriers loaded on microbubbles. J. Controlled Release 111, 128–134.

Lu, W., Huang, Q., Ku, G., Wen, X., Zhou, M., Guzatov, D., Brecht, P., Su, R., Oraevsky, A., Wang, L.V., Li, C., 2010. Photoacoustic imaging of living mouse brain vasculature using hollow gold nanospheres. Biomaterials 31, 2617–2626.

Mallidi, S., Larson, T., Tam, J., Joshi, P.P., Karpiouk, A., Sokolov, K., Emelianov, S., 2011. Multiwavelength Photoacoustic Imaging and Plasmon Resonance Coupling of Gold Nanoparticles for Selective Detection of Cancer. Nano Lett 9, 2825–2831.

Marmottant, P., Meer, S. van der, Emmer, M., Versluis, M., Jong, N. de, Hilgenfeldt, S., Lohse, D., 2005. A model for large amplitude oscillations of coated bubbles accounting for buckling and rupture. J. Acoust. Soc. Am. 118, 3499–3505.

Martin, M.G., Siepmann, J.I., 1998. Transferable Potentials for Phase Equilibria. 1. United-Atom Description of n-Alkanes. J. Phys. Chem. B 102, 2569–2577.

Matsunaga, T.O., Sheeran, P.S., Luois, S., Streeter, J.E., Mullin, L.B., Banerjee, B., Dayton, P.A., 2012. Phase-Change Nanoparticles Using Highly Volatile Perfluorocarbons: Toward a Platform for Extravascular Ultrasound Imaging. Theranostics 2, 1185–1198.

Mauldin, F.W.J., Dhanaliwala, A.H., Patil, A.V., Hossack, J.A., 2012. Real-time targeted molecular imaging using singular value spectra properties to isolate the adherent microbubble signal. Phys. Med. Biol. 57, 5275.

McDannold, N., Arvanitis, C.D., Vykhodtseva, N., Livingstone, M.S., 2012. Temporary Disruption of the Blood–Brain Barrier by Use of Ultrasound and Microbubbles: Safety and Efficacy Evaluation in Rhesus Macaques. Cancer Res. 72, 3652–3663.

Morgan, K.E., Allen, J.S., Dayton, P.A., Chomas, J.E., Klibaov, A.L., Ferrara, K.W., 2000. Experimental and theoretical evaluation of microbubble behavior: effect of transmitted phase and bubble size. IEEE Trans. Ultrason. Ferroelectr. Freq. Control 47, 1494 –1509.

Mountford, P.A., Sirsi, S.R., Borden, M.A., 2014. Condensation Phase Diagrams for Lipid-Coated Perfluorobutane Microbubbles. Langmuir 30, 6209–6218.

Neppiras, E.A., 1980. Acoustic cavitation. Phys. Rep. 61, 159–251.

Orsi, M., Essex, J.W., 2011. The ELBA Force Field for Coarse-Grain Modeling of Lipid Membranes. PLoS ONE 6, e28637.

Overvelde, M., Garbin, V., Sijl, J., Dollet, B., de Jong, N., Lohse, D., Versluis, M., 2010. Nonlinear Shell Behavior of Phospholipid-Coated Microbubbles. Ultrasound Med. Biol. 36, 2080–2092.

Park, J.I., Jagadeesan, D., Williams, R., Oakden, W., Chung, S., Stanisz, G.J., Kumacheva, E., 2010. Microbubbles Loaded with Nanoparticles: A Route to Multiple Imaging Modalities. ACS Nano 4, 6579–6586.

Phillips, L.C., Puett, C., Sheeran, P.S., Dayton, P.A., Miller, G.W., Matsunaga, T.O., 2013. Phase-shift perfluorocarbon agents enhance high intensity focused ultrasound thermal delivery with reduced near-field heating. J. Acoust. Soc. Am. 134, 1473–1482.

Plesset, M.S., 1949. The Dynamics of Cavitation Bubbles. J. Appl. Mech. 16, 277–282.

Plesset, M.S., Prosperetti, A., 1977. Bubble Dynamics and Cavitation. Annu. Rev. Fluid Mech. 9, 145–185.

Porter, T.R., Oberdorfer, J., Rafter, P., Lof, J., Xie, F., 2003. Microbubble responses to a similar mechanical index with different real-time perfusion imaging techniques. Ultrasound Med. Biol. 29, 1187–1192.

Prosperetti, A., 1977. Thermal effects and damping mechanisms in the forced radial oscillations of gas bubbles in liquids. J. Acoust. Soc. Am. 61, 17–27.

Pustovalov, V.K., 2005. Theoretical study of heating of spherical nanoparticle in media by short laser pulses. Chem. Phys. 308, 103–108.

Qin, S., Caskey, C.F., Ferrara, K.W., 2009. Ultrasound contrast microbubbles in imaging and therapy: physical principles and engineering. Phys. Med. Biol. 54, R27.

Rapoport, N., 2012. Phase-shift, stimuli-responsive perfluorocarbon nanodroplets for drug delivery to cancer. Wiley Interdiscip. Rev. Nanomed. Nanobiotechnol. 4, 492–510.

Rayleigh, Lord, 1917. VIII. On the pressure developed in a liquid during the collapse of a spherical cavity. Philos. Mag. Ser. 6 34, 94–98.

Renaud, G., Bosch, J.G., Steen, A.F.W. van der, Jong, N. de, 2012a. Chirp resonance spectroscopy of single lipid-coated microbubbles using an "acoustical camera." J. Acoust. Soc. Am. 132, EL470–EL475.

Renaud, G., Bosch, J.G., van der Steen, A.F.W., de Jong, N., 2012b. An "acoustical camera" for in vitro characterization of contrast agent microbubble vibrations. Appl. Phys. Lett. 100, 101911–101911–4.

Richardson, H.H., Carlson, M.T., Tandler, P.J., Hernandez, P., Govorov, A.O., 2009. Experimental and Theoretical Studies of Light-to-Heat Conversion and Collective Heating Effects in Metal Nanoparticle Solutions. Nano Lett. 9, 1139–1146.

Sarkar, K., Katiyar, A., Jain, P., 2009. Growth and Dissolution of an Encapsulated Contrast Microbubble: Effects of Encapsulation Permeability. Ultrasound Med. Biol. 35, 1385–1396.

Sarkar, K., Katiyar, A., Jain, P., 2009. Growth and dissolution of an encapsulated contrast microbubble: Effects of encapsulation permeability. Ultrasound Med Biol 35, 1385–1396.

Sassaroli, E., Li, K.C.P., O'Neill, B.E., 2009. Linear behavior of a preformed microbubble containing light absorbing nanoparticles: Insight from a mathematical model. J. Acoust. Soc. Am. 126, 2802.

Schleichert, U., Langenberg, K.J., Arnold, W., Fabbender, S., 1989. A Quantitative Theory of Laser-Generated Ultrasound. In: Thompson, D.O., Chimenti, D.E. (Eds.), Review of Progress in Quantitative Nondestructive Evaluation. Springer US, pp. 489–496.

Seo, M., Gorelikov, I., Williams, R., Matsuura, N., 2010. Microfluidic Assembly of Monodisperse, Nanoparticle-Incorporated Perfluorocarbon Microbubbles for Medical Imaging and Therapy. Langmuir 26, 13855–13860.

Shankar, P.M., Krishna, P.D., Newhouse, V.L., 1999. Subharmonic backscattering from ultrasound contrast agents. J. Acoust. Soc. Am. 106, 2104.

Sheeran, P.S., Dayton, P.A., 2014. Improving the Performance of Phase-Change Perfluorocarbon Droplets for Medical Ultrasonography: Current Progress, Challenges, and Prospects. Scientifica 2014, e579684.

Sheeran, P.S., Luois, S., Dayton, P.A., Matsunaga, T.O., 2011a. Formulation and Acoustic Studies of a New Phase-Shift Agent for Diagnostic and Therapeutic Ultrasound. Langmuir 27, 10412–10420.

Sheeran, P.S., Luois, S.H., Mullin, L.B., Matsunaga, T.O., Dayton, P.A., 2012. Design of ultrasonically-activatable nanoparticles using low boiling point perfluorocarbons. Biomaterials 33, 3262–3269.

Sheeran, P.S., Wong, V.P., Luois, S., McFarland, R.J., Ross, W.D., Feingold, S., Matsunaga, T.O., Dayton, P.A., 2011. Decafluorobutane as a phase-change contrast agent for low-energy extravascular ultrasonic imaging. Ultrasound Med. Biol. 37, 1518–1530.

Sheeran, P.S., Wong, V.P., Luois, S., McFarland, R.J., Ross, W.D., Feingold, S., Matsunaga, T.O., Dayton, P.A., 2011b. Decafluorobutane as a Phase-Change Contrast Agent for Low-Energy Extravascular Ultrasonic Imaging. Ultrasound Med. Biol. 37, 1518–1530.

Shekhar, H., Rychak, J.J., Doyley, M.M., 2013. Modifying the size distribution of microbubble contrast agents for high-frequency subharmonic imaging. Med. Phys. 40, 082903.

Shepherd, J.E., Sturtevant, B., 1982. Rapid evaporation at the superheat limit. J. Fluid Mech. 121, 379–402.

Shpak, O., Verweij, M., Vos, H.J., Jong, N. de, Lohse, D., Versluis, M., 2014. Acoustic droplet vaporization is initiated by superharmonic focusing. Proc. Natl. Acad. Sci. 111, 1697–1702.

Sijl, J., Dollet, B., Overvelde, M., Garbin, V., Rozendal, T., Jong, N. de, Lohse, D., Versluis, M., 2010. Subharmonic behavior of phospholipid-coated ultrasound contrast agent microbubbles. J. Acoust. Soc. Am. 128, 3239–3252.

Sijl, J., Vos, H.J., Rozendal, T., Jong, N. de, Lohse, D., Versluis, M., 2011. Combined optical and acoustical detection of single microbubble dynamics. J. Acoust. Soc. Am. 130, 3271–3281.

Simpson, D.H., Chin, C.T., Burns, P.N., 1999. Pulse inversion Doppler: a new method for detecting nonlinear echoes from microbubble contrast agents. IEEE Trans. Ultrason. Ferroelectr. Freq. Control 46, 372–382.

Sirsi, S., Feshitan, J., Kwan, J., Homma, S., Borden, M., 2010. Effect of microbubble size on fundamental mode high frequency ultrasound imaging in mice. Ultrasound Med. Biol. 36, 935–948.

Sirsi, S.R., 2012. Advances in Ultrasound Mediated Gene Therapy Using Microbubble Contrast Agents. Theranostics 2, 1208–1222.

Sirsi, S.R., Hernandez, S.L., Zielinski, L., Blomback, H., Koubaa, A., Synder, M., Homma, S., Kandel, J.J., Yamashiro, D.J., Borden, M.A., 2012. Polyplex-microbubble hybrids for ultrasound-guided plasmid DNA delivery to solid tumors. J. Controlled Release 157, 224–234.

Sorace, A.G., Saini, R., Rosenthal, E., Warram, J.M., Zinn, K.R., Hoyt, K., 2013. Optical fluorescent imaging to monitor temporal effects of microbubble-mediated ultrasound therapy. IEEE Trans. Ultrason. Ferroelectr. Freq. Control 60, 281–289.

Streeter, J.E., Gessner, R., Miles, I., Dayton, P.A., 2010. Improving Sensitivity in Ultrasound Molecular Imaging by Tailoring Contrast Agent Size Distribution: In Vivo Studies. Mol. Imaging 9, 87–95.

Stride, E., Edirisinghe, M., 2008. Novel microbubble preparation technologies. Soft Matter 4, 2350–2359.

Stride, E., Pancholi, K., Edirisinghe, M.., Samarasinghe, S., 2008. Increasing the nonlinear character of microbubble oscillations at low acoustic pressures. J. R. Soc. Interface 5, 807 –811.

Stride, E., Saffari, N., 2003. Microbubble ultrasound contrast agents: A review. Proc. Inst. Mech. Eng. [H] 217, 429–447.

Strohm, E., Rui, M., Gorelikov, I., Matsuura, N., Kolios, M., 2011. Vaporization of perfluorocarbon droplets using optical irradiation. Biomed. Opt. Express 2, 1432–1442.

Tam, A.C., 1986. Applications of photoacoustic sensing techniques. Rev. Mod. Phys. 58, 381.

Thomas, D.H., Butler, M., Anderson, T., Emmer, M., Vos, H., Borden, M., Stride, E., de Jong, N., Sboros, V., 2012. The "quasi-stable" lipid shelled microbubble in response to consecutive ultrasound pulses. Appl. Phys. Lett. 101, 071601–071601–4.

Thomas, D.H., Butler, M., Pelekasis, N., Anderson, T., Stride, E., Sboros, V., 2013. The acoustic signature of decaying resonant phospholipid microbubbles. Phys. Med. Biol. 58, 589.

Thomas, D.H., Looney, P., Steel, R., Pelekasis, N., McDicken, W.N., Anderson, T., Sboros, V., 2009. Acoustic detection of microbubble resonance. Appl. Phys. Lett. 94, 243902.

Tong, L., Wei, Q., Wei, A., Cheng, J., 2009. Gold Nanorods as Contrast Agents for Biological Imaging: Optical Properties, Surface Conjugation and Photothermal Effects†. Photochem. Photobiol. 85, 21–32.

TRC thermodynamic tables. Non-hydrocarbons, 1985. . College Station, Tex : Thermodynamics Research Center.

Tristram-Nagle, S., Zhang, R., Suter, R. M., Worthington, C. R., Sun, W. J., and Nagle, J. F., 1993. Measurement of chain tilt angle in fully hydrated bilayers of gel phase lecithins. Biophysical Journal, 64, 1097–1109.

Tung, Y.-S., Marquet, F., Teichert, T., Ferrera, V., Konofagou, E.E., 2011a. Feasibility of noninvasive cavitation-guided blood-brain barrier opening using focused ultrasound and microbubbles in nonhuman primates. Appl. Phys. Lett. 98, 163704–163704–3.

Tung, Y.-S., Vlachos, F., Feshitan, J.A., Borden, M.A., Konofagou, E.E., 2011b. The mechanism of interaction between focused ultrasound and microbubbles in blood-brain barrier opening in mice. J. Acoust. Soc. Am. 130, 3059–3067.

Unger, E.C., Hersh, E., Vannan, M., Matsunaga, T.O., McCreery, T., 2001. Local drug and gene delivery through microbubbles. Prog. Cardiovasc. Dis. 44, 45–54.

Unger, E.C., Porter, T., Culp, W., Labell, R., Matsunaga, T., Zutshi, R., 2004. Therapeutic applications of lipid-coated microbubbles. Adv. Drug Deliv. Rev. 56, 1291–1314.

Van der Meer, S.M., Dollet, B., Voormolen, M.M., Chin, C.T., Bouakaz, A., de Jong, N., Versluis, M., Lohse, D., 2007. Microbubble spectroscopy of ultrasound contrast agents. J. Acoust. Soc. Am. 121, 648.

Van Osdol, W.W., Johnson, M.L., Ye, Q., and Biltonen, R.L., 1991, Relaxation dynamics of the gel to liquid-crystalline transition of phosphatidylcholine bilayers. Effects of chainlength and vesicle size. Biophys. J. 59, 775-785.

Versluis, M., Goertz, D.E., Palanchon, P., Heitman, I.L., van der Meer, S.M., Dollet, B., de Jong, N., Lohse, D., 2010. Microbubble shape oscillations excited through ultrasonic parametric driving. Phys. Rev. E 82, 026321.

Vos, H.J., Dollet, B., Versluis, M., de Jong, N., 2011. Nonspherical Shape Oscillations of Coated Microbubbles in Contact With a Wall. Ultrasound Med. Biol. 37, 935–948.

Wang, L.V., 2009. Multiscale photoacoustic microscopy and computed tomography. Nat Photon 3, 503–509.

Wang, L.V., Gao, L., 2014. Photoacoustic Microscopy and Computed Tomography: From Bench to Bedside. Annu. Rev. Biomed. Eng. 16, 155–185.

Wang, L.V., Hu, S., 2012. Photoacoustic Tomography: In Vivo Imaging from Organelles to Organs. Science 335, 1458 –1462.

Wang, P.-H., Liu, H.-L., Hsu, P.-H., Lin, C.-Y., Chris Wang, C.-R., Chen, P.-Y., Wei, K.-C., Yen, T.-C., Li, M.-L., 2012. Gold-nanorod contrast-enhanced photoacoustic micro-imaging of focused-ultrasound induced blood-brain-barrier opening in a rat model. J. Biomed. Opt. 17, 061222.

Wang, Y.-H., Li, P.-C., Liao, A.-H., Chen, J.-H., Wang, C.-R.C., 2012. Photoacoustic/ultrasound dual-modality contrast agent and its application to thermotherapy. J Biomed Opt 17.

Wang, Y., Xie, X., Wang, X., Ku, G., Gill, K.L., O'Neal, D.P., Stoica, G., Wang, L.V., 2004. Photoacoustic Tomography of a Nanoshell Contrast Agent in the in Vivo Rat Brain. Nano Lett 4, 1689–1692.

Wei, C., Lombardo, M., Larson-Smith, K., Pelivanov, I., Perez, C., Xia, J., Matula, T., Pozzo, D., O'Donnell, M., 2014a. Nonlinear contrast enhancement in photoacoustic molecular imaging with gold nanosphere encapsulated nanoemulsions. Appl. Phys. Lett. 104, 033701.

Wei, C., Xia, J., Lombardo, M., Perez, C., Arnal, B., Larson-Smith, K., Pelivanov, I., Matula, T., Pozzo, L., O'Donnell, M., 2014b. Laser-induced cavitation in nanoemulsion with gold nanospheres for blood clot disruption: in vitro results. Opt. Lett. 39, 2599–2602.

Wei, K., Jayaweera, A.R., Firoozan, S., Linka, A., Skyba, D.M., Kaul, S., 1998. Quantification of Myocardial Blood Flow With Ultrasound-Induced Destruction of Microbubbles Administered as a Constant Venous Infusion. Circulation 97, 473–483.

Wilson, K., Homan, K., Emelianov, S., 2012. Biomedical photoacoustics beyond thermal expansion using triggered nanodroplet vaporization for contrast-enhanced imaging. Nat Commun 3, 618.

Wilson, S.R., Burns, P.N., 2010. Microbubble-enhanced US in Body Imaging: What Role? Radiology 257, 24–39.

Wilson, S.R., Jang, H.-J., Kim, T.K., Iijima, H., Kamiyama, N., Burns, P.N., 2008. Real-Time Temporal Maximum-Intensity-Projection Imaging of Hepatic Lesions with Contrast-Enhanced Sonography. Am. J. Roentgenol. 190, 691–695.

Xu, M., Wang, L.V., 2006. Photoacoustic imaging in biomedicine. Rev. Sci. Instrum. 77, 041101.

Yang, F., n.d. Superparamagnetic iron oxide nanoparticle-embedded encapsulated microbubbles as dual contrast agents of magnetic resonance and ultrasound imaging. BIOMATERIALS.

Yang, F., Wang, Q., Gu, Z., Fang, K., Marriott, G., Gu, N., 2013. Silver Nanoparticle-Embedded Microbubble as a Dual-Mode Ultrasound and Optical Imaging Probe. ACS Appl. Mater. Interfaces 5, 9217–9223.

Yang, X., Skrabalak, S.E., Li, Z.-Y., Xia, Y., Wang, L.V., 2007. Photoacoustic Tomography of a Rat Cerebral Cortex in vivo with Au Nanocages as an Optical Contrast Agent. Nano Lett. 7, 3798–3802.

Yang, X., Stein, E., Ashkenazi, S., Wang, L., 2009. Nanoparticles for photoacoustic imaging. Wiley Interdiscip Rev Nanomed Nanobiotechnol 1, 360–368.

Yelin, D., Oron, D., Thiberge, S., Moses, E., Silberberg, Y., 2003. Multiphoton plasmon-resonance microscopy. Opt. Express 11, 1385–1391.

Yuan, B., Uchiyama, S., Liu, Y., Nguyen, K.T., Alexandrakis, G., 2012. High-resolution imaging in a deep turbid medium based on an ultrasound-switchable fluorescence technique. Appl. Phys. Lett. 101, 033703.

Zhang, P., Porter, T., 2010. An in vitro Study of a Phase-Shift Nanoemulsion: A Potential Nucleation Agent for Bubble-Enhanced HIFU Tumor Ablation. Ultrasound Med. Biol. 36, 1856–1866.

Zhang, Q., Iwakuma, N., Sharma, P., Moudgil, B.M., Wu, C., McNeill, J., Jiang, H., Grobmyer, S.R., 2009. Gold nanoparticles as a contrast agent for in vivo tumor imaging with photoacoustic tomography. Nanotechnology 20, 395102.